12-2013

A Compact Ultra Wide-Band Radar System for See-Through-Wall Applications

Stephen G. Magoon
University of Tennessee - Knoxville, smagoon@utk.edu

To the Graduate Council:

I am submitting herewith a thesis written by Stephen G. Magoon entitled "A Compact Ultra Wide-Band Radar System for See-Through-Wall Applications." I have examined the final electronic copy of this thesis for form and content and recommend that it be accepted in partial fulfillment of the requirements for the degree of Master of Science, with a major in Electrical Engineering.

Aly E. Fathy, Major Professor

We have read this thesis and recommend its acceptance:

Benjamin J. Blalock, Jayne Wu

Accepted for the Council:
Carolyn R. Hodges

Vice Provost and Dean of the Graduate School

(Original signatures are on file with official student records.)

12-2013

A Compact Ultra Wide-Band Radar System for See-Through-Wall Applications

Stephen G. Magoon
smagoon@utk.edu

To the Graduate Council:

I am submitting herewith a thesis written by Stephen G. Magoon entitled "A Compact Ultra Wide-Band Radar System for See-Through-Wall Applications." I have examined the final electronic copy of this thesis for form and content and recommend that it be accepted in partial fulfillment of the requirements for the degree of , with a major in Electrical Engineering.

Aly Fathy, Major Professor

We have read this thesis and recommend its acceptance:

Benjamin J Blalock, Jayne Wu

Accepted for the Council:
Carolyn R. Hodges

Vice Provost and Dean of the Graduate School

(Original signatures are on file with official student records.)

A Compact Ultra Wide-Band Radar System for See-Through-Wall Applications

A Thesis Presented for the

Master of Science

Degree

The University of Tennessee, Knoxville

Stephen G. Magoon

December 2013

Acknowledgements

I am grateful for the instruction and supervision of "Hall of Fame" professors Dr. Aly Fathy, Dr. Ben Blalock, and Dr. Jayne Wu.

I am especially thankful for my wife, Colette. She is an inspiration not only to me, but to our many family, personal, and college student friends.

To God be the glory, great things He has done! So loved He the world that He gave us His Son!

Abstract

A compact Ultra wide-band (UWB) radar system for through-wall applications has been developed. Lightweight, portable and low in power consumption, it is configurable for both bistatic and monostatic operation. It uses low cost, off-the-shelf surface mount components, and is ideally suited for ranging, 3d-imaging, and wall characterization. Tests show excellent pulse width generation, resulting in very broadband transmission (0.7 – 5.6 GHz) and good receiver dynamic range, resulting in accurate measurement capabilities.

Table of Contents

List of Tables

List of Figures

Chapter 1 – Introduction

This thesis documents the development of a system using Ultra wideband (UWB) radar for the localization of objects through walls and for wall characterization. UWB, a term originally coined by the military in the 1990's and later defined by the FCC, describes the use of wide bandwidth, very low energy pulse transmission.

Some of the history for this technology dates back to the 1960's, when Dr. Gerald Ross and others [1] sought to characterize microwave antenna components by their impulse response. From signal theory the convolution integral is

$$y(t) = x(t) * h(t) = \int_{-\infty}^{+\infty} x(u)h(t-u)du \qquad (1)$$

Injecting the input of a network with an impulse $x(t)$, the output could be observed and the network's transfer function $h(t)$ could be determined. This type of characterization required the development of pulses that could approach the theoretical Dirac impulse of zero pulse width and infinite amplitude. By transmitting a fast pulse through air, scientists, including Dr. Ross, recognized the opportunity that impulse response afforded for locating and characterizing physical objects.

Fast pulse UWB has numerous advantages over conventional radar, including higher accuracy due to its shorter wavelengths, immunity to passive interference such as rain, fog, and clutter, increased security because of its broad spectrum spreading, and its ability to detect slowly moving or static targets [1]. Early applications of UWB were for low probability of detection radar and communications. As interest grew, the FCC released the 3.1 – 10.6 GHz band for use at low power: -41.3 dBm/MHz equivalent isotropically radiated power (EIRP). Following this decision, applications developed for nondestructive evaluation of civil engineering structures, mineral locating, biological diagnosis, terrain profiling and remote sensing.

Figure 1 – UWB radar applications

In particular, interest has grown in object localization and motion detection. Existing imaging devices can track persons of concern behind walls or other objects, or locate people trapped due to fire or earthquake. UWB used in ground penetrating radar can locate buried mines. Pulsed-Doppler UWB radar can be used to detect whether weapons are being carried by moving persons, or to monitor vital signs of patients in hospitals or the activity of elderly people at home [2].

Other technology has been proposed for through-wall imaging, such as narrowband radar, ultrasound, infrared and x-ray. Table 1 compares these technologies and demonstrates a strong future for UWB radar [3].

Table 1 – Comparing current imaging technology

	Narrowband Radar	**Ultrasound**	**Infrared**	**X-ray**	**UWB Radar**
Resolution	Poor	Good	Good	Good	Good
Day/Night Operation	Yes	Yes	No	No	Yes
Wall Penetration	Good	Marginal	Good	Good	Good
Motion Tracking	Yes	Yes	No	No	Yes

Constructing an UWB radar system has its challenges:

- For good range resolution, fast pulses are required with large bandwidths relative to the carrier. Component availability narrows as a result. In addition, a wide bandwidth signal means large amounts of data must be recorded and stored. If the object of interest is moving, the data must be digitized quickly and stored at high refresh rates to be meaningful.
- The system must have a high dynamic range in order to distinguish from the strong reflections from building walls and the low intensity signals from objects behind walls.
- Wideband antennas, antenna arrays, and power dividers are required that are not available "off the shelf".
- Software and/or algorithms are needed that can process the data quickly and create real-time images.

Research at the University of Tennessee under Dr. Aly Fathy, Dr. Yazhou Wang and others had produced a prototype of a UWB radar system that was used extensively for through-wall localization,

human gait analysis and respiration detection. It overcame many of the challenges through the development of a high dynamic range RF front end and a fast data acquisition system. Also, a USB 2.0 serial link was created to quickly upload the data to a PC, and a wideband Vivaldi array was fabricated to cover the 1.0 to 6.0 GHz bandwidth of interest. Software was written to process the raw data for real-time image display.

Interest in the prototype provided motivation for a possible field-usable device, for example, in a military application. Therefore, a simple, easy to use mobile device with low power requirements was begun.

The basis of this thesis, then, is the design, fabrication and testing of a complete, compact, and mobile UWB radar system based on the original See-Through-Wall prototype.

The thesis is divided into four sections. The introduction provides some electromagnetics background for understanding the use of travelling, pulsed waves directed toward targets of interest. A simple conclusion is reached that has important ramifications for an adaptation to the original bistatic radar system. Chapter 2 covers the design details and Chapter 3, testing of the new module. Chapter 4 introduces an adapter to convert the original prototype to a monostatic radar system. The final two chapters discuss future work for the project and conclusions.

Electromagnetics and Radar

Travelling waves

Electromagnetic theory states that a time-varying electric field produces a time-varying magnetic field, and conversely, a time-varying magnetic field produces a time-varying electric field. Therefore, establishing a time-varying current in conducting media will often generate a travelling, time-varying electric and magnetic field. Though spherical in nature, observing this field at a distance away from the

source looks like a uniform *plane* wave, i.e., a wave with properties that are the same at all points on its travelling surface.

Maxwell's equations give expressions for this travelling wave.

$$\nabla \times E = -jw\mu H \tag{2}$$

$$E(x,y,z) = a_x E_x(x,y,z) + a_y E_y(x,y,z) + a_z E_z(x,y,z) \tag{3}$$

Equation (2) describes the coupling between the E and H fields in the frequency domain, where *w* is the frequency of the wave in radians per second, and μ is the permeability of the medium the wave travels in. Assuming a source-free medium, the uncoupled version of this equation is [4]

$$\nabla^2 E = jw\mu\sigma E - w^2\mu\varepsilon E \tag{4}$$

Or

$$\nabla^2 E = \gamma^2 E \tag{5}$$

For equation (5)

$$\gamma^2 = jw\mu\sigma - w^2\mu\varepsilon \tag{6}$$

With

$$\gamma = \alpha + j\beta \tag{7}$$

In equation (7), α is the attenuation constant in nepers/m, β the phase constant in radians/m, σ represents the conductivity in lossy media in Siemens/m, and ε is the complex permittivity of the medium in farads/m. The phase constant β is also represented by the letter *k*, called the wave number. In free space $\varepsilon = \varepsilon_0$, $\alpha \cong 0$ and $\beta = w\sqrt{\mu\varepsilon}$. Therefore equation (4) can be written as

$$\nabla^2 E + \beta^2 E = 0 \tag{8}$$

For a plane wave in the *x*-*y* plane of the Cartesian coordinate system and assuming only vertical polarization, *E* does not vary with *x* and *y*, and equation (8) can be written as

$$\frac{d^2 E_x}{dz^2} + \beta^2 E_x = 0 \tag{9}$$

Equation (9) is an ordinary differential equation with general solution [5]

$$E_x(z) = E_x^+(z) + E_x^-(z) = E_{x0}^+ e^{-jkz} + E_{x0}^- e^{+jkz} \tag{10}$$

This solution represents two travelling waves, one in the $+z$ direction and one in the $-z$ direction. For a wave travelling in the $+z$ direction,

$$E_x(z) = E_{x0}^+ e^{-jkz} \tag{11}$$

Using a similar procedure, with $\eta = \sqrt{\frac{\mu}{\varepsilon}}$, the intrinsic impedance of the medium,

$$H_y(z) = H_{y0}^+ e^{-jkz} = \frac{E_{x0}^+}{\eta} e^{-jkz} \tag{12}$$

The corresponding instantaneous form for the *E* field is

$$E(z;t) = Re\left[E_{x0}^+ e^{-jkz}\right] = E_{x0}^+ \cos(wt - \beta z) \tag{13}$$

This wave has velocity

$$v = \frac{dz}{dt} = \frac{w}{\beta} = \frac{1}{\sqrt{\mu\varepsilon}} \tag{14}$$

For free space, the wave velocity is the speed of light, *c*. For medium other than free space, velocity, wave number and attenuation should be taken into account.

Boundaries

As previously mentioned, this system was developed for, among other things, through-wall localization and wall characterization. Therefore the propagation of electromagnetic waves in and through boundaries must also be characterized.

When a travelling wave encounters a boundary such as a wall or the ground, assuming no sources such as current flow or surface charge at this boundary, Maxwell's equations demonstrate that the tangential components of the electric and magnetic fields crossing the boundary are continuous.

$$n \times (E_{1t} - E_{2t}) = 0 \tag{15}$$

$$n \times (H_{1t} - H_{2t}) = 0 \tag{16}$$

In these equations, *n* represents a unit vector normal to the surface of the boundary. For simplicity, assume the plane wave travelling through free space, with electric field transverse to the wave, encounters the boundary normal to its surface, as shown in Figure 2.

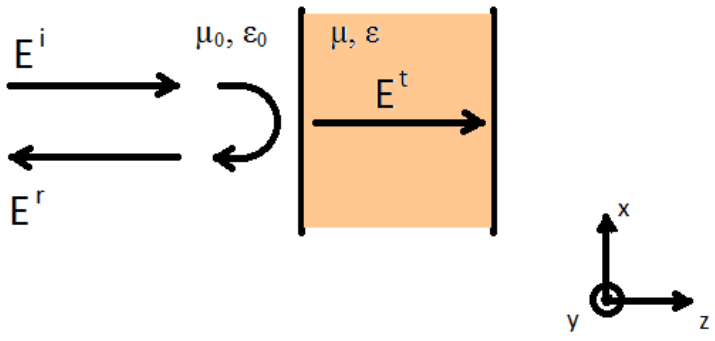

Figure 2 – Incident wave upon a wall boundary

The electric field incident to the boundary can be written as

$$E^i = a_x E_{x0}^+ e^{-jkz} \tag{17}$$

Using the reflection coefficient Γ^b and the transmission coefficient T^b, the reflected and transmitted fields normal to the boundary are

$$E^r = a_x E_{x0}^+ \Gamma^b e^{+jk_1 z};\ E^t = a_x E_{x0}^+ T^b e^{-jk_2 z} \tag{18}$$

The magnetic fields are similar,

$$H^i = a_y \frac{E_{x0}^+}{\eta_1} e^{-jk_1 z} \tag{19}$$

$$H^r = -a_y \frac{E_{x0}^+}{\eta_1} \Gamma^b e^{+jk_1 z};\ H^t = a_y \frac{E_{x0}^+}{\eta_2} T^b e^{-jk_2 z} \tag{20}$$

Enforcing the tangential boundary conditions,

$$E^i + E^r = E^t \tag{21}$$

$$H^i + H^r = H^t \tag{22}$$

Solving for Γ^b and T^bgives

$$\Gamma^b = \frac{\eta_1 - \eta_2}{\eta_1 + \eta_2} \tag{23}$$

$$T^b = \frac{2\eta_2}{\eta_1 + \eta_2} \tag{24}$$

Note that as the *load* impedance of the boundary approaches the *source* impedance of the medium through which the wave travels, the reflection coefficient approaches zero and the transmission coefficient approaches one. Therefore, waves travelling through materials such as gypsum (sheet rock),

concrete, brick or dry soil would be attenuated much less than at a boundary with a high dielectric constant, such as sea water, or high conductivity, such as metal.

For lossy medium, the attenuation constant can no longer be neglected, and η becomes complex. The general solution to equation (5) becomes [4]

$$E(z) = a_x\left(E_0^+ e^{-j\gamma z} + E_0^- e^{+j\gamma z}\right) = a_x E_0^+ e^{-\alpha z} e^{-j\beta z} + a_x E_0^- e^{+\alpha z} e^{+j\beta z} \qquad (25)$$

For a good dielectric,

$$\left(\frac{\sigma}{w\varepsilon}\right)^2 \ll 1 \qquad (26)$$

$$\alpha = \frac{\sigma}{2}\sqrt{\frac{\mu}{\varepsilon}} \qquad (27)$$

The term on the left of equation (26) is also known as the loss tangent (tan δ) squared. As a practical example, five inch thick concrete block has a permittivity of 9.0 and an approximate loss tangent magnitude of 0.1 at 1 GHz [6], so its attenuation constant α would be 24.5 Np/m, and the loss would be -14 dB across the wall in one direction.

Figure 3 diagrams a plane wave that runs into a wall at an oblique angle, and again assumes a linear, vertically polarized wave. Because the wall represents two boundaries of different permittivity, multiple reflections occur with magnitudes that attenuate according to equation (25). Reflection and transmission angles of the resultant waves depend on the physical characteristics of the medium.

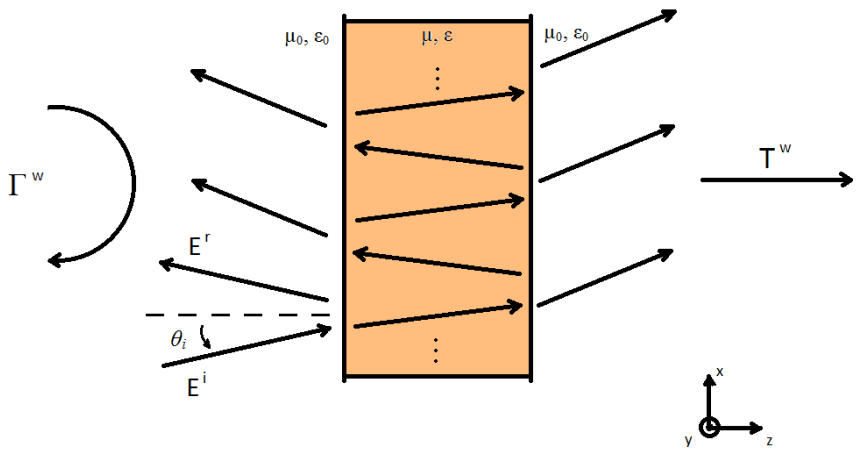

Figure 3 – Multiple reflections of a travelling wave incident upon a wall

The incident, linear, vertically polarized electric field can be written as

$$E_i = (a_x \cos(\theta_i) - a_z \sin(\theta_i)) E_0 e^{-j\beta_0(x sin\theta_i + z cos\theta_i)} \tag{28}$$

The field has components in both the "x" and "z" directions, depending on the angle of incidence θ_i.

From [4]

$$\Gamma^w = \frac{C_0}{D_0};\ T^w = \frac{1}{D_0} \tag{29}$$

$$C_0 = \frac{e^{\psi}}{2}(1+Z_2)(1+Z_1) + \frac{e^{-\psi}}{2}(1-Z_2)(1-Z_1) \tag{30}$$

$$D_0 = \frac{e^{\psi}}{2}(1+Z_2)(1-Z_1) + \frac{e^{-\psi}}{2}(1-Z_2)(1+Z_1) \tag{31}$$

$$Z_1 = \frac{cos\theta_1}{cos\theta_i}\sqrt{\frac{\varepsilon_0}{\varepsilon_1(1-jtan\delta_1)}};\ Z_2 = \frac{cos\theta_2}{cos\theta_1}\sqrt{\frac{\varepsilon_1(1-jtan\delta_1)}{\varepsilon_0}} \tag{32}$$

$$\psi = d\gamma cos\theta_1; \quad sin\theta_1 = \frac{\gamma_i}{\gamma_1} sin\theta_i; \quad sin\theta_2 = \frac{\gamma_1}{\gamma_i} \tag{33}$$

The complex solution to oblique incidence demonstrates added attenuation, polarization, and non-uniform refracted waves from objects of interest. To reduce these unwanted elements, ideally the angle of incidence should be minimized, preferably approaching zero degrees. Thus, normal incidence should produce more reliable imaging and wall characterization data.

Wall Characterization

The radar system documented in this thesis takes advantage of measurements in the *time* domain. It transmits a narrow, broadband pulse at a rate of 10 MHz, and then captures the reflected pulses from targeted objects. These pulses are encoded at an equivalent sampling rate of 100 Gbps and the data is stored on a local computer. One such example can be seen in Figure 4. A dihedral was placed behind a wall formed from 5" solid concrete brick. Reflections from the front and back of the wall as well as from the metal object can be seen from the plotted data.

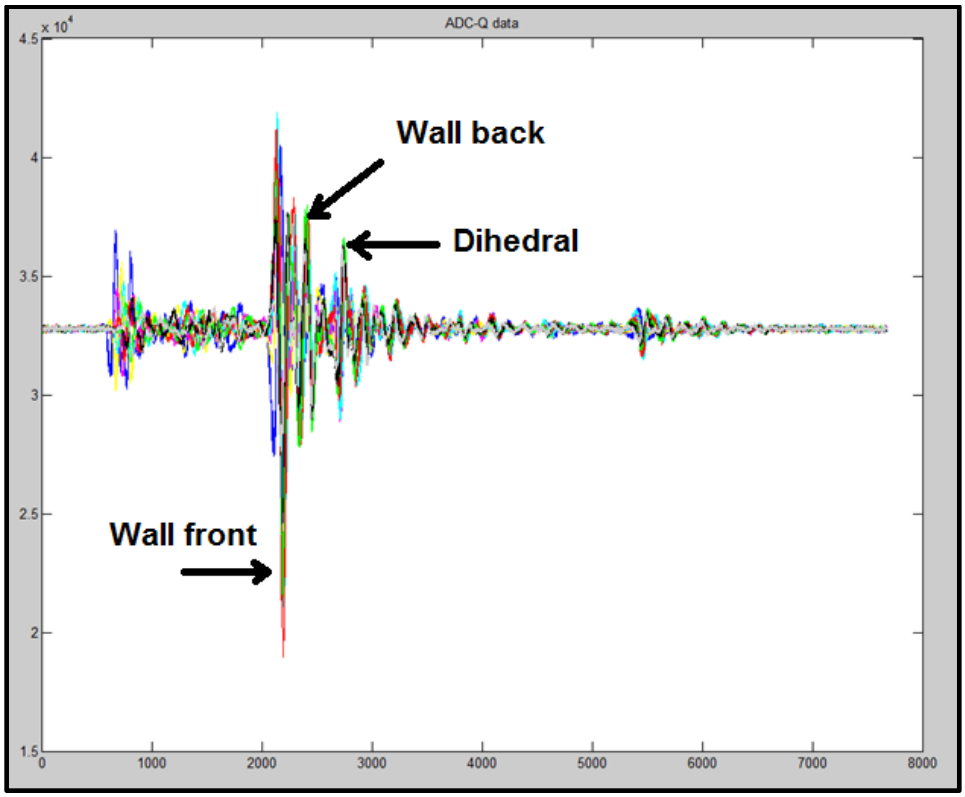

Figure 4 – Pulse data from a wall experiment

Of special concern are the strong reflections that result from external walls, because they may mask the target of interest. In order to effectively image these targets, wall reflections must be removed before any post-processing image enhancement can be attempted. To do this, knowledge of the wall parameters such as thickness and dielectric constant must be determined.

Wall characterization in the *lab* is relatively simple. As shown in Figure 5, a Vector Network Analyzer (VNA) measures S-parameters of the wall under consideration. Then using equations (23) and (24), wall parameters such as permittivity and conductivity can be calculated. However, in the remote case, for example of a building in a city, the transmission coefficient is not available and the environment uncontrolled.

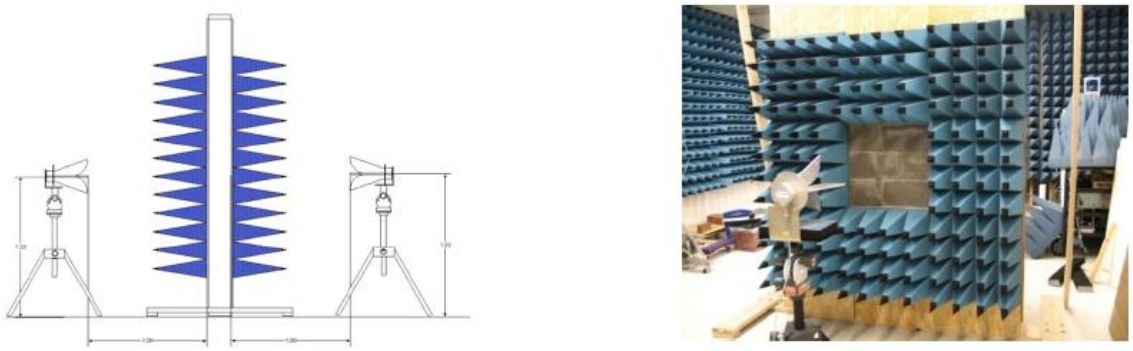

Figure 5 – Wall parameter estimation in the lab

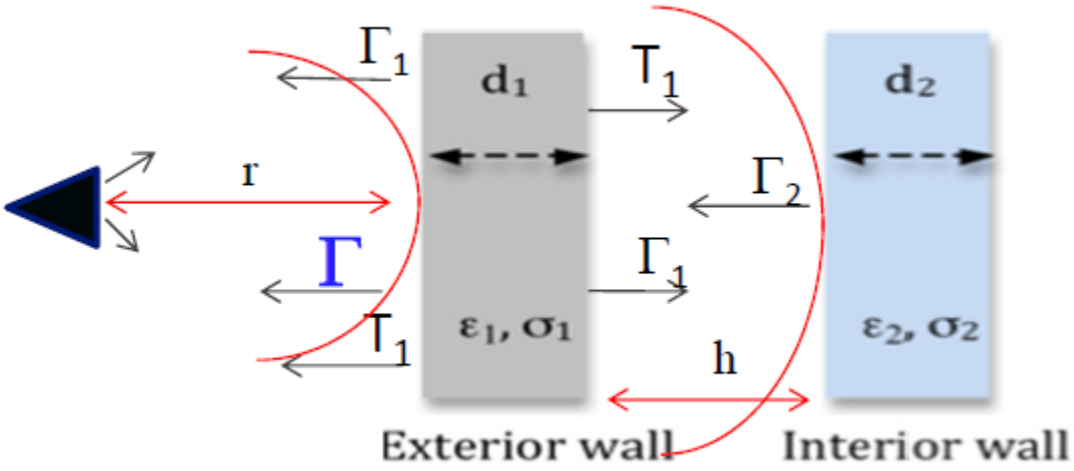

Figure 6 – Estimating multiple wall parameters

Multiple walls and space between walls, such as hallways, must also be considered. Multiple wall parameter techniques are available, such as [7]

1. The Layer-Peeling method. It uses an iterative technique to solve for permittivity and layer thickness. However, it is time consuming, not applicable to lossy walls and does not account for wave scattering.
2. Inverse Scattering. This approach applies to multi-layered wall geometry, but robustness and speed of implementation may be an issue.
3. Time Domain Reflectometry (TDR)

   This approach has practical application primarily to a single wall, but not to multiple walls or gaps, such as hallways between walls. It requires two time domain measurements, the wall response and a calibration response from a metal plate. TDR then estimates the wall parameters.

Thajudeen has completed extensive research in this area and developed the following modified TDR procedure [7]:

1. Perform PEC (perfect electrical conductor, a metal plate) calibration at the external wall and apply the standard TDR method on the first two responses from the first wall to calculate its parameters.
2. Model the exterior wall and then remove its response. The resulting response represents the internal wall.
3. The location of the first response from the interior wall determines wall separation.
4. Account for wall effects in forward (antenna-to-target) and backward (target-to-antenna) transmitted signals using a compensation factor.
5. Repeat the standard TDR method to acquire the inner wall parameters.

From this research, equations were derived for estimating these wall parameters. Assuming a homogeneous wall, normal incidence and wall parameters independent of frequency,

$$\Gamma^w = -\frac{\|h(n)\|_\infty}{\|h_m(n)\|_\infty} \tag{34}$$

The transfer functions *h(n)* and $h_m(n)$ represent the wall response and calibration response, respectively, to a PEC.

Once wall response and calibration data are gathered, wall permittivity, thickness and conductivity can be determined by

$$\varepsilon_r = \frac{(1-\Gamma^w)^2}{(1+\Gamma^w)^2} \tag{35}$$

$$d_w = \frac{v\Delta t}{2}; \quad v = \frac{c}{\sqrt{\varepsilon_r}} \tag{36}$$

$$\sigma = 2\sqrt{\varepsilon_r}\frac{\|h_2(n)\|_\infty}{\|h(n)\|_\infty}\left(1-\Gamma^{w^2}\right) \tag{37}$$

$$h_2(n) \approx h(n) + \Gamma^w h_m(n) \tag{38}$$

These useful equations provide the basis for data analysis in Chapter 4.

Chapter 2 – System Hardware Integration

The UWB radar imaging prototype developed by Dr. Yazzhou Wang [8] and others is shown in Figure 7. It consisted of components with connectors, cables, and several evaluation boards. This chapter documents the development of a new module with improved performance, functionality, and significant size and power reduction over the original prototype. Figure 8 shows the proposed structural outline of the new compact, portable module, with dimensions of 4" W x 8" L x 2.5" D. The FPGA controller board and antennas (not shown) were not included in the module design.

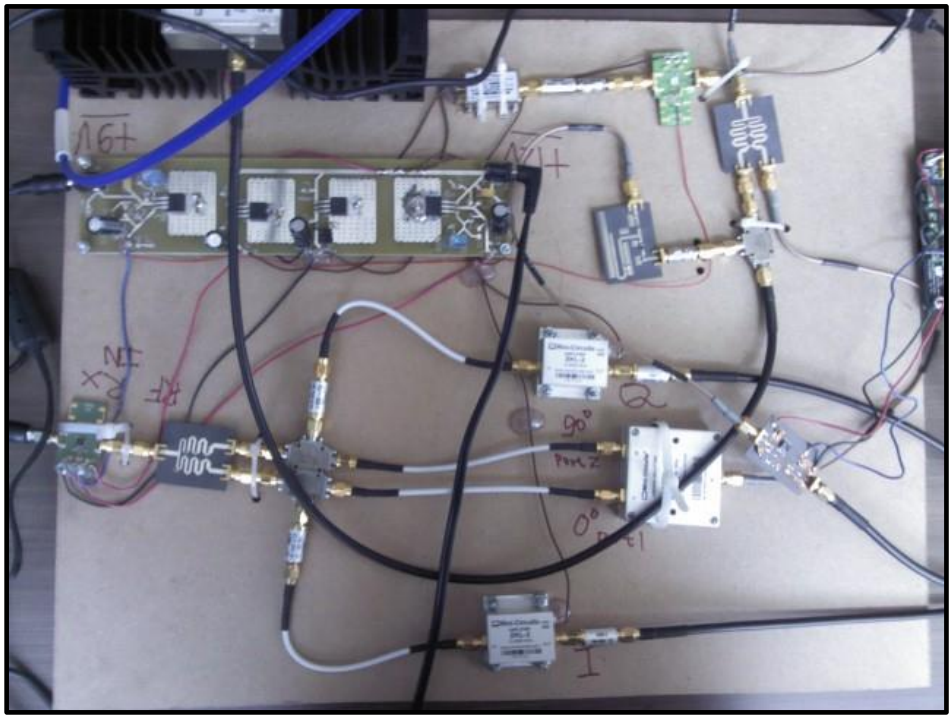

Figure 7 – Original prototype

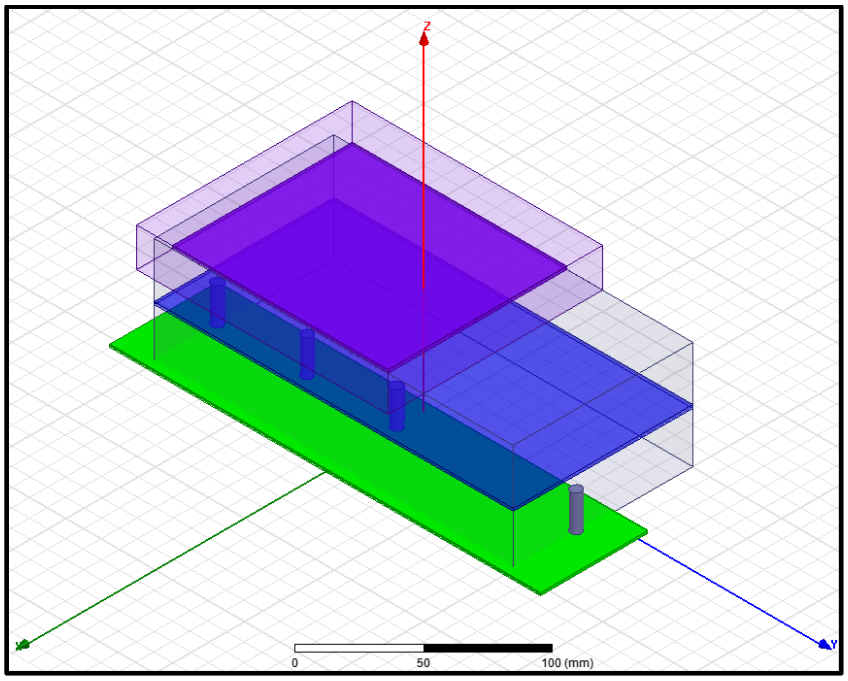

Figure 8 – New module assembly objective

System Overview

Background of the Transceiver RF Front-end

The detailed block diagram of the previously developed UWB Doppler radar is shown in Figure 9. For the transmitter, a 10 MHz clock generated by FPGA circuitry powered a 700ps Gaussian pulse generator. The Gaussian pulse was modulated with a 3 GHz carrier by a Hittite HMC213 mixer. The Hittite HMC753 low noise amplifier (LNA) and the Mini-Circuits ZHL-42 power amplifier (PA) generated sufficient gain for transmission via a wideband Vivaldi antenna. At the receiver, the collected radar returned signal was amplified by another Hittite HMC753 LNA and then down-converted into baseband. The down conversion was implemented by mixing the modulated signal with the same carrier (thus called a *coherent* system) and Hittite HMC213 mixer. Finally, the baseband I and Q signals were low-pass filtered and amplified before being sent to the data sampling and acquisition module.

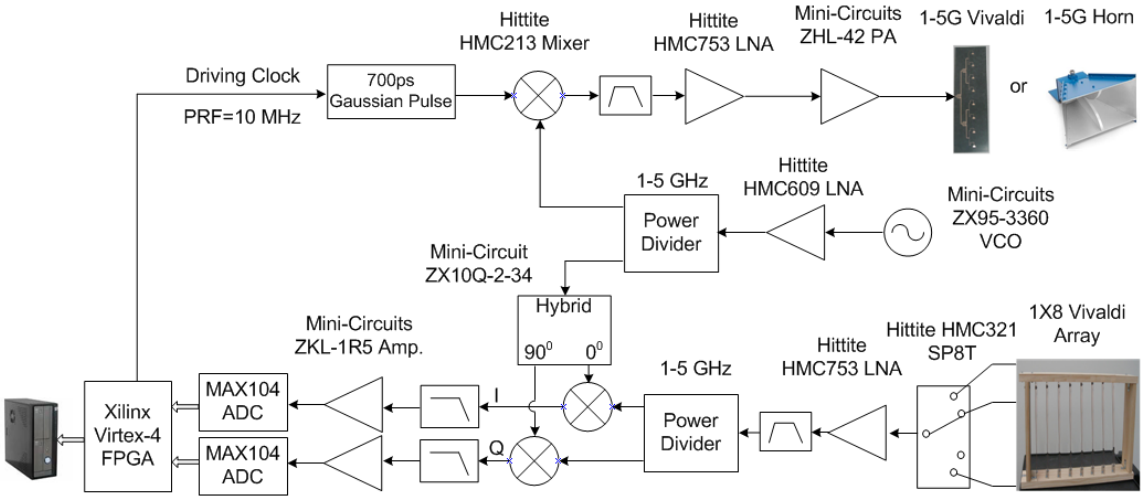

Figure 9 – Prototype block diagram

Figure 10 introduces the link budget analysis of the previously developed radar transceiver. The transmitting power level was mainly decided by the last stage power amplifier. The selected commercial component, the Mini-Circuits ZHL-42PA, provided a 1dB output power compression point of 28dBm. To avoid nonlinearity and signal distribution, a slight margin of 25dBm was used. At the receiver, the commercial LNA HMC753 had a 1dB input compression point of 18 dBm. The HMC213 commercial mixer had a 1dB input gain compression point of 9dBm. Therefore the maximum input power level injected into radar receiver was 0dBm. This set a minimum isolation requirement between the radar transmitter and receiver of 25 dB, easily achieved by separating the transmitting and receiving antennas, or by placing the transmitting antenna slightly forward to reduce the coupling between them, as in the case of bistatic radar. Table 2 gives the analysis of the isolation requirement between radar transmitter and receiver.

The dynamic range of the radar receiver was calculated as shown in Table 3. The thermal noise floor of the receiver is -174 dBm/Hz, or -114 dBm/MHz. The radar receiver has a bandwidth of about 3 GHz and therefore, the noise floor of the radar receiver is -79 dBm. The receiver had a noise figure of approximately 8dB, which was mainly due to the cable loss, SP8T switch loss, and the noise figure of the HMC753 LNA. The minimum signal-to-noise ratio (SNR) required for acceptable imaging quality is 6dB. Subsequently, the acquired radar receiver sensitivity was -65 dBm. Since the receiver 1dB input compression point is 0dBm, the receiver had a dynamic range of as much as 65 dB.

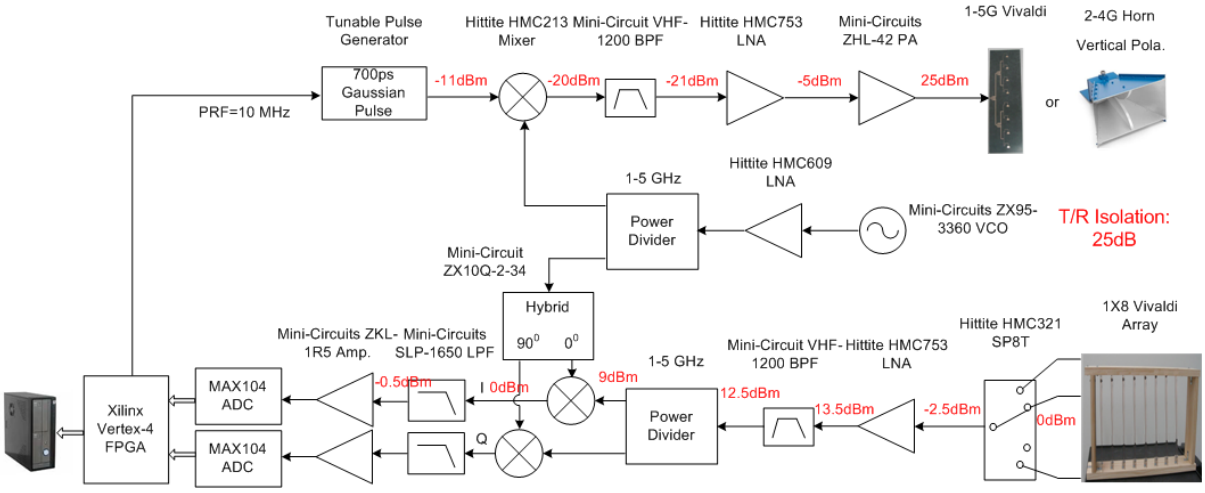

Figure 10 – Link budget analysis of the radar transceiver

Table 2 – Isolation requirement between radar transmitter and receiver

Parameters	**Values**
Transmitter Total Power (dBm)	25
Rx 1dB Compression Point (dBm)	0
Required Tx-Rx Isolation (dB)	25
Tx/Rx Isolation achieved by placing Tx and Rx antennas apart	

Table 3 – Dynamic range analysis of the radar transceiver

Parameters	Values
Rx Thermal Noise Floor (dBm/Hz)	-174
Rx Thermal Noise Floor (dBm/MHz)	-114
Receiver Bandwidth (GHz)	3
Receiver Thermal Noise Floor (dBm)	-79
Receiver Noise Figure (dB)	8
Receiver Noise Floor (dBm)	-71
Required SNR (dB)	6 (for acceptable image quality)
Receiver Sensitivity (dBm)	-65
Rx 1dB Compression Point (dBm)	0
Receiver Dynamic Range (dB)	65

Digital Controller Board and Antennas

Figure 11 shows the controller board for the UWB radar system [9] used extensively in this project. It sported a Xilinx Virtex-5 FPGA, and a National Semiconductor ADC16DV160 ADC dual-channel, 16-bit Analog to Digital Converter, as well as a Cypress USB microcontroller and 10 ps digital delay chip. The board provided several functions:

- Dual-channel 100 Gbps equivalent sampling at its "I" and "Q" input ports.
- Internal algorithms within the FPGA for data buffering, matched filtering, localization calculations for 2D-3D imaging, clock generation, and switching for the Vivaldi antenna array
- USB data serialization
- Optional external clock control

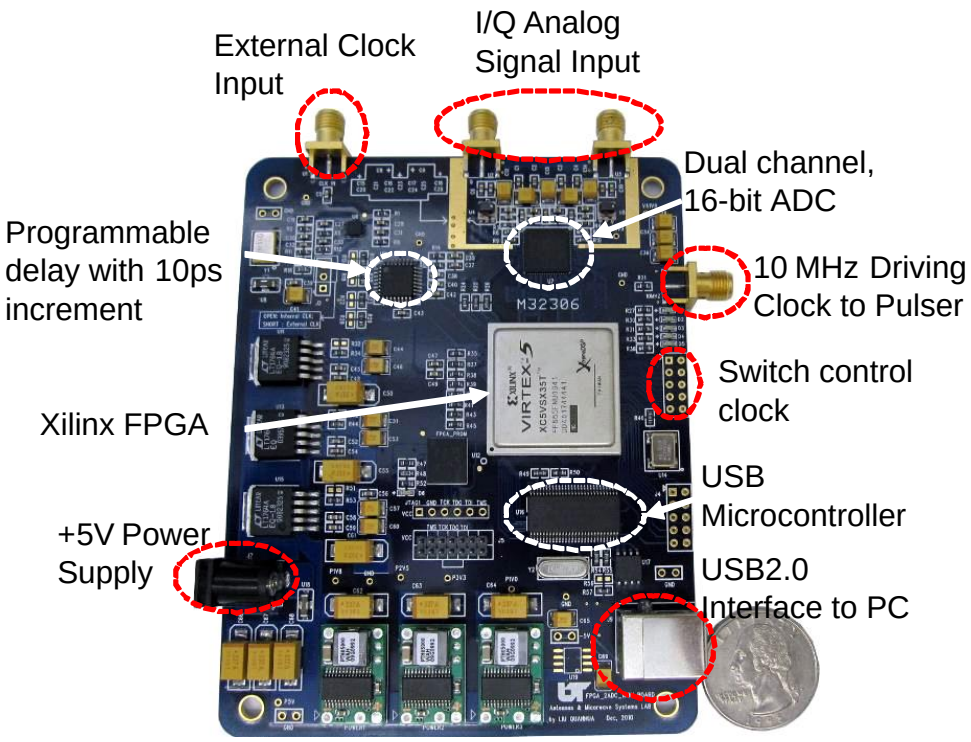

Figure 11 – Digital controller used for the new module

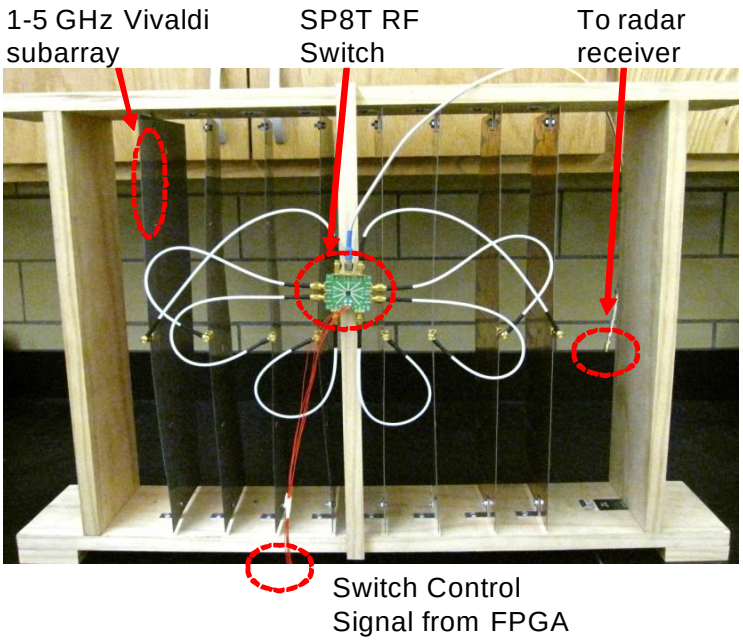

Figure 12 – 1 x 8 Vivaldi array, 2 to 10 GHz

In addition to the digital board, the Vivaldi antenna array of Figure 12 provided wide band response and narrow vertical beamwidth to reduce reflections from the floor or ceiling.

New Design Challenges

The new pulsed Doppler radar system was completely redesigned, primarily with mobility in mind. Hence, size was a major concern. It was geared towards wall-parameters estimation and limited imaging capability. The design was also required to provide either bistatic or monostatic operation. Surface mount components were necessary to replace cable type components. Special effort was directed towards finding a more efficient power amplifier that would not require the bulky heat sink or large power supply. The layout had to be optimized to develop two separate boards, one for the transmitter and one for the receiver. A better mixer was needed both to improve output spectrum flatness and for a simpler solution to the "I" and "Q" mixers on the receiver. Local Oscillator leakage needed addressing. Table 4 lists the main system description.

Table 4 – System description

	Mobile system
Capability	Through-wall localization Wall parameters estimation Limited, low resolution through-wall imaging
Frequency range	0.5 - 5.5 GHz, carrier at 3.125 GHz
Antennas	Broadband planar array of 64 Vivaldi antennas for receiver and Horn antenna for transmitter (bistatic mode) Horn antenna (monostatic mode)
Radar Waveform	Impulse
Size	8” (L) x 4” (W) x 2.5” (D)
Features	Very compact, simple structure but FPGA driven Monostatic or bistatic operation PCB off-the-shelf surface mount components Low power

Transmitter

Figure 13 shows the transmitter block diagram with summary power levels. Details for individual components will be discussed in the following sections.

Coplanar Waveguide

Co-planar waveguide (CPW) was used throughout this design for transmission lines because of its simplicity, quasi-TEM mode, low loss, robustness at low frequencies, and the availability of a ground plane for ease of connection to integrated circuit components. The equation for calculating the trace width and the air gap between trace and ground plane was given by Wen [10], involving complete elliptical integrals of the first kind. Numerous software programs are available to do this calculation, among them Agilent ADS. One practical solution resulted in a line width of 38 mils and air gap of 13 mils, assuming 20-mil Rogers RT Duroid 4350. For this material, the manufacturer reported a permittivity of 3.66 and loss tangent of .0037, a good choice because of its high frequency and low loss characteristics.

Figures 14 and 15 show HFSS simulated CPW, and Figure 16, the test board. Overall board dimensions for both simulation and testing were 2.5 in. square. All S parameter measurements were made with the Agilent E8363B Vector Network Analyzer (VNA).

Figure 17 shows S11 for simulated versus measured results of this planar transmission line, and Figure 18, S21. Return loss for CPW shows a good match and low loss to 10 GHz.

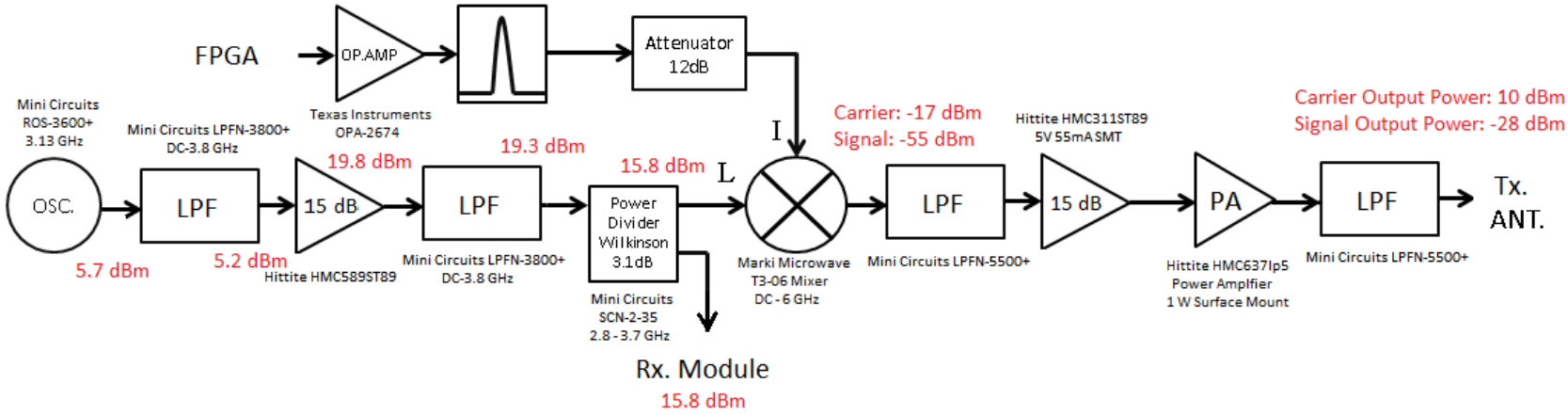

Figure 13 – Block diagram of new module transmitter with approximate power levels

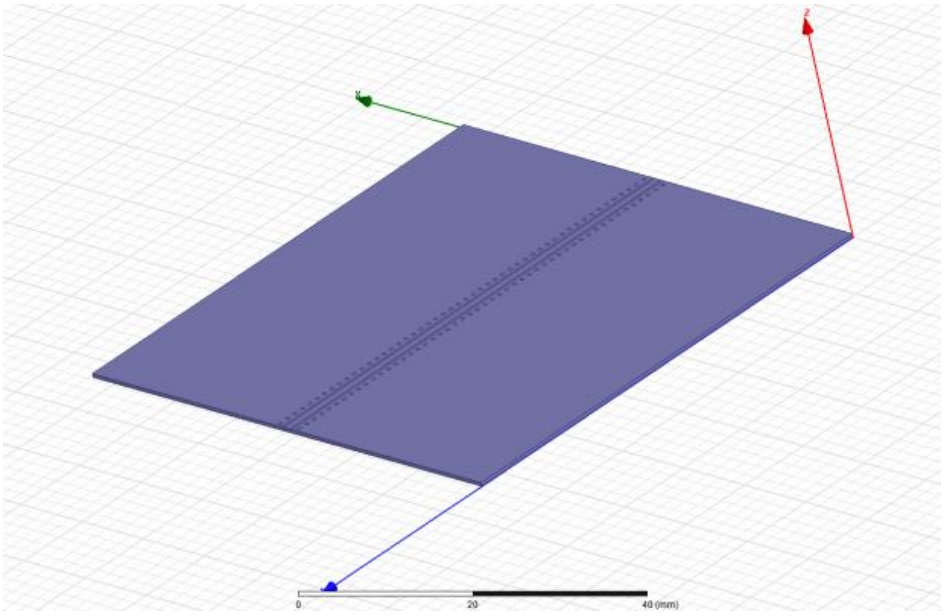

Figure 14 - Simulated CPW PCB

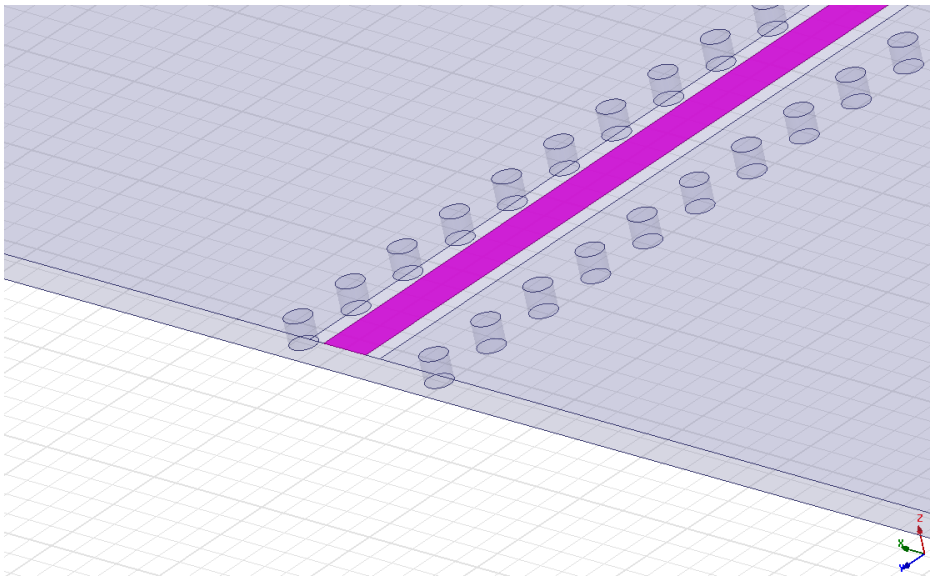

Figure 15 – Close up of the simulated transmission line

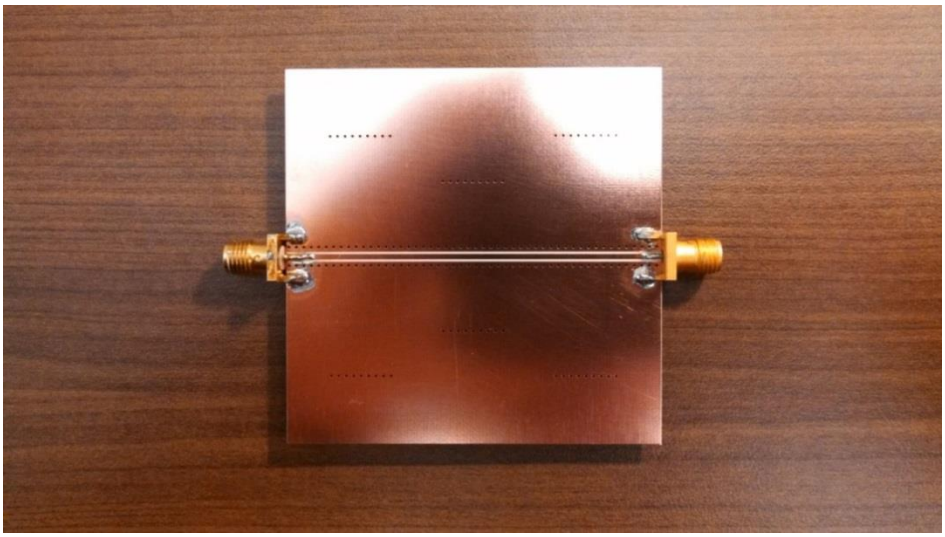

Figure 16 – CPW Test Board

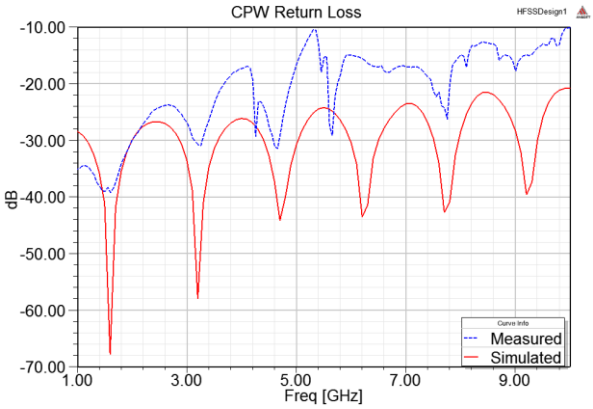

Figure 17 – Simulated and measured S11 for CPW PCB

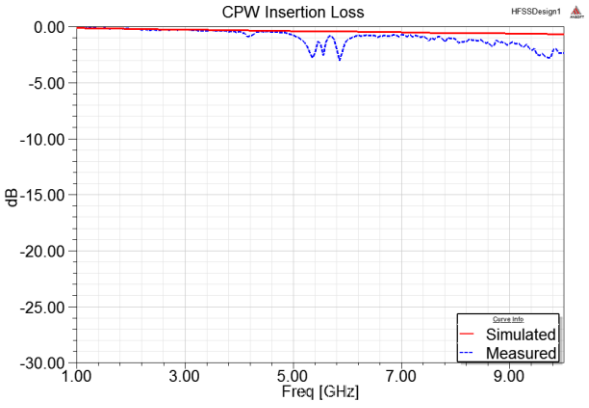

Figure 18 – CPW evaluated S21

Pulse Generator Network

The original prototype used a triggerable impulse generator from Hyperlabs, which can be seen in Figure 7, bottom left-hand side. In the new design a 10 MHz square wave (3.3V logic) from an FPGA-based controller board was amplified before driving a tunable Gaussian pulse generator capable of a 260 ps pulse-width. The pulse generator consisted of the Aeroflex-Metelics SMMD840 step recovery diode (SRD) and a Schottky MSS60 diode. The SMMD840 had a charge recovery time of 60 ps typical.

Square Wave Amplifier

The FPGA output could not source sufficient current to drive the Gaussian pulse generator. Thus the circuit schematic for the original square wave amplifier can be seen in Figure 19, and its printed circuit equivalent on the left side of Figure 20. A Texas Instruments Current Feedback op amp, the OPA 2674, provided a 220 MHz bandwidth and a maximum 500 mA output current.

The op amp circuit amplified the input square wave to approximately 3.6 Vp-p into 50Ω and level-shifted the output to an average zero volts DC. Figure 21 shows the input from the FPGA, a 10 MHz square wave with amplitude of 1.5 volts (tested using the Tektronix DPO 70804, 25 GSPS, with a 50Ω input impedance), and Figure 22, the circuit output.

Due to the large capacitor in the feedback loop of the op amp, LTSpice simulation in Figure 23 shows a charge time of almost 1.8 ms to reach the maximum peak-to-peak output. Note also the distortion in the rise and fall of the output signal (circled in red in Figure 22). To eliminate the capacitor, the circuit was modified as shown in Figure 24, with the addition of an op amp to provide DC offset bias. Since the OPA 2674 has two op amps in one package, no additional packages were needed. The more elegant solution provided better rise time characteristics, reduced output distortion and greater reliability.

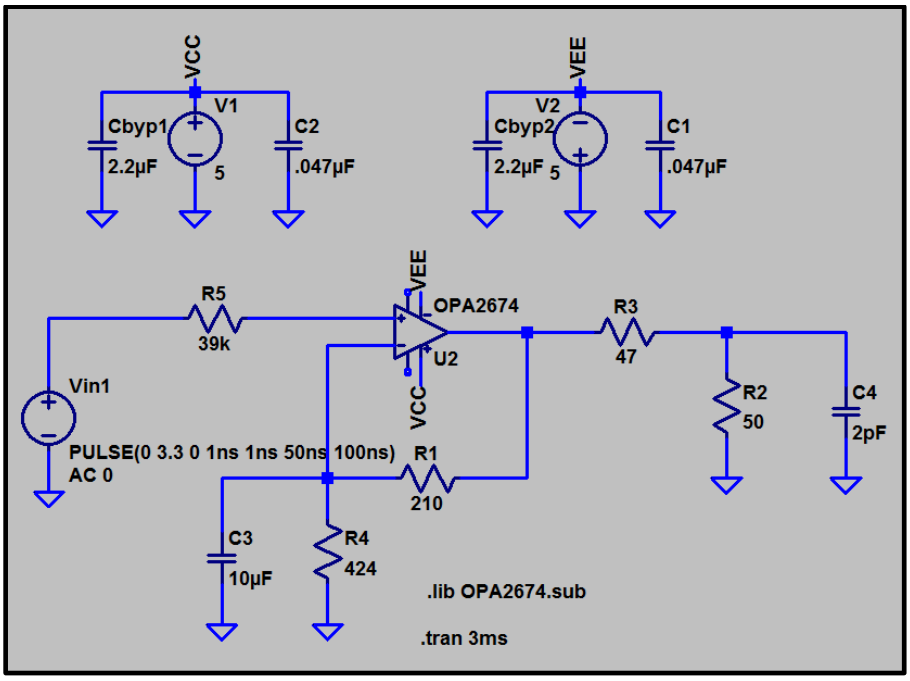

Figure 19 – Pulse generator driver

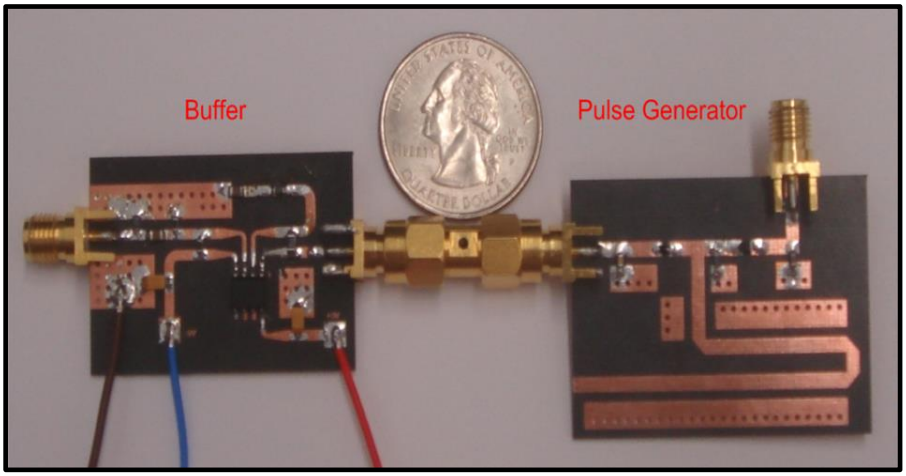

Figure 20 – Printed circuits to generate a Gaussian pulse

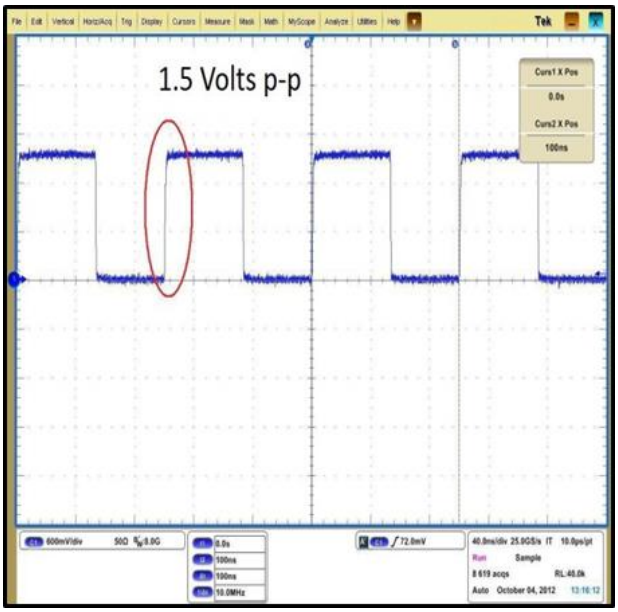

Figure 21 – FPGA 10 MHz clock output

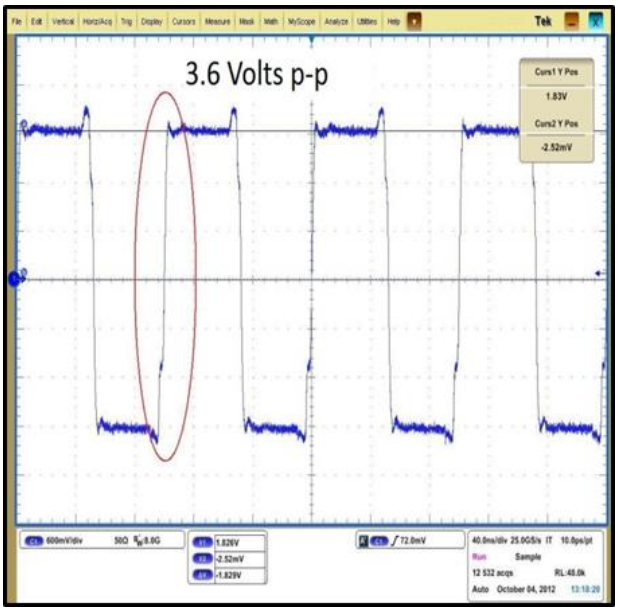

Figure 22 – Buffer amplifier output

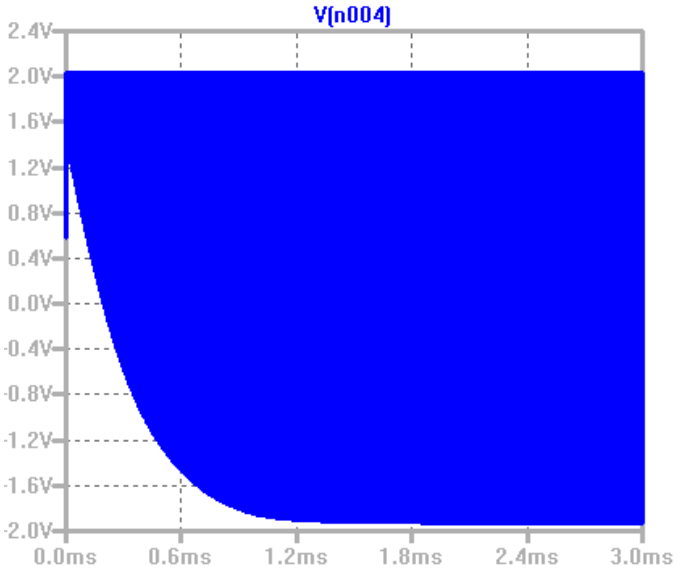

Figure 23 – LTSpice simulation of original op amp circuit

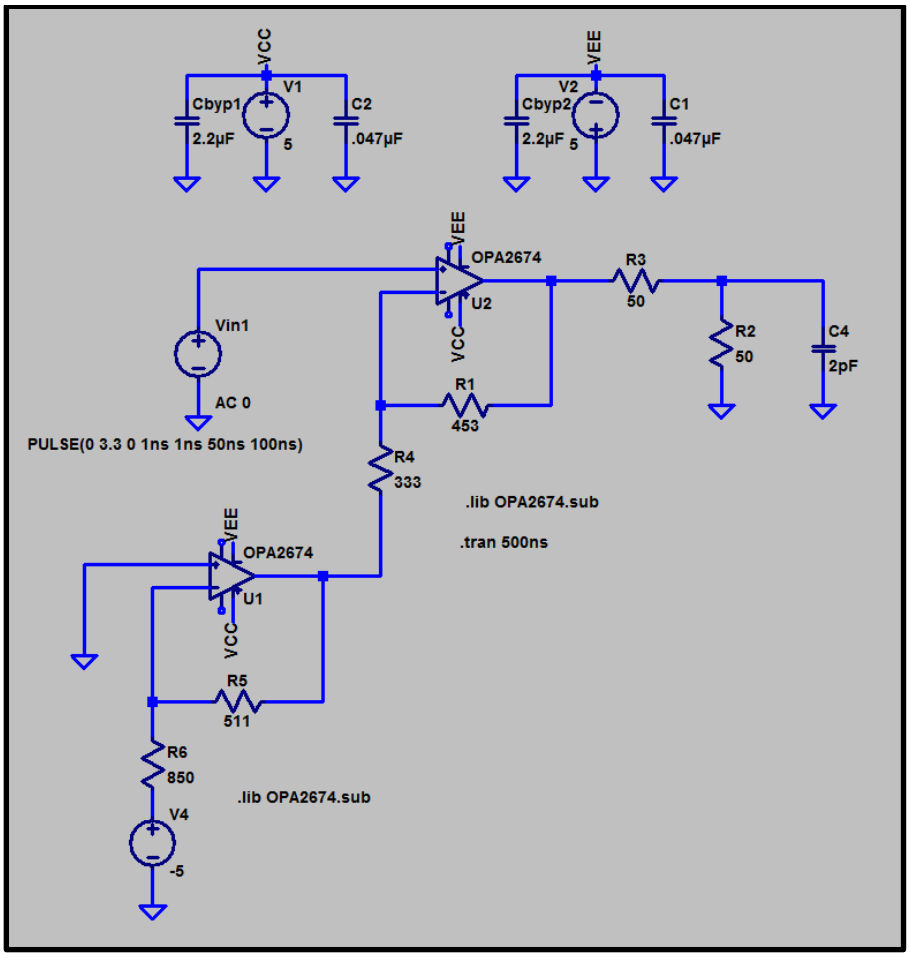

Figure 24 – Improved buffer to drive Gaussian pulse generator

The simple gain equation for the circuit of Figure 24 is:

$$V_o = 0.5 * \left[V_{in} * \left(1 + \frac{R_1}{R_4}\right) + (-5) * \left(-\frac{R_5}{R_6}\right) * \left(-\frac{R_1}{R_4}\right)\right] \tag{39}$$

The additional op amp, shown in the figure as "U1", has negligible closed-loop output resistance of 0.01Ω, so its introduction will have no effect on the overall gain of the network.

Pulse generator

The Agilent ADS model of Figure 25 shows the schematic of the pulse generator printed circuit, shown on the right side of Figure 20. The generator consists of a fast step-recovery diode (SRD) fabricated in a 50Ω microstrip transmission line and a microwave stub. A thorough explanation of this circuit can be found here [11]. The amplified square wave input to this circuit turns the SRD on and off. The resulting fast positive and negative-going pulses are reflected by the stub and combined at the transmission line. The length of the stub determines the pulse width.

Simulation results in the time and frequency domain are shown in Figures 26 and 27. The plot of ADS simulation in Figure 26 shows a pulse width of approximately 240 ps, with a -10 dB bandwidth in Figure 27 of 3.1 GHz.

Figure 28 shows the measured frequency spectrum of the pulse with a -10 dB bandwidth of 2.5 GHz, good correlation to the ADS simulation.

The generated pulse train, Figure 29, contains fast, periodic pulses with a half-max width of 260 ps and a voltage peak of 900 mV. These narrow pulses (Figure 30) provide good image resolution and better range and location accuracy.

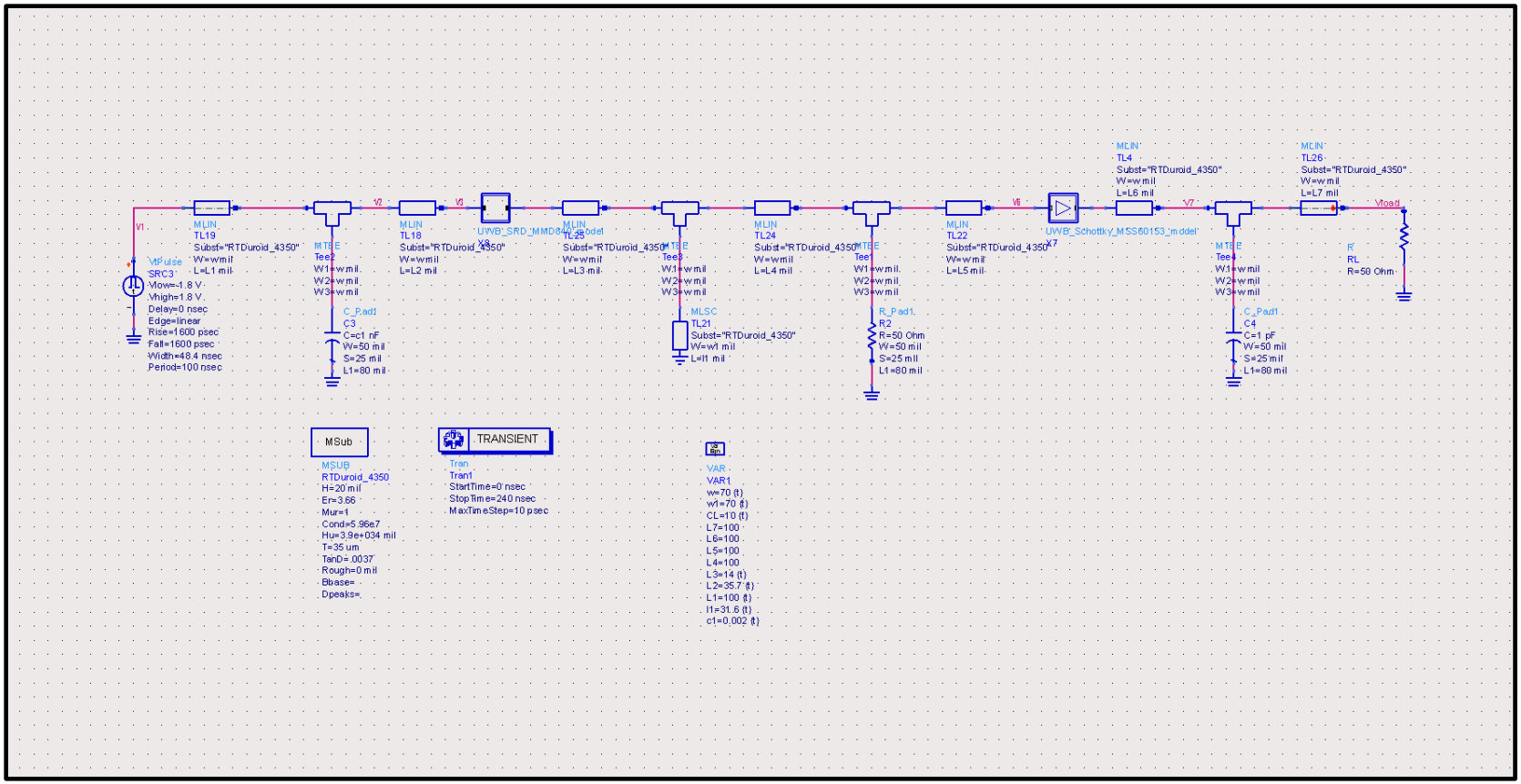

Figure 25 – Agilent ADS pulse generator model

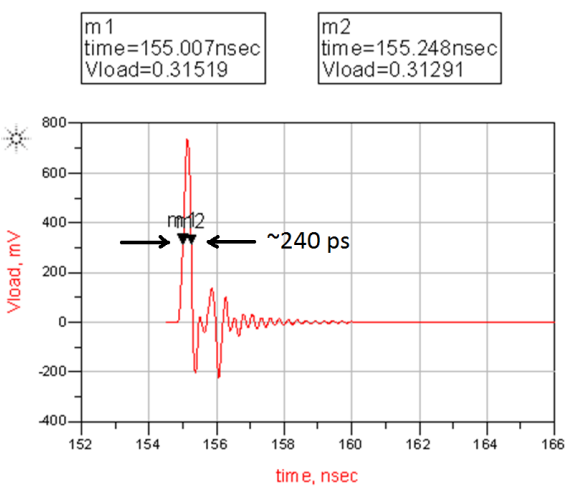

Figure 26 – Simulated pulse generator output

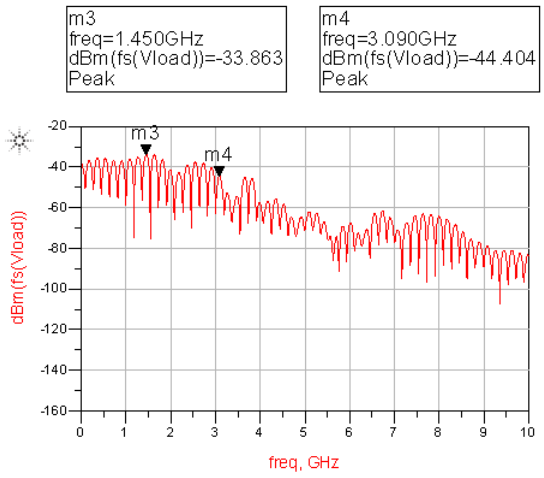

Figure 27 – Pulse generator frequency output

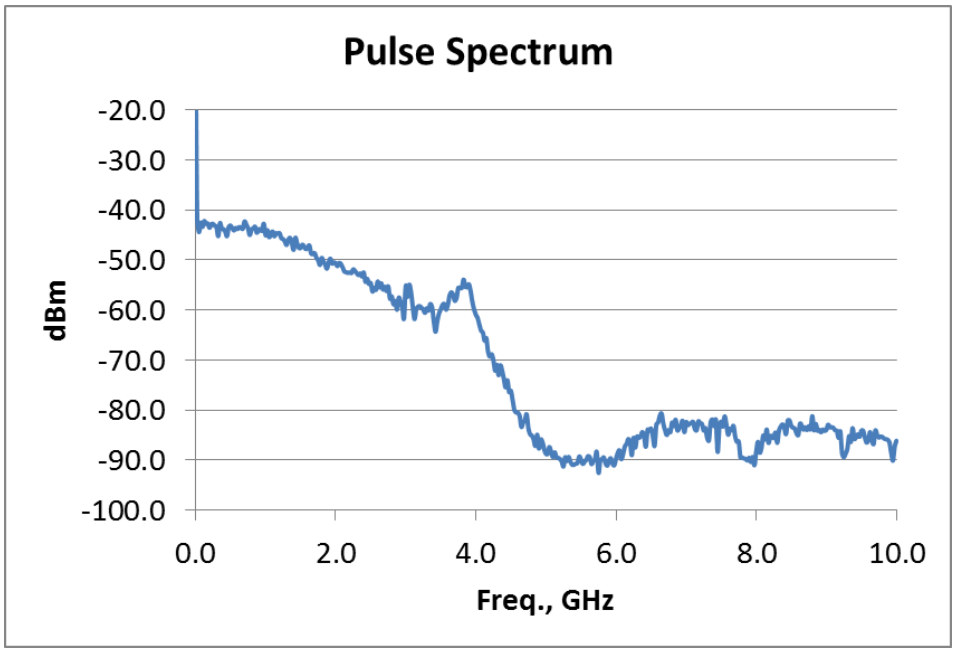

Figure 28 – Measured pulse output spectrum

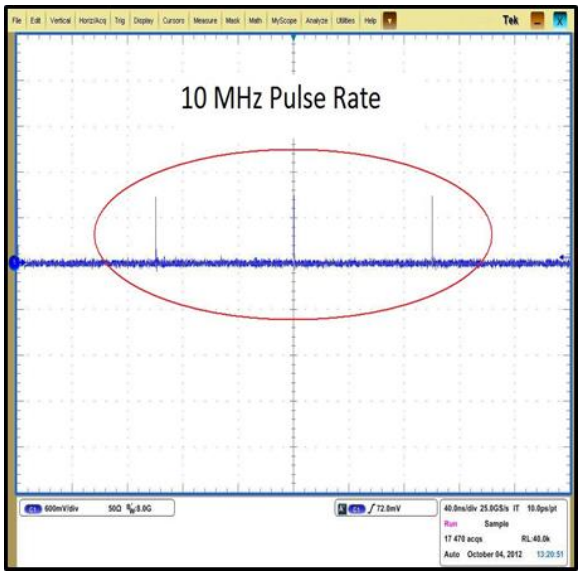

Figure 29 – Pulse generator output at 10 MHz

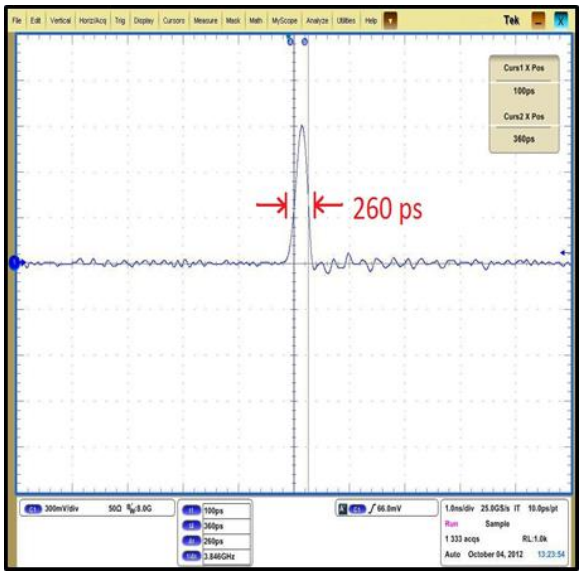

Figure 30 – One pulse, demonstrating 260 ps pulse width

Pulse Analysis

An approximate Fourier series transformation of the Gaussian pulse in Figure 30 provides useful frequency domain information for this system.

The transform for a square pulse of width w and period T_0 is

$$rect\left(\frac{t}{w}\right) * \delta_{T_0}(t) \longleftrightarrow \left(\frac{w}{T_0}\right) sinc\left(\frac{wk}{mT_0}\right)\delta[k], -\infty \leq k \leq \infty, \frac{k}{m}\, an\ integer \qquad (40)$$

Thus, in the frequency domain, the square pulse approaches an infinite series of 10 MHz signals with sinc function amplitude variation. Instead of using a rect function however, a Gaussian equation gives a better description.

$$v(t) = V_0 * e^{-a(t-t_0)^2} \qquad (41)$$

Let equation (41) describe the pulse generator output in the time domain. Then the Fourier series transform is [12]

$$F(k) = V_0\sqrt{\frac{\pi}{a}}e^{-\pi^2 k^2/a} \tag{42}$$

which is another Gaussian. Therefore the envelope of the pulse spectrum will follow a Gaussian curve, scaled by a constant in magnitude and frequency, and directly set by the pulse width of the source. Note also that since $a = 1/\tau$ sets the pulse width of the Gaussian time domain function, the frequency domain is π^2/a, or approximately ten times the inverse of the pulse width. Again, this broad bandwidth provides short wavelength impulses and therefore greater accuracy for localization and wall characterization.

Attenuator

The surface-mount attenuator of Figure 31, the Mini-Circuits PAT-12+, replaced a Mini-Circuits VAT-12 sma-type attenuator. The new 12 dB attenuator at the output of pulse generator provided a 50 ohm load as well as good matching for the mixer. It was broadband, with flatness of 1.5 dB and VSWR of 1.15 from DC to 7 GHz .

Figure 31 – Attenuator comparison, with the new attenuator on the right

Oscillator

A Mini-Circuits ROS-3600-1119 voltage controlled oscillator (VCO) replaced the Mini-Circuits ZX96-3360+ shown in Figure 32. It produced the 3.13 GHz carrier, and because of its non-linear nature, multiple harmonics. An evaluation board was fabricated to test the part, as shown in Figure 33.

Results are shown in Table 5, and a plot of output frequency and power versus input control voltage, Figure 34. An Agilent D5044 DC – 33 GHz Spectrum Analyzer provided frequency measurements.

From Table 5, the oscillator generated a 3.1 GHz signal with output power of 5.74 dBm. The first and second harmonics were 25 and 33 dB below the fundamental.

Figure 32 – Original VCO

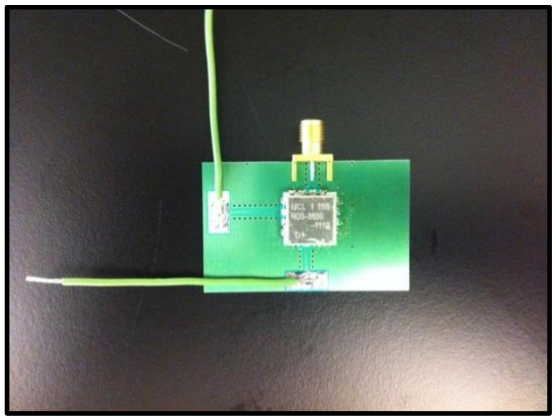

Figure 33 - VCO and evaluation board

Table 5 – VCO Output

Mini-Circuits ROS-3600-1119 Voltage Controlled Oscillator (VCO)						
	Fundamental		1st Harmonic		2nd Harmonic	
V (tune)	Freq. (GHz)	Power (dBm)	Freq.	Power (dBm)	Freq.	Power (dBm)
0	2.75	6.55	5.45	-15.24	8.125	-35.8
2	2.9	6.13	5.8	-18.82	8.7	-46.6
4	3.1	5.74	6.2	-19.28	9.25	-26.9
6	3.3	5.38	6.55	-19.66	9.83	-37.5
8	3.45	4.8	6.95	-17.83	10.39	-54
10	3.65	4.11	7.25	-18.58	10.87	-37.8
12	3.75	2.74	7.55	-21.66	11.29	-33.4

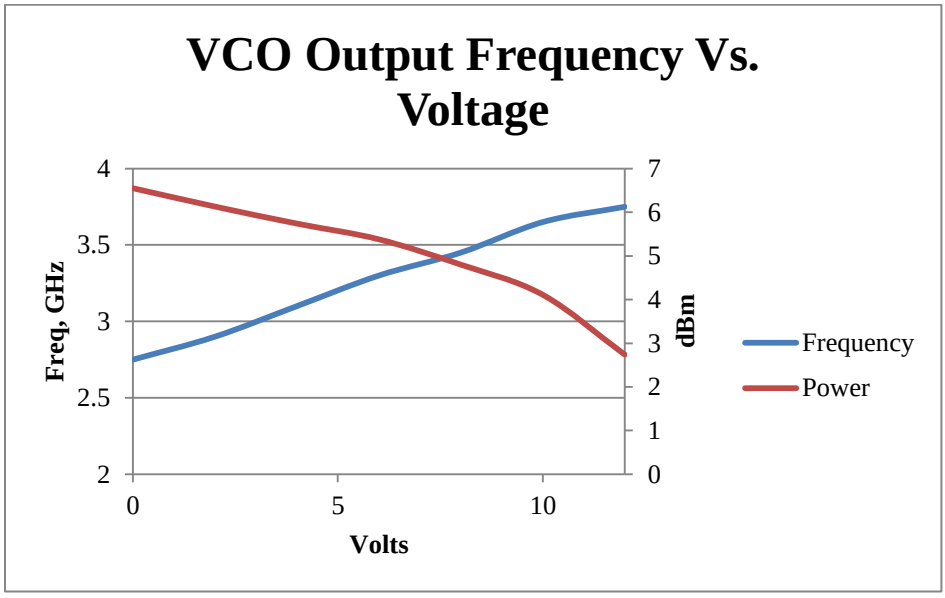

Figure 34 – Mini-Circuits ROS-3600 evaluation board results

Low Pass Filter (Mini-Circuits LFCN-3800D+)

To reduce VCO generated first and second harmonics to acceptable levels, two Mini-Circuits LFCN-3800+ low pass filters were inserted, the first after the VCO, and the second after the first gain block. With a slightly higher passband than the LFCN 3400+, it provided lower insertion loss at the carrier frequency while still generating excellent insertion loss at the first harmonic. For the evaluation board shown in Figure 35, tests showed a 0.7dB pass-band insertion loss and 14.5 dB return loss at 3.1 GHz. This simple device achieved 34dB first harmonic rejection and 36dB second harmonic rejection. A plot of the filter response is shown in Figure 36.

Hittite HMC589ST89 Gain Block

The Hittite HMC589ST89 Gain Block supplied +17.4 dB gain at 3.125 GHz with acceptable return loss (better than 10 dB) and output isolation (better than 20 dB), as shown in Fig. 37. Its 1 dB compression output power of +19dBm provided sufficient power to drive the mixer.

Mini-Circuits Ceramic Power Splitter

The Mini-Circuits SCN-2-35 power splitter demonstrated low return loss and 0.48 dB average insertion loss to each of its output ports, Figures 38 and 39. It had close phase agreement of 0.17 degrees between ports and its convenient size made it useful for splitting carrier power between the mixer and receiver board.

Local Oscillator (LO) Results

Figure 40 displays the resultant LO energy generated for the mixer. The plot shows a +15.75 dBm carrier at 3.125 GHz. The first harmonic of 6.25 GHz has been attenuated below the noise floor of the Spectrum Analyzer. A second harmonic at 9.375 GHz exists but was inconsequential due to the system bandwidth.

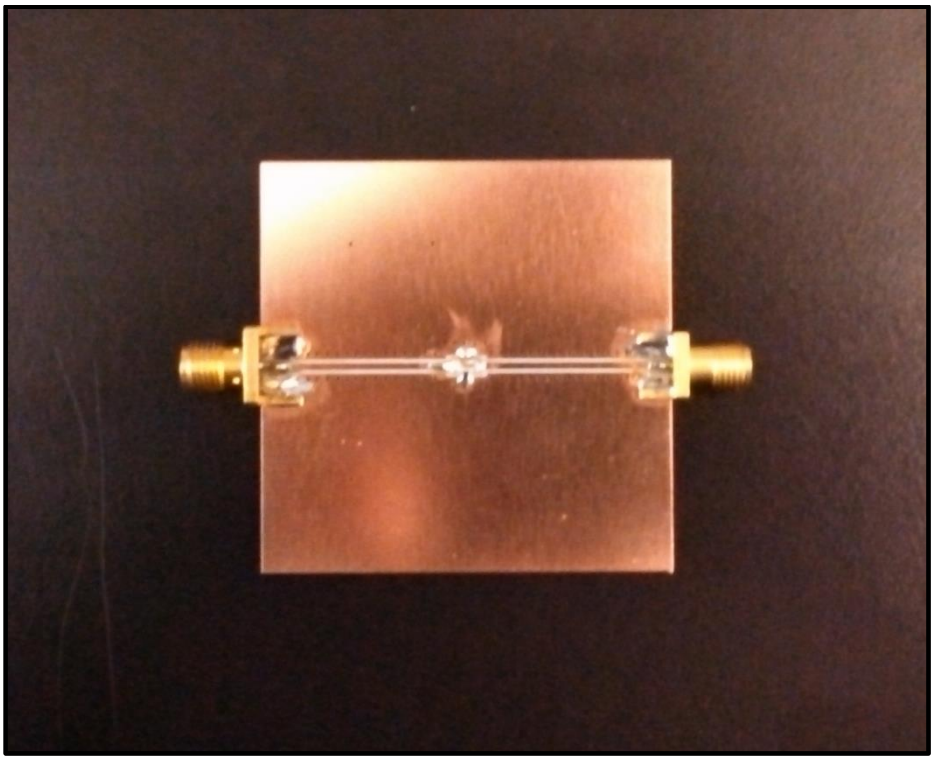

Figure 35 - Evaluating the LFCN-3800+

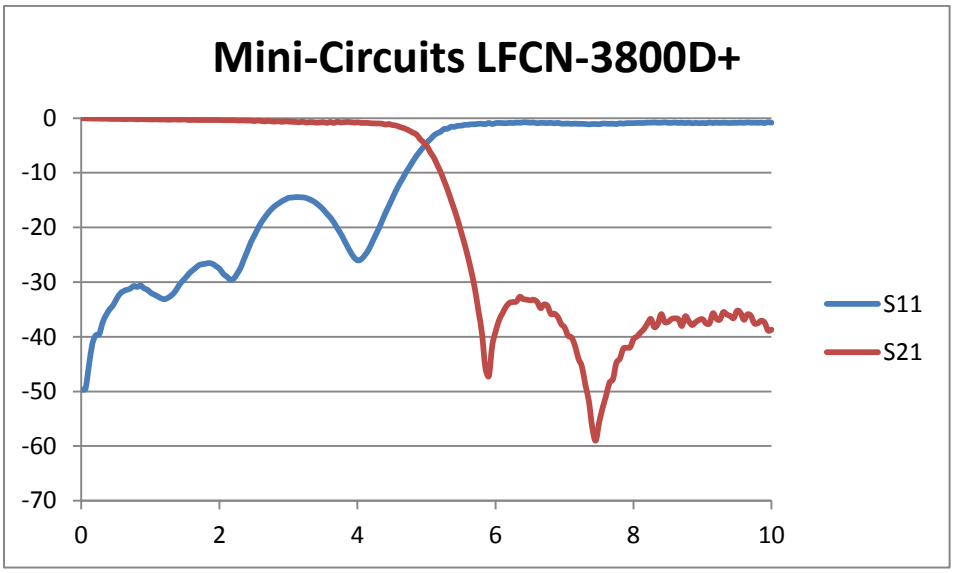

Figure 36 – Measured Mini-Circuits low pass filter return and insertion loss

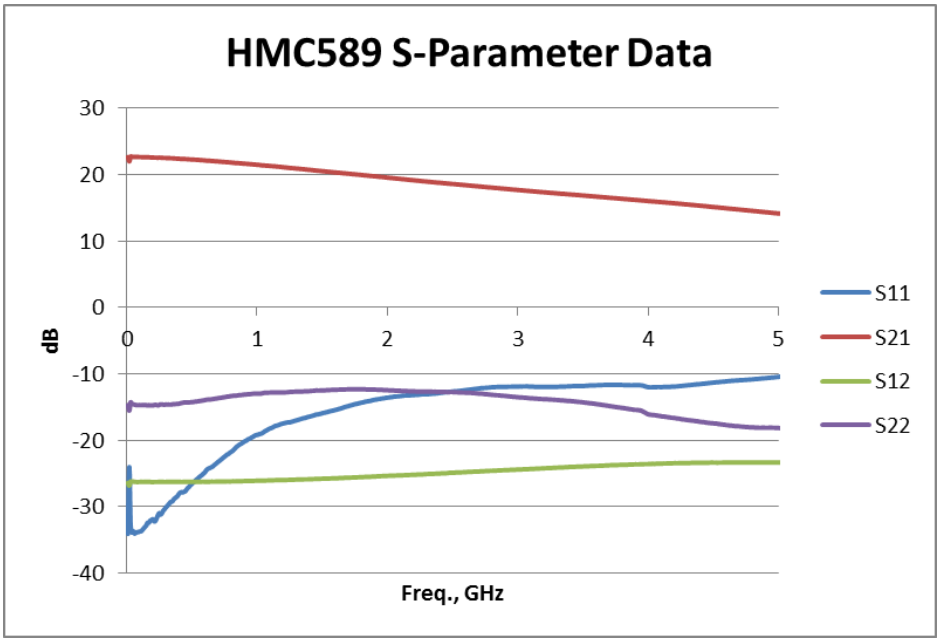

Figure 37 – The Hittite HMC589 gain block S-parameter data

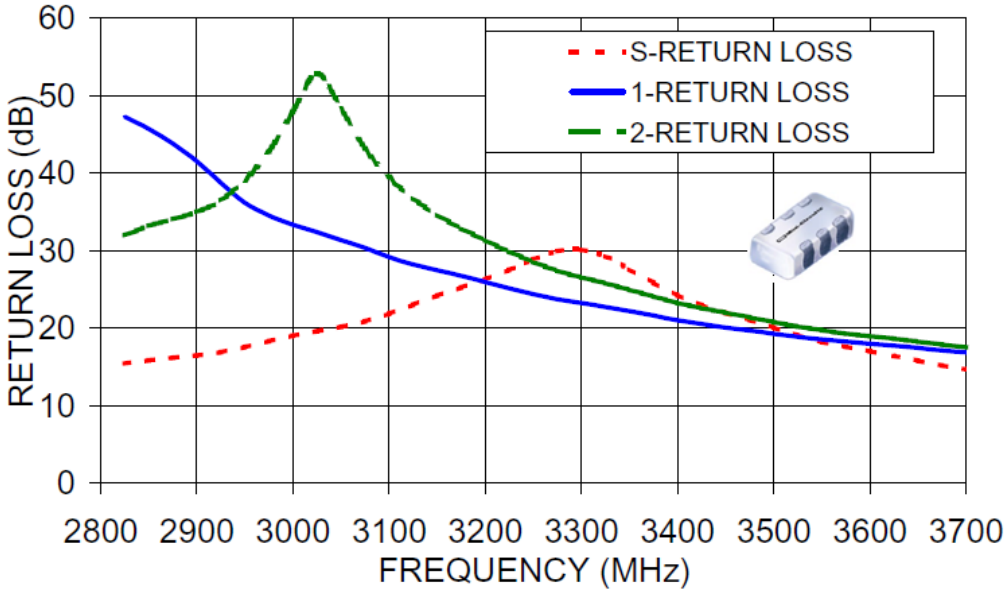

Figure 38 – Mini-Circuits SCN-2-35 power splitter data

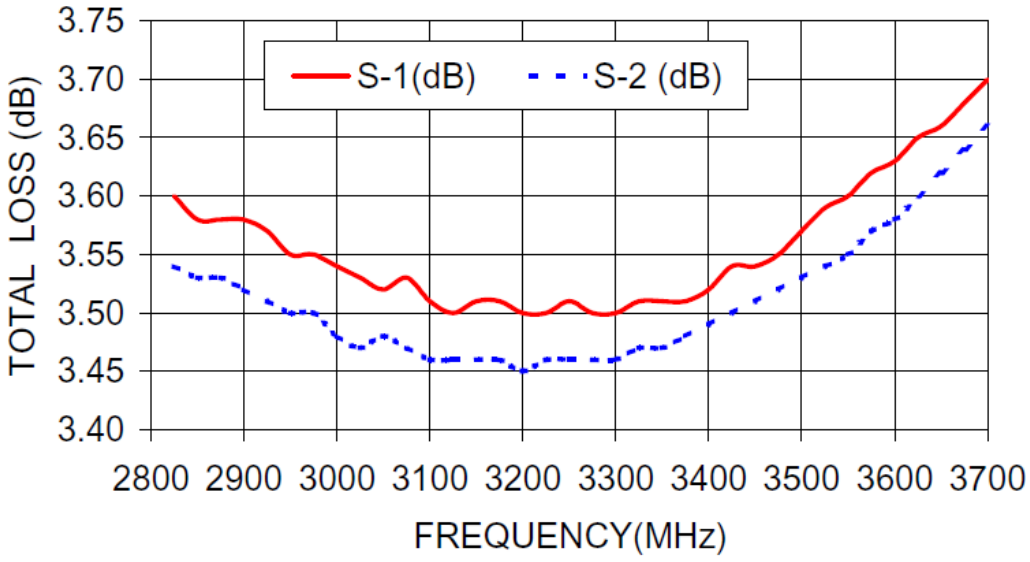

Figure 39 – Insertion loss for the power splitter

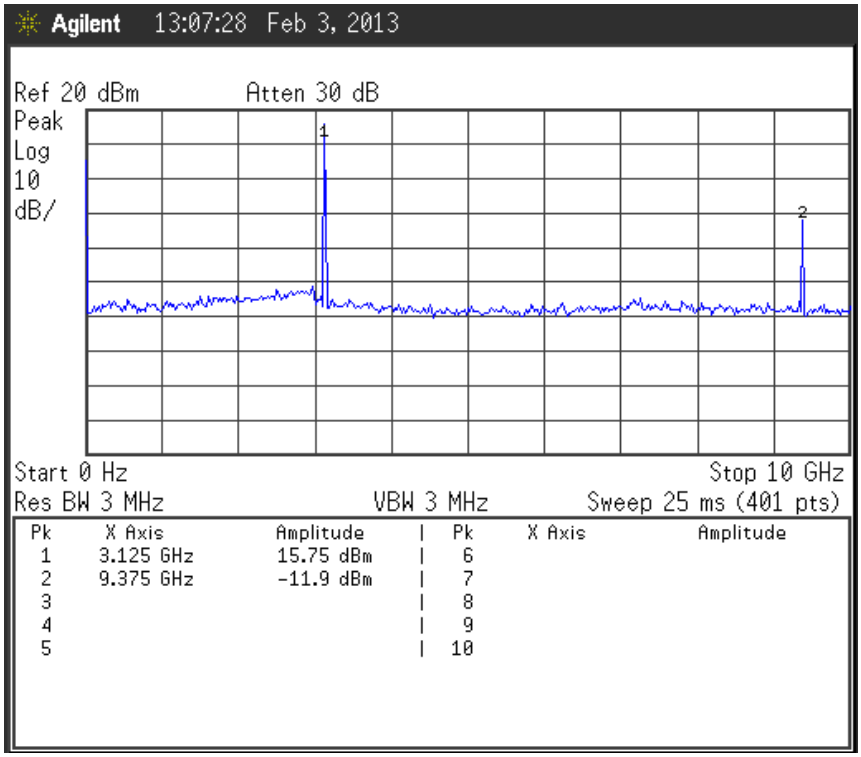

Figure 40 – Generated LO power for mixer up-conversion

Mixer

The broad frequency spectrum of the Gaussian pulse required a mixer with a relatively flat conversion loss response from DC to 6 GHz. Previous mixers are shown in Figures 41 and 42. The surface-mount Mini-Circuits MAC-60+ mixer was inexpensive, but had limited IF response. Marki Microwave makes a good surface mount device, the T3-06LCQ, as shown in Figure 43. Besides its flat conversion response from DC to 6 GHz, the mixer had 33 dB of isolation from LO to RF ports at the carrier frequency. The broad bandwidth and flat conversion response were a significant improvement from the previous mixers used in the cabled/connector-type prototype. The device had a higher LO power requirement of +15 dBm, but this was easily achieved, as previously mentioned, by the addition of the Hittite HMC589 gain block.

Figure 41 – The Miteq-0208 3 GHz mixer

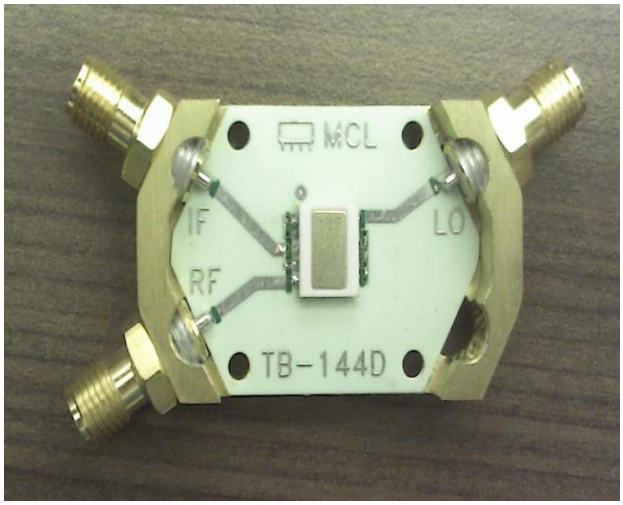

Figure 42 – Mini-Circuits MAC-60+ mixer

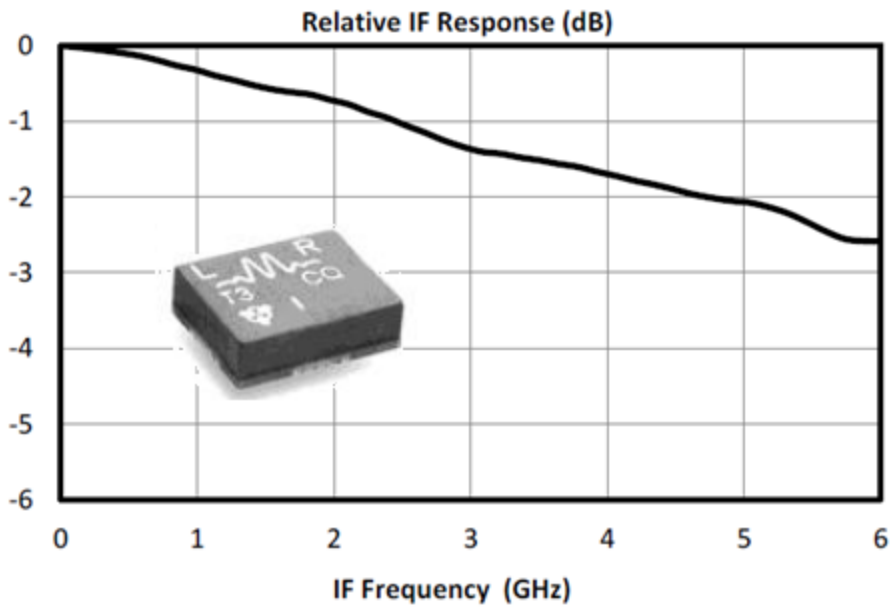

Figure 43 – Marki Mixer conversion loss as a function of IF input frequency, from data sheet

Low Pass Filter (LFCN-5500+)

After up-conversion by the Marki mixer, harmonics above the bandwidth of the pulse-modulated carrier required filtering. Figure 44 shows the Marki mixer output while being driven by a +15.7 dBm carrier and the pulse generator with a 6 dB pad. Resulting first and second harmonics were at similar power levels to the carrier. Two Mini-Circuits LFCN-5500 low pass filters were inserted, one after the mixer and another after the Power Amplifier (PA), to help reduce them.

Hittite HMC311ST89 Gain Block

This amplifier was chosen for its excellent gain response and power output capabilities from DC to 6 GHz. Typical gain of 15 dB was achieved with a flatness of ± 1dB and a 1dB compression of +15 dBm.

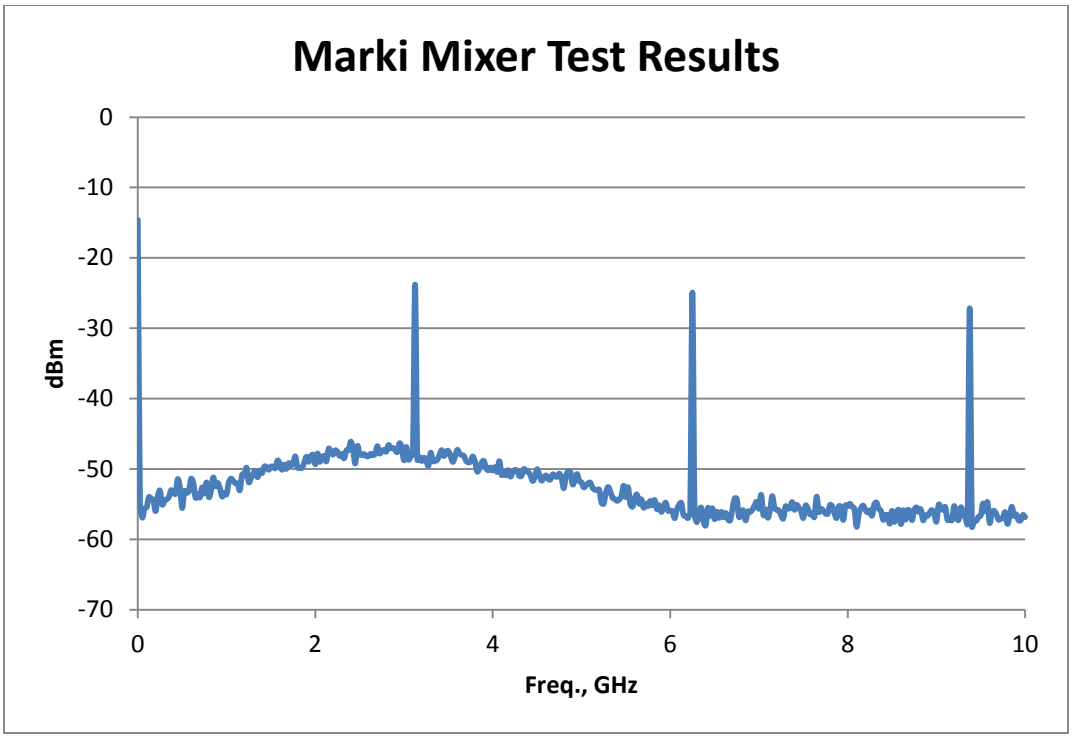

Figure 44 – Mixer output showing multiple harmonics

Hittite HMC637LP5 Power Amplifier

The original power amplifier used in the cabled/connector-type prototype is shown in Figure 45. It was 7.5" W x 1.68" W x 3.6" H, including the necessary heat sink, and required 14 watts of power for +30 dBm output. In addition, it had limited response below 2 GHz. Hittite makes the HMC637LP5 in a 25 pin QFN, 0.2" square package. It has a gain of 13dB and gain flatness of ±0.75dB from DC to 6 GHz, besides consuming a maximum of 4.8 watts for a +29dBm power output.

Measured results are shown in Figures 46 and 47. The Hittite-supplied evaluation board and accompanying DC block and bias tee are shown in Figure 48, with the chip mounted in the middle of the evaluation board.

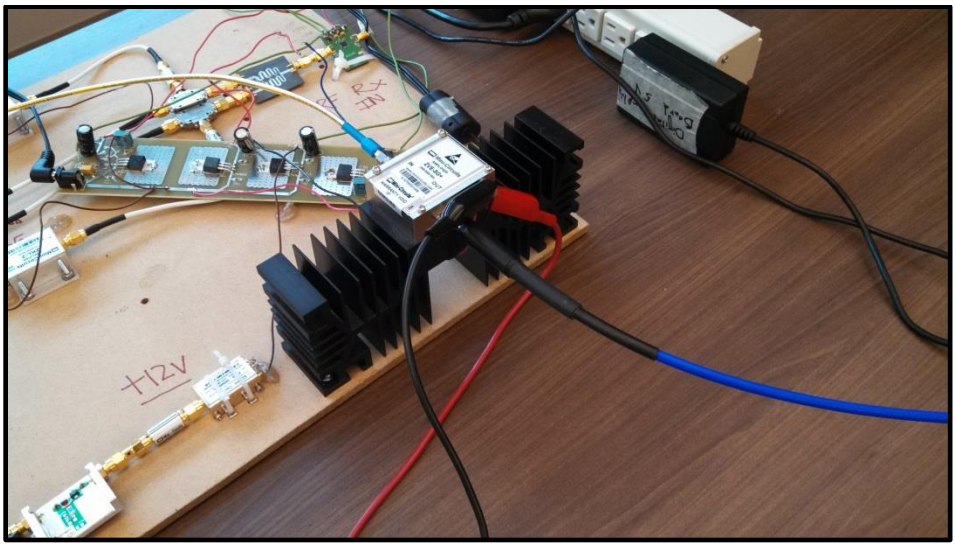

Figure 45 – The original power amplifier

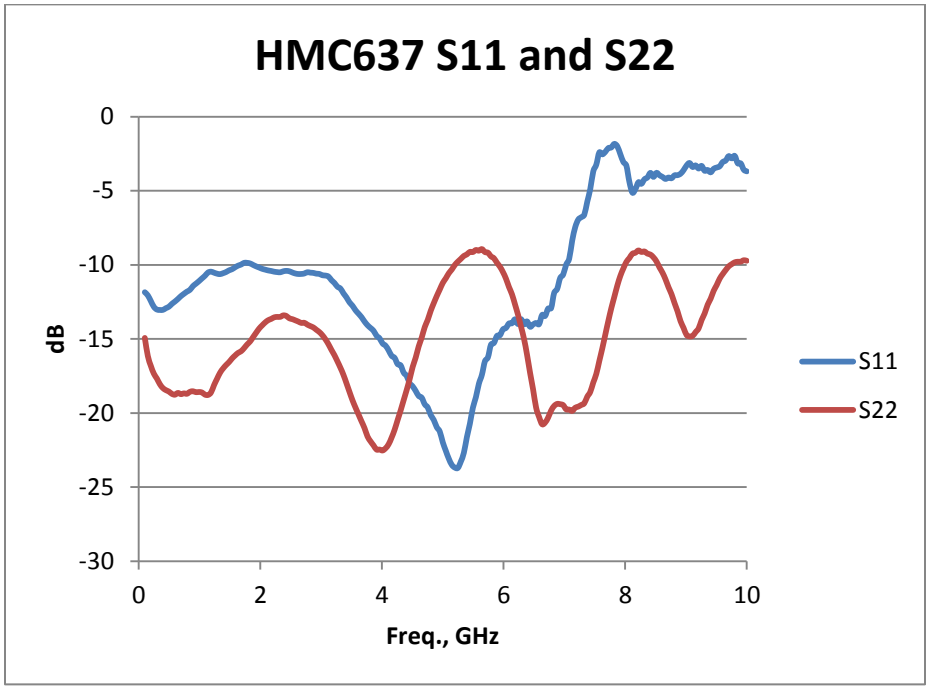

Figure 46 – Measured input and output return loss for the Hittite PA

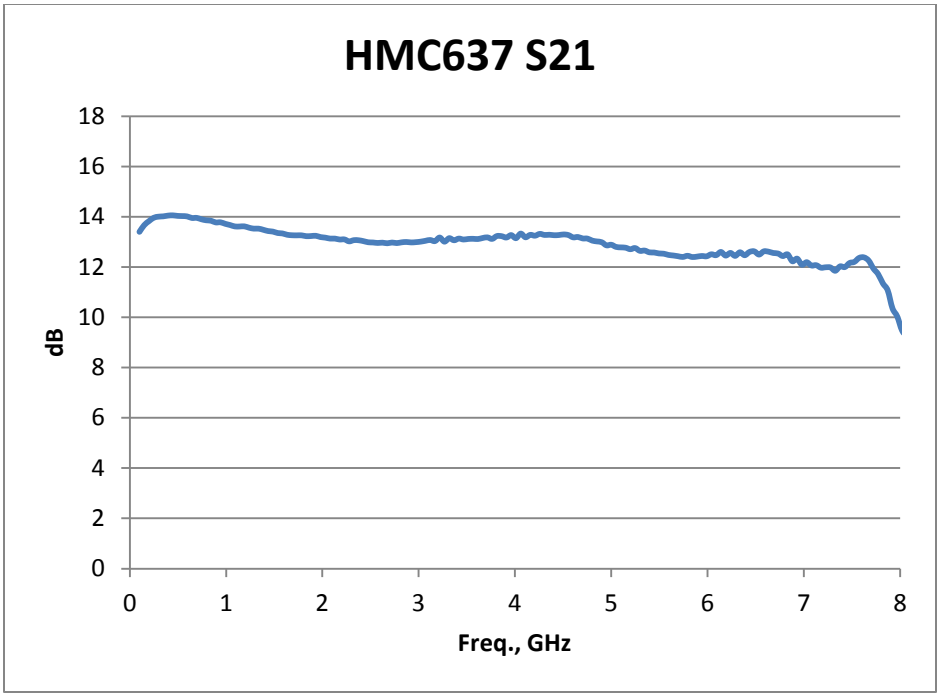

Figure 47 – Power gain for the PA

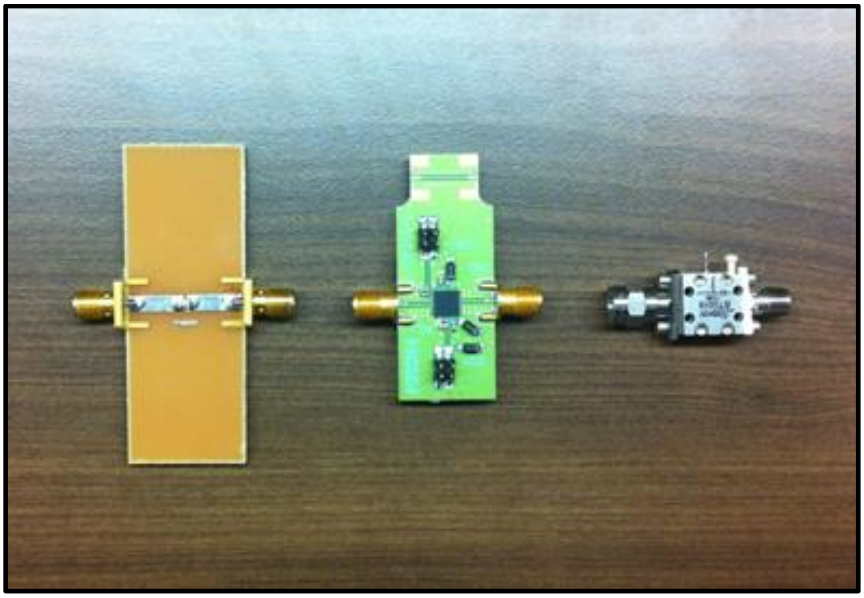

Figure 48 – DC block, Hittite evaluation board, and bias tee

Transmitter results

The transmitter PCB output is shown in Figure 49. The pulse spectrum is exceptionally flat from 1.5 to 4.5 GHz, and the -10 dB bandwidth is excellent, from 0.7 to 5.6 GHz. This compares well to the ADS simulation from Figure 27, which predicted an upper -10dB bandwidth of 6.2 GHz. However, the carrier and first harmonic are high at +9 dBm and -7 dBm respectively. Work on these issues is discussed in Chapter 5.

The transmitter PCB is shown in Figure 50. The board measures 2.25" W x 6.5" L, well within established criteria for the final module dimensions of Figure 8.

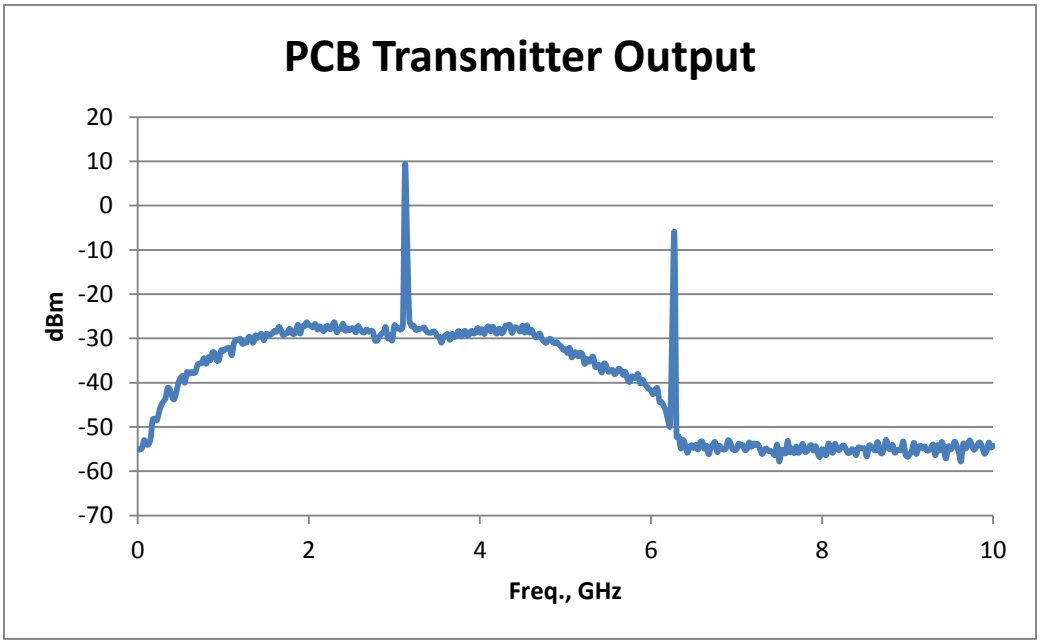

Figure 49 – The PCB transmitter output

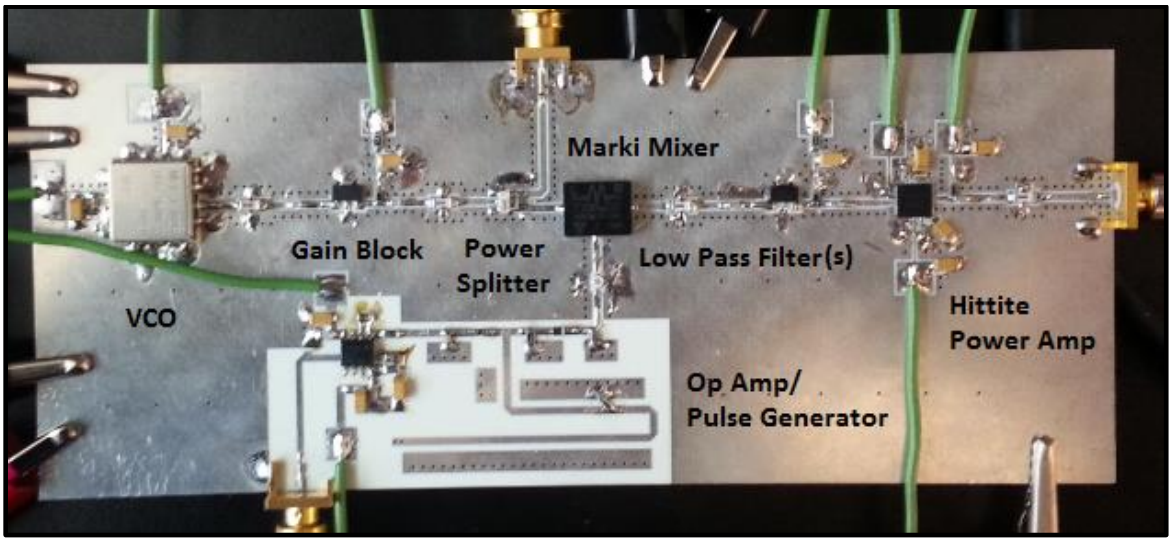

Figure 50 – STW transmitter PCB

Receiver

At the receiver, in bistatic mode, a Vivaldi antenna array is moved electronically to gather energy reflected by an object from the transmitted pulse. The energy is amplified by a Low Noise Amplifier (LNA), then split into separate "I" and "Q" channels via two Marki mixers and supplied carrier input power from the transmitter PCB. See Figure 51. The output from the mixers is filtered and amplified, then acquired by an Analog-to-Digital converter on a separate Digital Controller board. Once acquired, the data is stored, digitally filtered and passed through a microwave beam-forming algorithm to recover a 3-D image. The image can then be displayed on a PC for viewing.

Low Noise Amplifier

The Hittite HMC753LP4, a GaAs MMIC chip mounted in a 24 pin QFN package, provided a good noise factor of 1.7 dB and a gain of 15.5dB into 50Ω. It had excellent gain flatness (measured) of ±0.5 dB from 1 to 6 GHz, and good return loss, as seen in Figures 52 and 53.

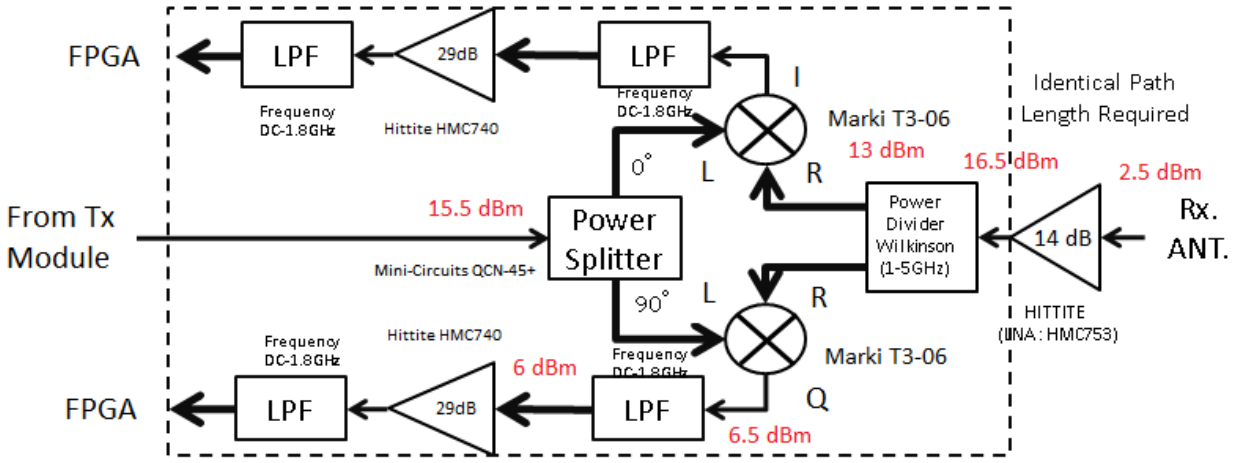

Figure 51 – STW module receiver block diagram

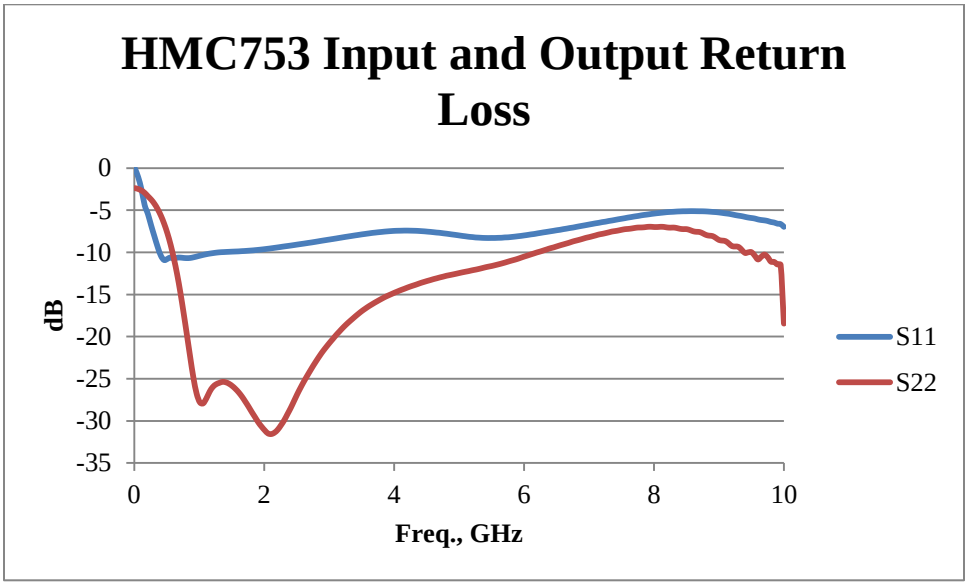

Figure 52 – Receiver LNA test results

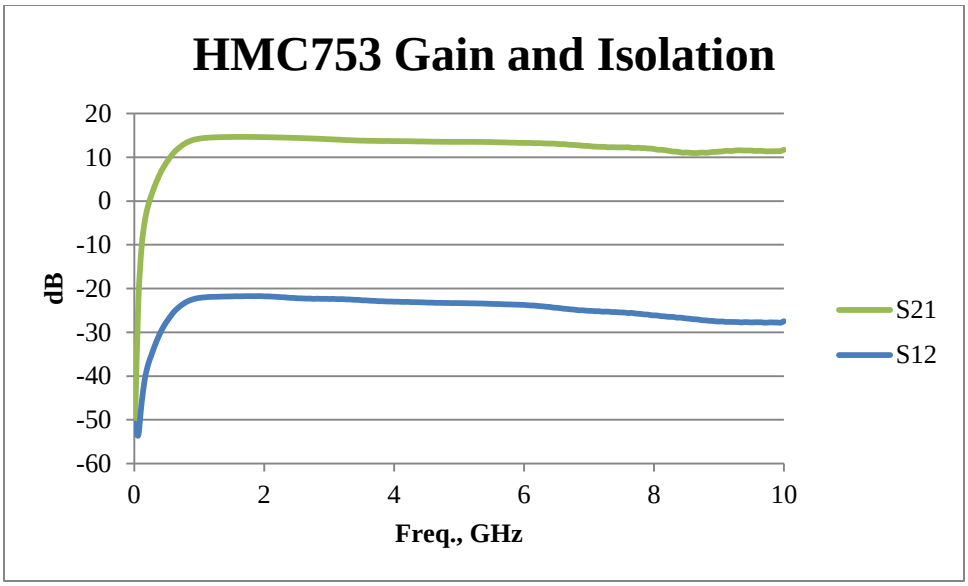

Figure 53 – LNA gain

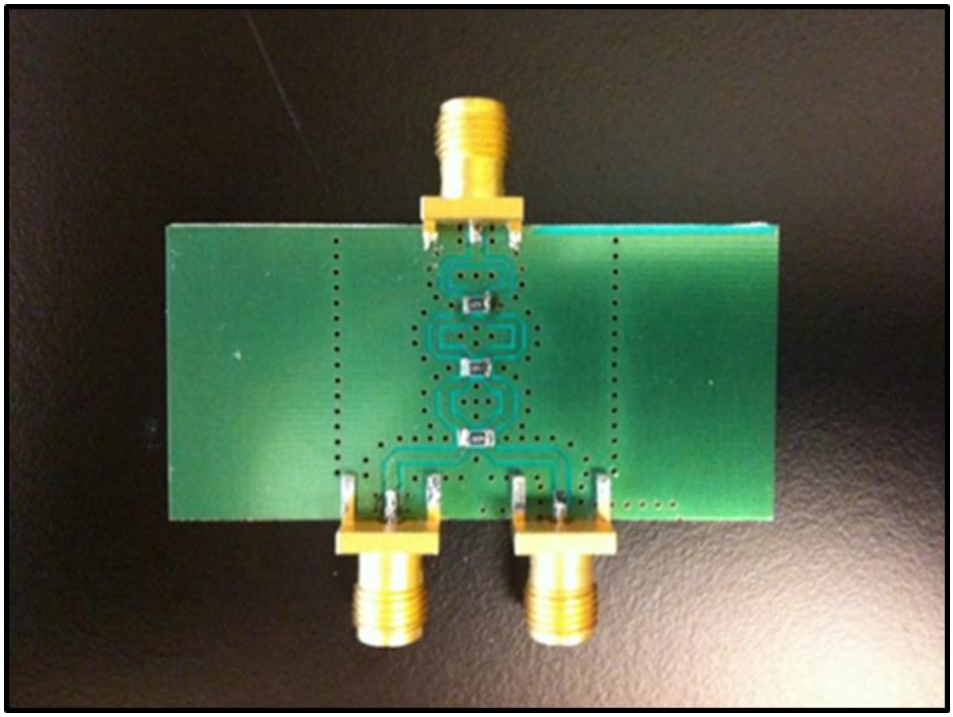

Figure 54 – Wilkinson power splitter

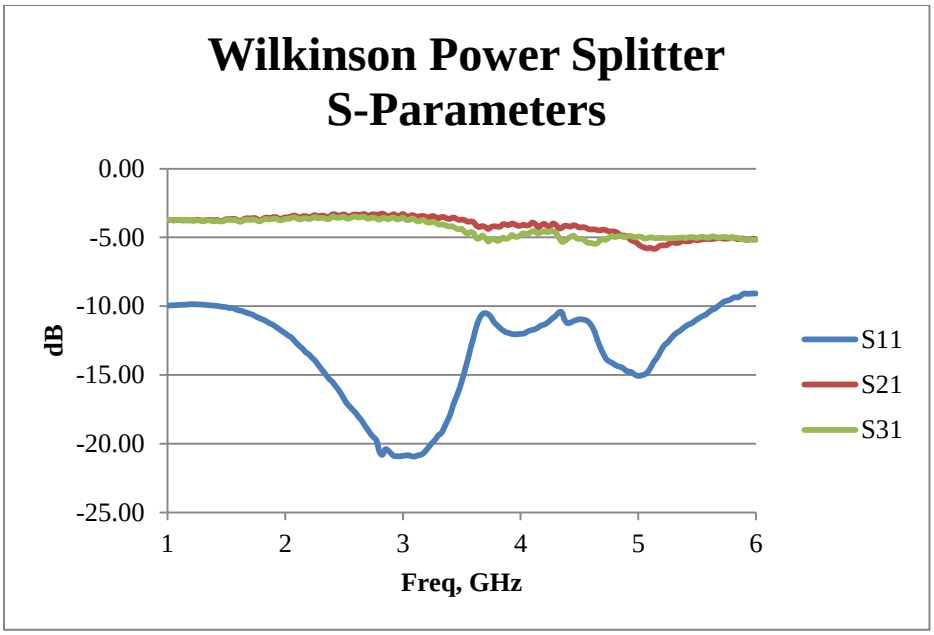

Figure 55 – Measured results from test board

Wilkinson Power Splitter

The planar circuit of Figure 54 was fabricated due to the need for the large bandwidth of the received pulse. Figure 55 shows the -10dB bandwidth of 1 to 5.5 GHz and about ±1dB insertion loss.

Marki Mixers

The dual Marki down-converting mixers utilized on the receiver are identical to the Marki T3-06 mixer used as an upconverter on the Transmitter Board. Their excellent linearity, broadband IF and RF response, and good isolation make them a premium choice for this application.

Fig. 51 shows the receiver block diagram with two channels, each channel containing phase information necessary to produce accurate localization data. Legacy design called for two separate, identical mixers, and due to their pin-out constraints, two separate printed circuit boards. However, the Marki mixers have a simple pin option that places the Intermediate Frequency (IF) output on either side of the surface mount device. The separate package options have phase agreement within ten degrees. This

convenience reduces overall module complexity, size and cost, by reducing the design to one receiver PCB instead of two.

Gain Block

The Hittite HMC740ST89 provides relatively flat gain from DC to 2 GHz, with reasonable gain above 3 GHz. Not shown in the receiver schematic above but pictured in Fig. 56 below, each I and Q channel has two of these amplifiers connected in series. Gain from each of these amplifiers is 14.5dB average. Measured S-parameters for this amplifier can be seen in Figures 57 and 58.

Quadrature Power Splitter

The Mini-Circuits QCN-45+ provided a phase-shifted carrier of 0° and 90° to the Marki mixers. It has better than 15dB return loss, less than ±0.5dB amplitude imbalance and an error of less than 3° between ports. The evaluation board, phase and S-parameter measurements are shown in Figure 59.

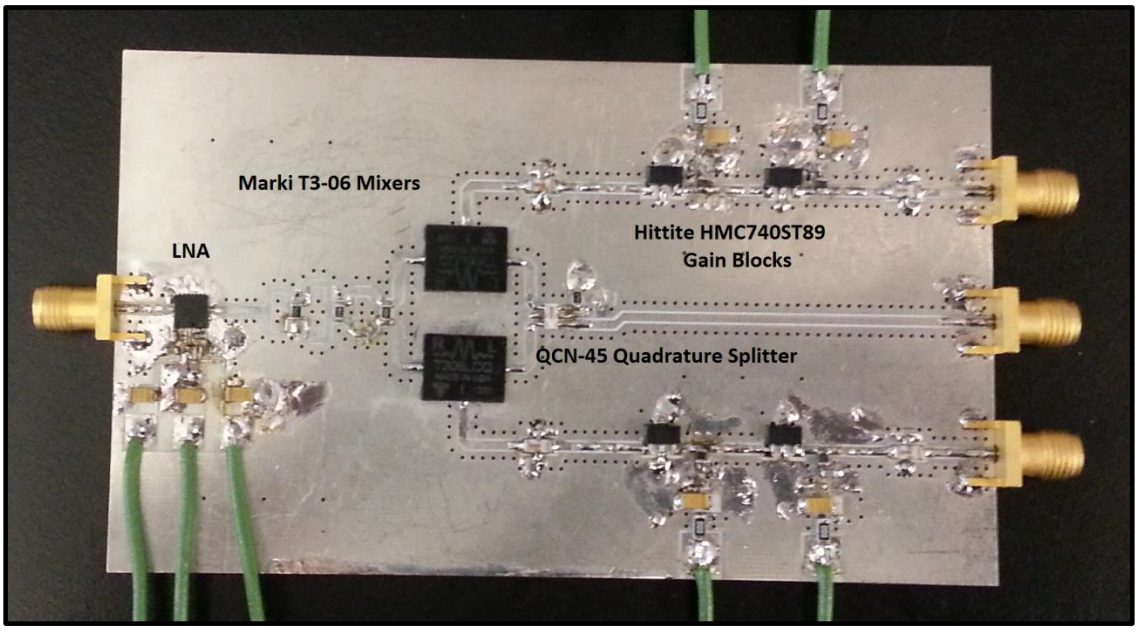

Figure 56 – Receiver PCB

Figure 57 – Hittite HMC740 S11 and S22

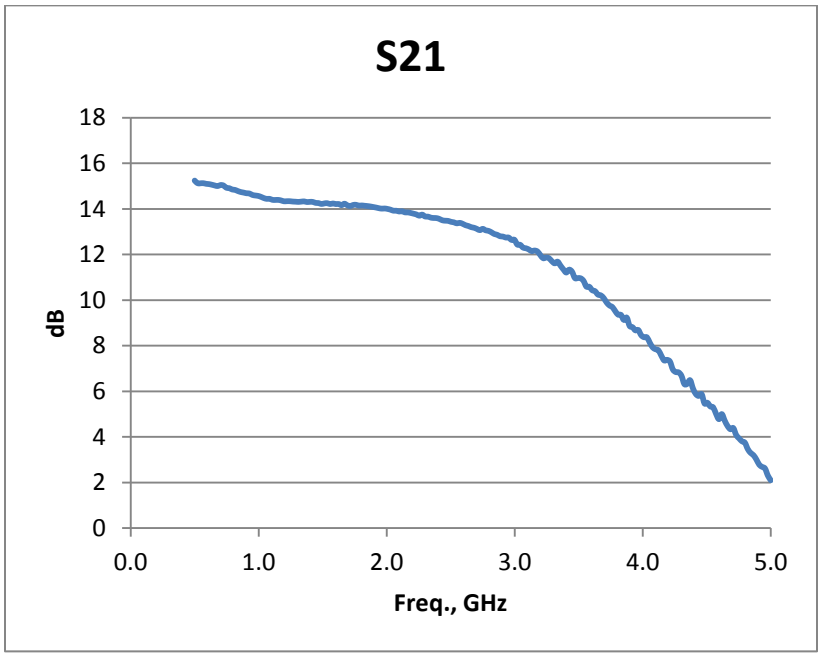

Figure 58 – HMC740 gain

Output Low Pass Filters

The two Mini-Circuits LFCN-1800+ low pass filters, one after the mixer and the other at the receiver "I" and "Q" outputs, reduced receiver input noise, carrier leakage and harmonics above 1.8 GHz.

Receiver Results

The pulse generated at the transmitter board was up-converted, amplified, and then input to the receiver board after 40 dB of attenuation. There, it was successfully down-converted and amplified, with the resulting output pulses compared to the original prototype, as depicted in Figures 60 through 63. Figure 61 shows the new module has better pulse-peak amplitude than the prototype, with its pulse amplitudes viewed in Figure 60. Figure 63 demonstrates an improved pulse width of 430 ps compared to the prototype pulse width of 500 ps, Figure 62.

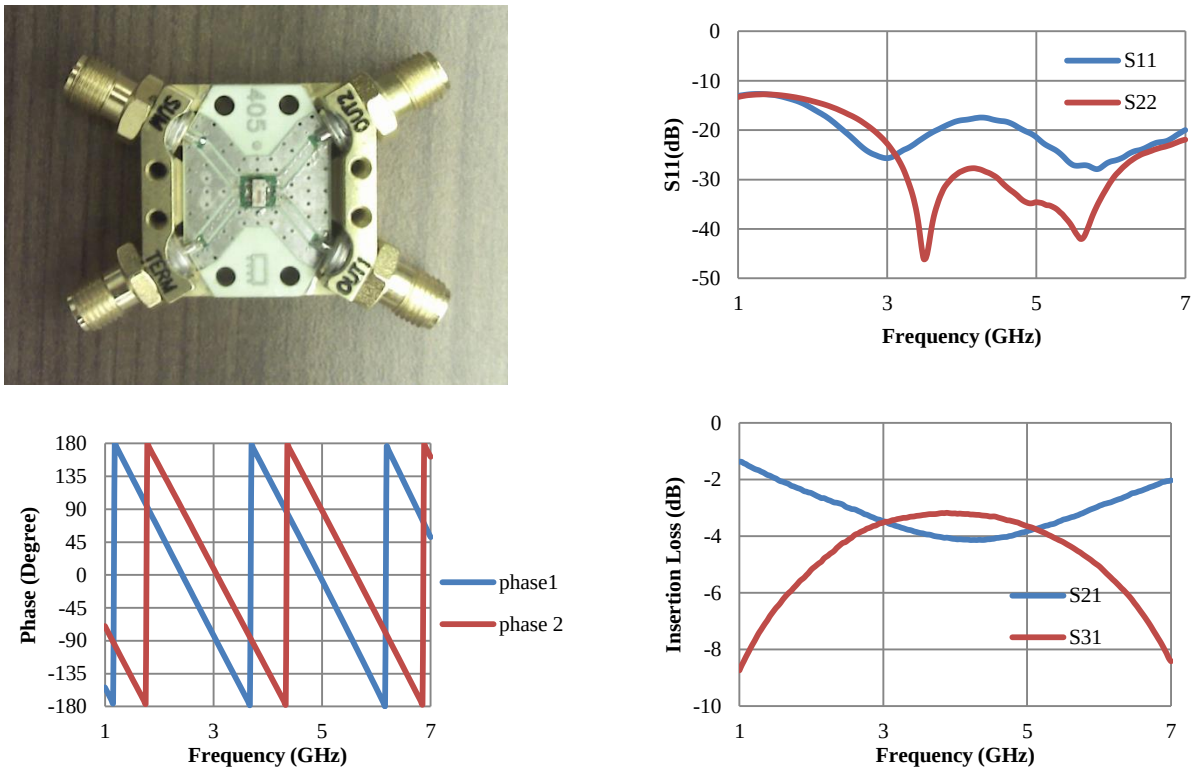

Figure 59 – Mini-Circuits quadrature power splitter measurements

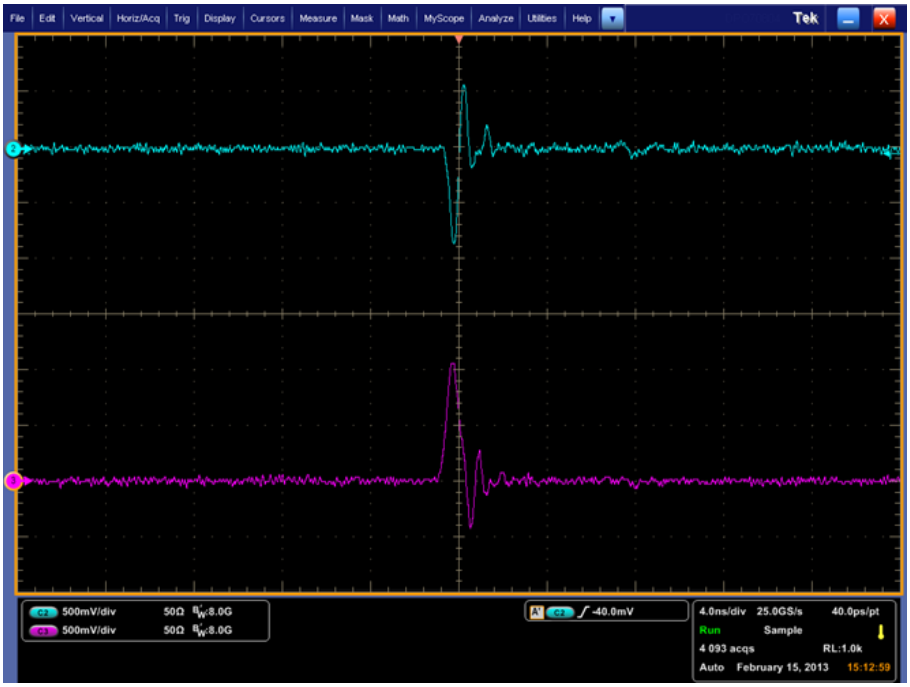

Figure 60 – Prototype receiver "I" and "Q" outputs

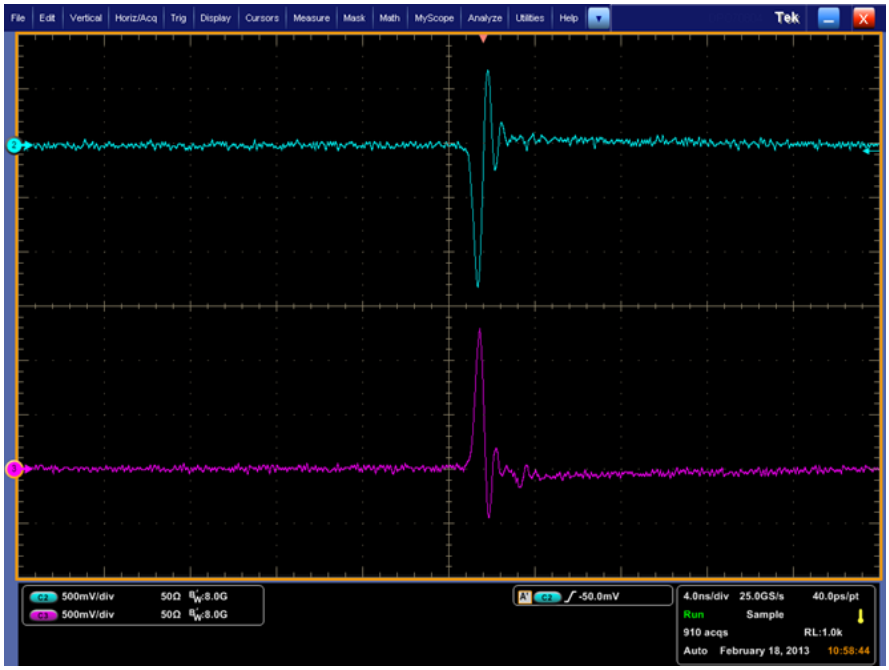

Figure 61 – New module receiver "I" and "Q" outputs

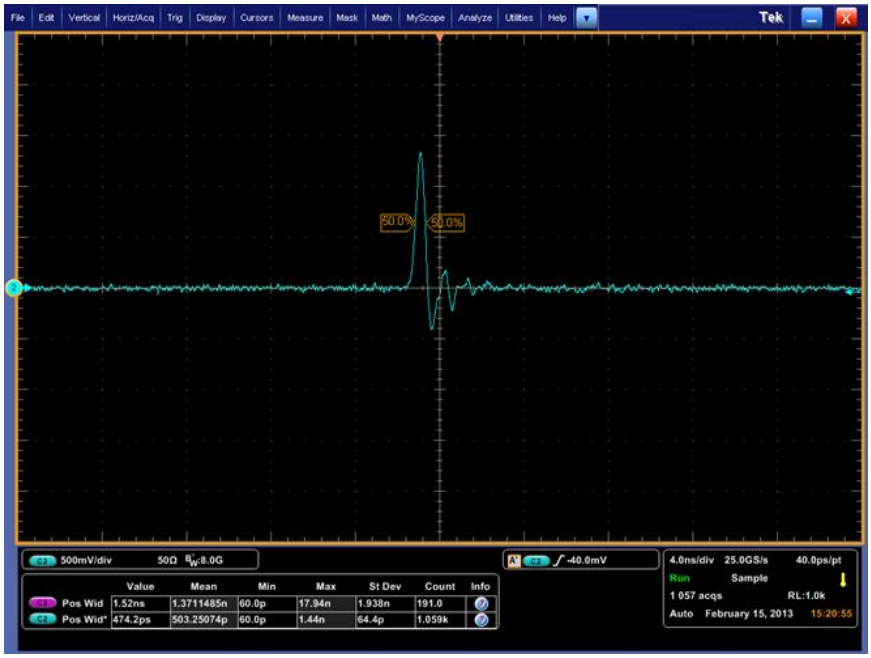

Figure 62 – Prototype output pulse of 500 ps

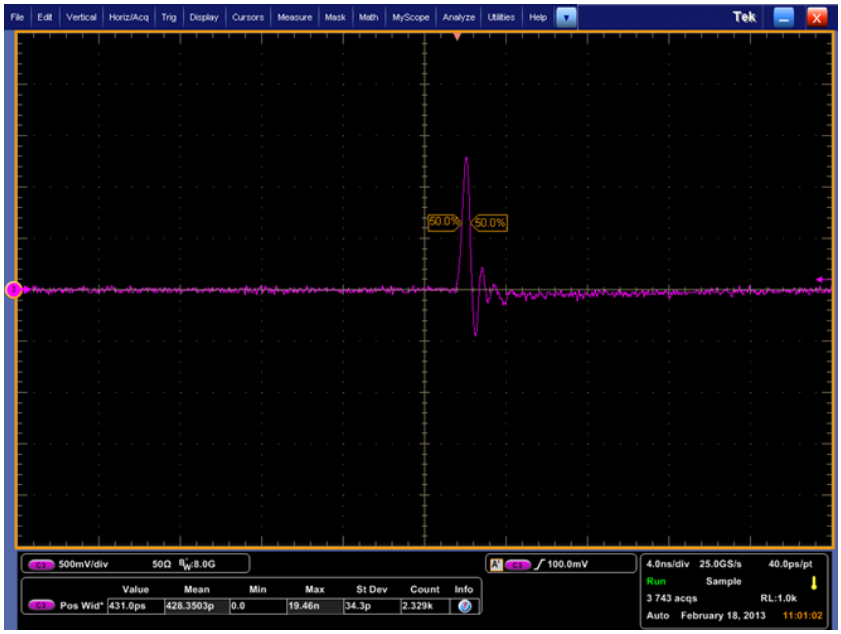

Figure 63 – Output pulse new module showing 430 ps pulse width

Power Supply

The STW PCB's required power supply improvements from the original prototype, especially for the new Power Amplifier and Pulse Generator added to the Transmitter PCB. However, with these changes came an opportunity to optimize the power supply. The result was a significant reduction in board size and part count.

The original power supply is displayed in Figure 64.

Figure 65 shows the new printed circuit board with installed components. Three simple regulators are evident: a -5V regulator at the upper left and two +5V regulators in the approximate left and right middle of the board. Five separate ten-turn trimmers, as shown, provide various positive and negative gate voltages for the VCO and Power Amplifier on the transmitter PCB and for the LNA on the receiver PCB. On the left are two barrel connectors, necessary for two plug-in DC power supplies, as shown in Figure 66.

The original supply had numerous bulky and unnecessary filter capacitors. Heat sinks and ground planes were reduced in the new supply, and handy 0.1" connectors were added to aid in simplifying connections to the main boards as well as for any future board upgrades.

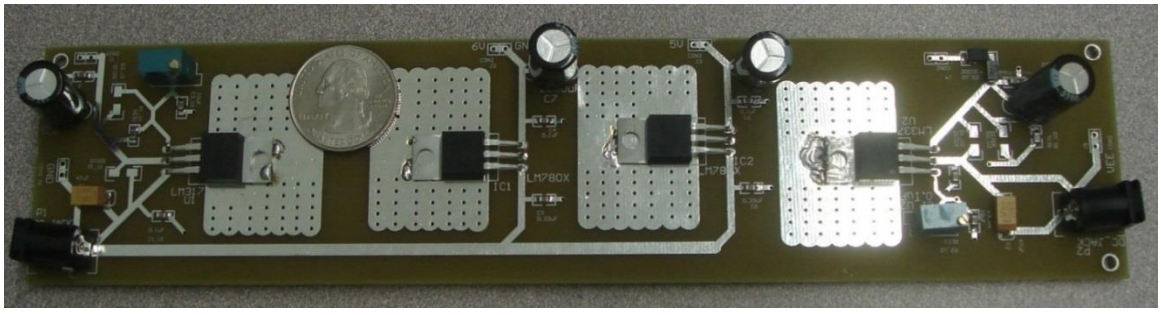

Figure 64 – Original power supply for the prototype with dimensions of 2" x 8"

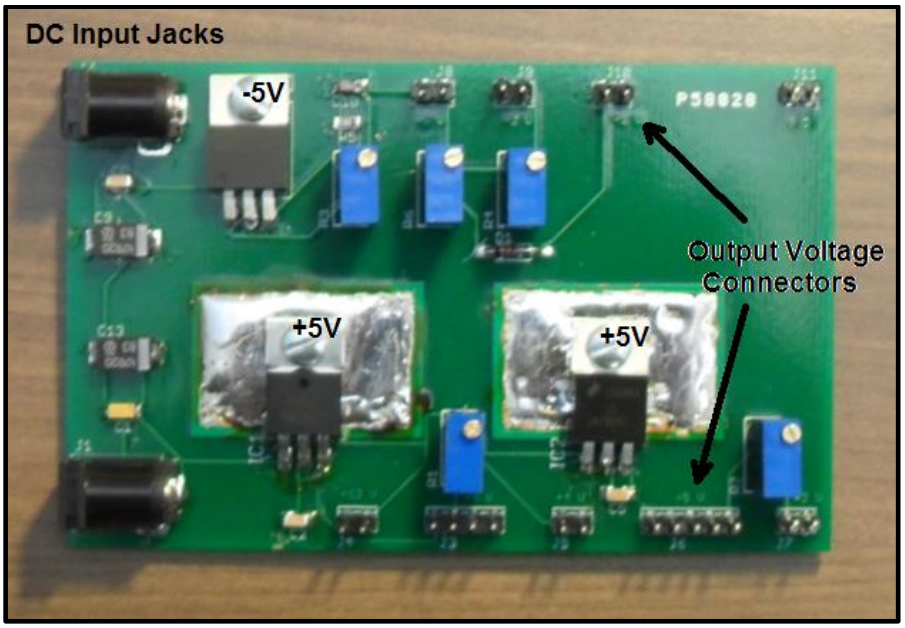

Figure 65 – STW Power Supply. Final dimensions are 2.5” x 3.5”

Figure 66 – DC power packs for the STW module

Final board size was 2.5” x 3.5”, easily one-half the size of the original prototype power supply, and well within module specifications.

Stack-up

Figure 67 shows the three main boards in a module assembly. The Transmitter, Receiver and Power Supply PCB’s were separated by blank single-sided FR4 PCB’s. These grounded, copper clad boards provided isolation between the individual power supply, transmitter and receiver boards, a “quieter” environment for clean operation, and a structure to add additional needed components.

The Receiver is at the top of the module. The left SMA would be connected to the receiving antenna. The right upper and lower SMA’s are the “I” and “Q” outputs that are connected to the Digital Acquisition Board. The right middle connector is the input terminal for the demodulating carrier, which was generated at the Transmitter PCB. A coaxial cable must connect the two boards at these ports.

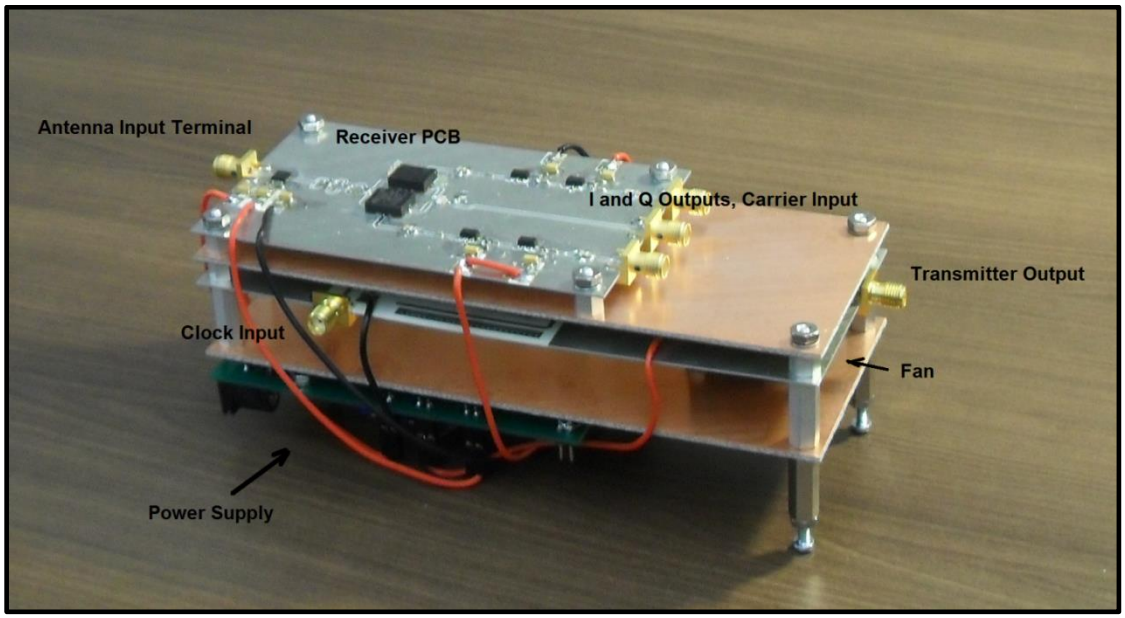

Figure 67 – STW Module Assembly

The Transmitter board, the middle board of the assembly, generates the modulated pulse for UWB wall characterization and localization. As shown, the lower connector of that board receives the clock pulse to generate this pulse. The right SMA connector goes to the transmitting antenna input terminal. Not shown in the picture, another SMA on the other side of the transmitter board provides the demodulating carrier for the Receiver.

Mounted just below the Transmitter board on the lower blank PCB is a 1" fan. The Transmitter output Power Amplifier is capable of +29dBm output power (1 dB compression) delivered to the antenna. Heat generated at this power raised the chip temperature, without cooling, to 56°C at an ambient temperature of T_A=25°C. Hittite Mfg. designed the chip (the HMC637LP5) to operate up to 85°C, so the design was well within manufacturer specifications. However, a cooling fan was added to provide for potentially higher ambient temperature environments. In addition, the lower operating temperature extended part life and helped maintain amplifier gain. With the fan, the Power Amplifier temperature dropped to and remained steady at 35°C.

The bottom PCB is the Power Supply. It was mounted to expose the 10-turn trimmers for gate voltage adjustment. One of the two DC power pack inputs is visible in the figure, at the bottom left.

Assembly size measured 3.5"W x 7"L x 3"D, not including input, output and interconnect cabling. The STW module consumed a measured 6.9 watts.

Chapter 3 – Module Test Results

The portable system was tested in several configurations. Figure 68 shows the system analyzing characteristics of a simple dihedral structure placed in an anechoic chamber. The module transmitter was connected to the blue horn antenna, centered in the middle of the picture, and a Vivaldi antenna array was used as the receiving antenna. The gold colored dihedral can be seen in the background. The received I and Q signals were sampled and the data was fed to the PC pictured in the right foreground. A Graphical User Interface (GUI) written in C++ analyzed and displayed the data.

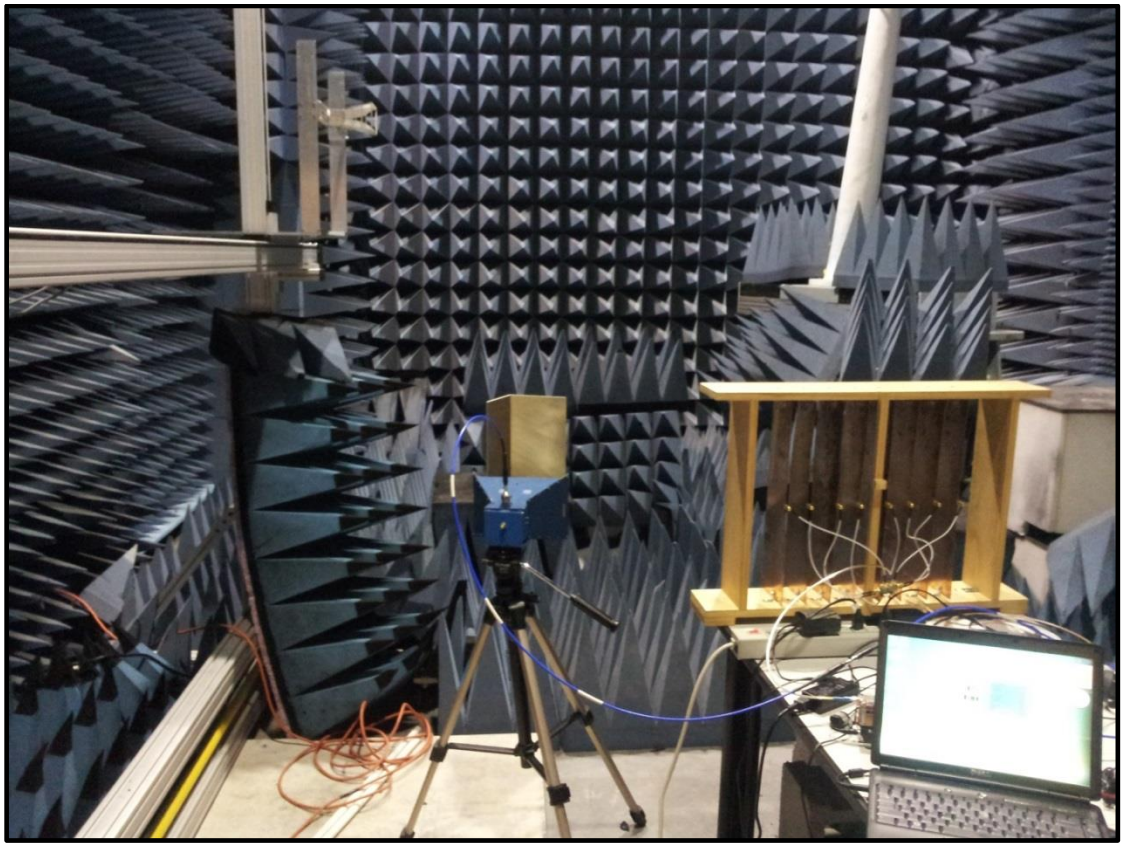

Figure 68 – Testing the portable system in an anechoic chamber

Figure 69 shows the time domain "Q" waveform of this test after sampling and filtering. The leftmost pulses, in the x-axis scale of 0 to approximately 1000 (0 to 10 ns), were caused by coupling of the transmitter and receiver antennas. The pulse data occurring at 1300 (13.00 ns) of the x-axis was reflection from the metallic dihedral. The overall sensitivity of this system was excellent. Pulse response was sharp and system noise was negligible.

Next, Figure 70 shows a test of a wall made of solid concrete bricks, 5.5" thick, with the metal dihedral placed behind the wall, out of sight.

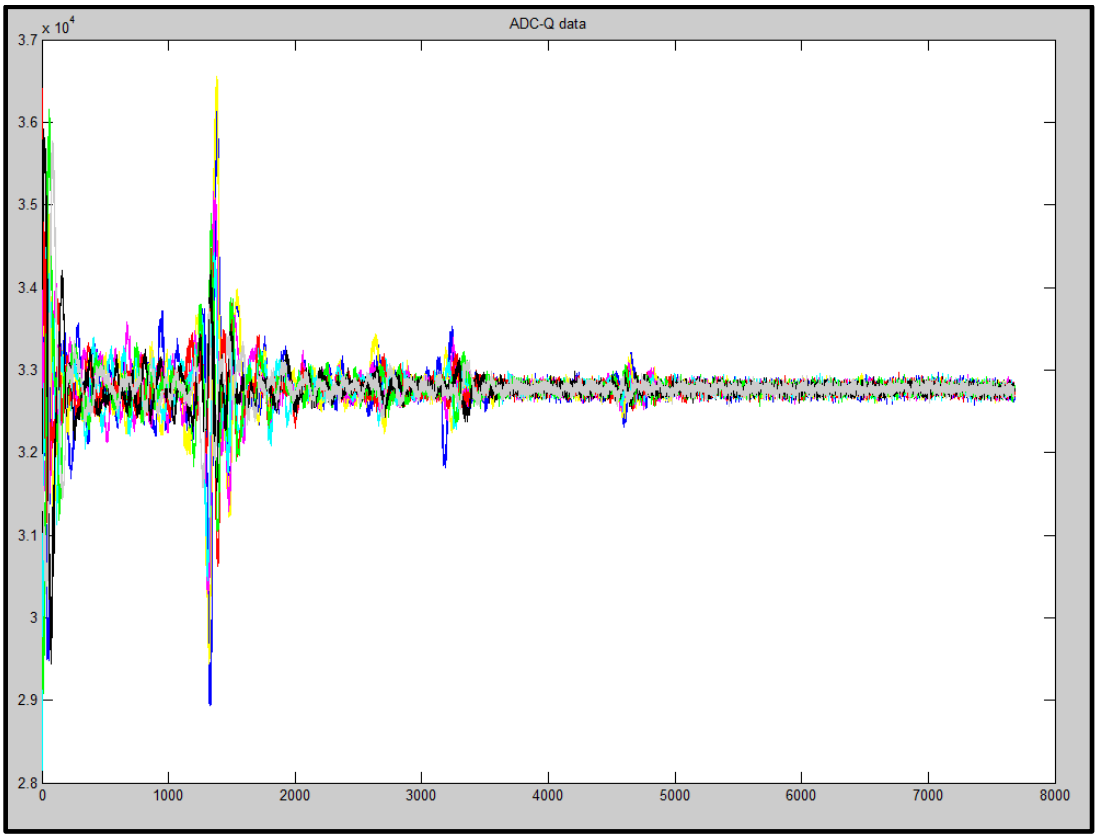

Figure 69 – Time domain reflections from a metallic dihedral object

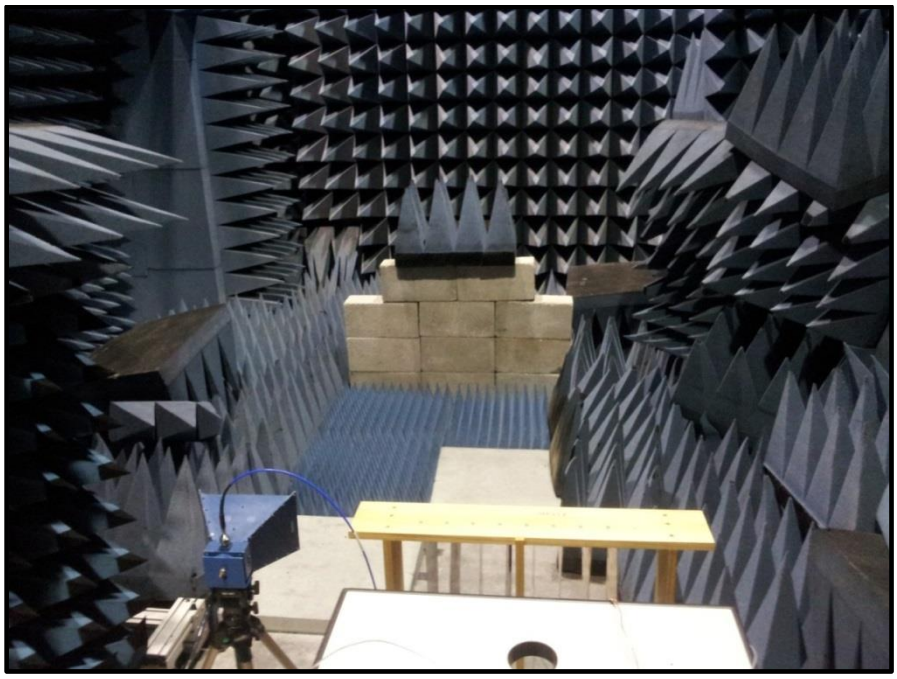

Figure 70 – A wall of concrete bricks with a metal dihedral placed behind it

Figure 71 shows the pulse response of this test. From approximately 10.00 ns to 18.00 ns on the x axis is coupling between transmitting and receiving antennas. The first major pulses are from the front of the wall, at 20.00 to 22.00 ns. At about 24.00 ns, secondary pulses are reflections from the back of the wall, and at 28.00 ns are reflections from the hidden dihedral. Again, module sensitivity proved very good.

Figure 72 compares the STW imaging of a metal target approximately three meters away from the transmitting and receiving antennas. The new module image on the right shows less “smear”, meaning better localization accuracy. Figure 73 displays the GUI image of concrete wallboard 9’ 4” away from the antenna and a metal object placed 5’ behind the wallboard. The lower image, at approximately 50 on the “y” axis, is the reflection from the wallboard. The metal target behind the wallboard is clearly seen in the image at 130 on the “y” axis.

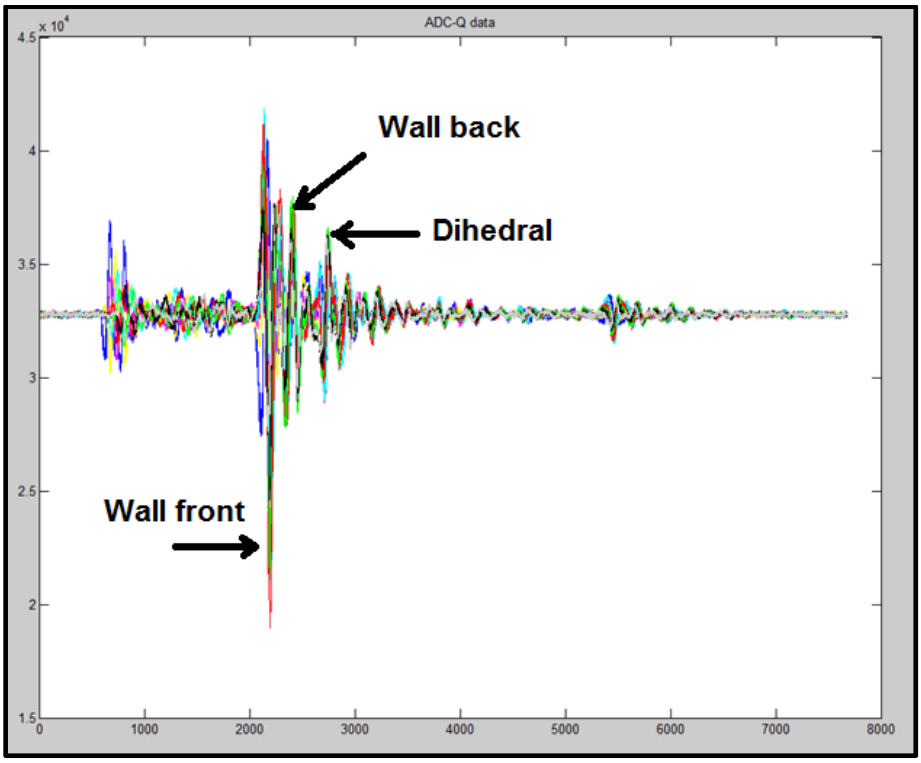

Figure 71 – Pulse response from a concrete brick wall

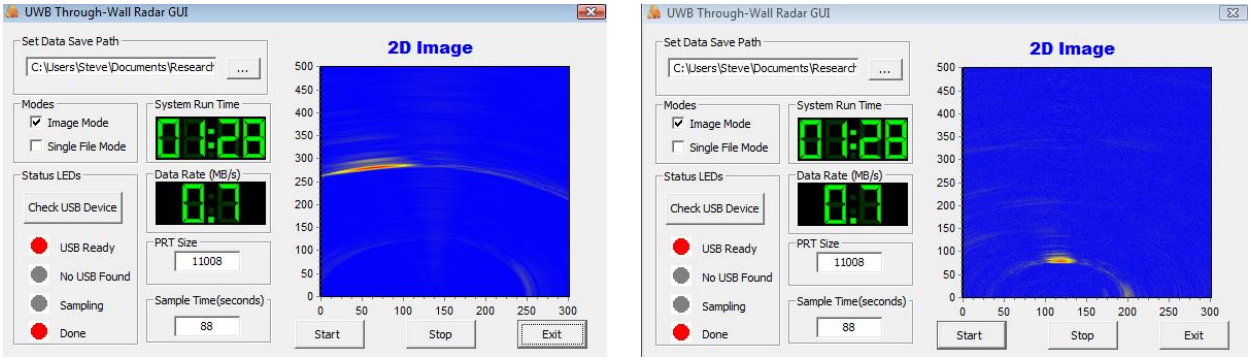

Figure 72 – Comparison of radar imaging; original prototype on the left, new module on the right

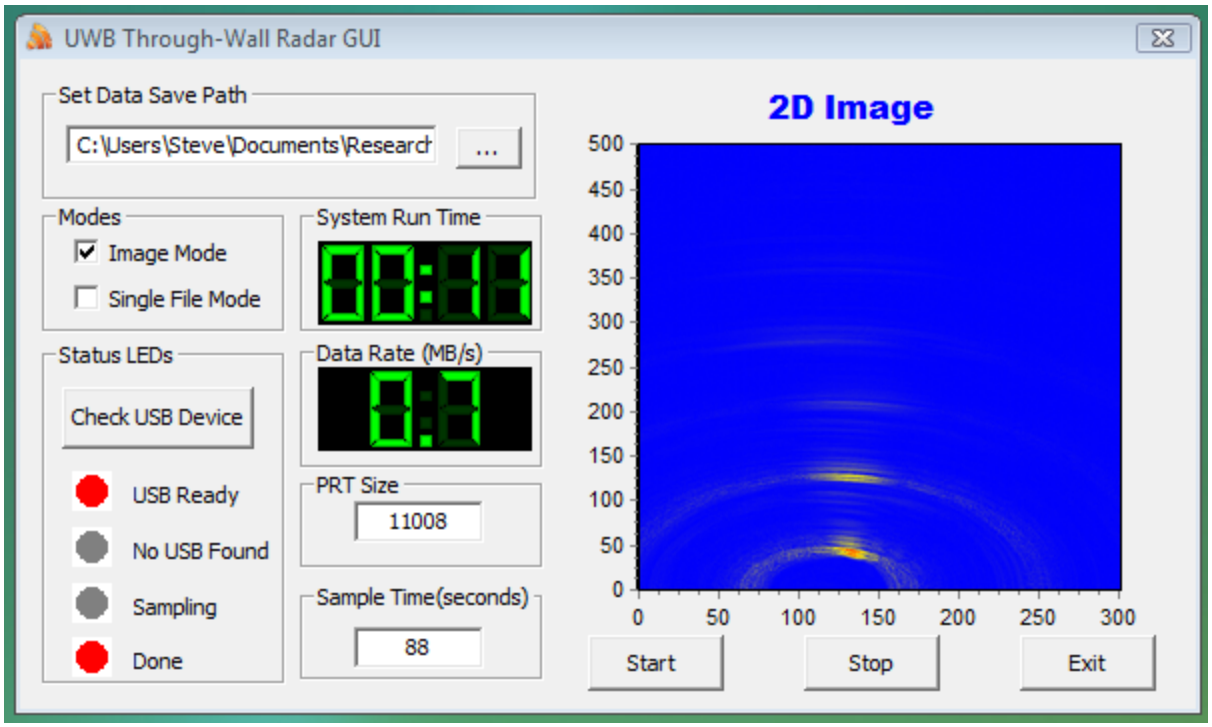

Figure 73 – GUI image showing a metal object behind concrete wallboard

Chapter 4 – Monostatic Radar Design

Discussion in this chapter centers on the details of how to reconfigure the previously designed transceiver for monostatic radar. Monostatic pulsed Doppler radar can be designed using either ultra wideband circulators or high isolation switches. Usually ultra wideband circulators are required in a CW operation, but switches are adequate for pulsed operation. In this application, the operating bandwidth of the radar system exceeds 5 GHz, necessitating a circulator with significant loss (> 1 dB). Switches are more appropriate because of their relatively low loss and the low power nature of this system.

Radar Types

By definition, Bistatic radar comprises a transmitter and receiver separated by a distance that is comparable to the expected target distance. Conversely, a radar system in which the transmitter and receiver are collocated is called Monostatic radar. Additionally, some radar systems may have separate transmit and receive antennas, but if the angle subtended between transmitter, target and receiver (the bistatic angle) is close to zero, then they would still be regarded as monostatic or pseudo-monostatic. Other types of radar include forward scatter radar, multi-static radar, and passive radar. In this implementation for wall characterization, monostatic radar is preferred to minimize localization error and because much simpler normal incidence calculations can be used.

Figure 74 shows testing conducted using a bistatic radar system. The blue “Horn” antenna on the left was used for transmitting, and the array of Vivaldi antennas, enclosed in a wood frame on the right, was used for the receiver. In Figure 75 are sketches of bistatic and monostatic radar and Table 6 compares the advantages and disadvantages of bistatic radar systems.

Figure 74 – Testing using a bistatic radar system

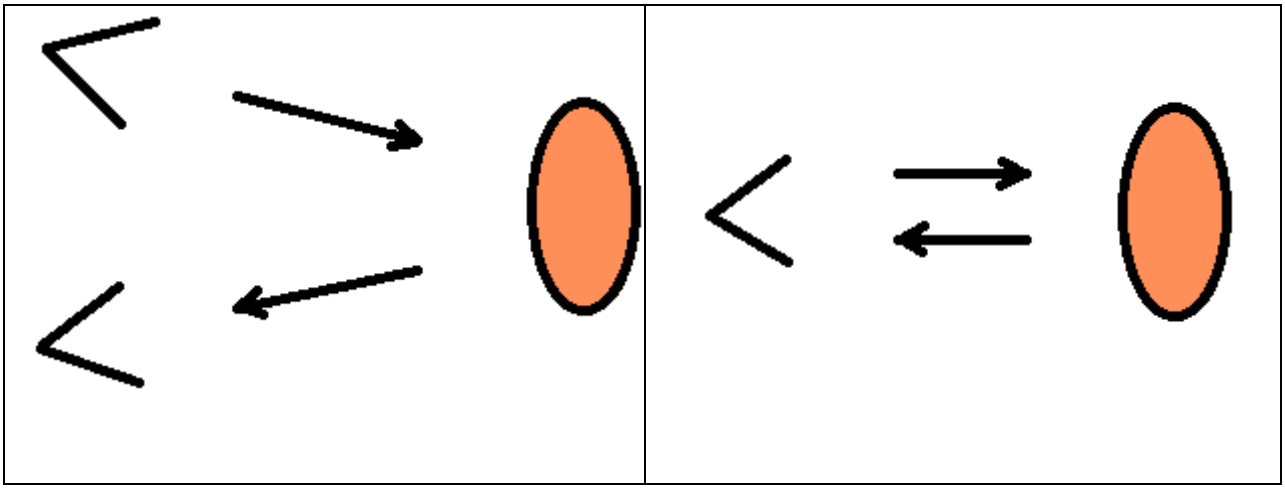

Figure 75 – Bistatic versus monostatic radar

Table 6 – Bistatic radar advantages and disadvantages

Advantages	Disadvantages
Low maintenance cost if using someone else's transmitter	System complexity
Operation without frequency clearance if using someone's transmitter	Costs of providing communication between the two sites
Great for covert operation of the receiver including resilience to counter measurements	Lack of control of the transmitter
Enhanced radar cross section	Harder to deploy
Use of separate transmitter and receiver makes the receiver much lighter	Reduced low level coverage

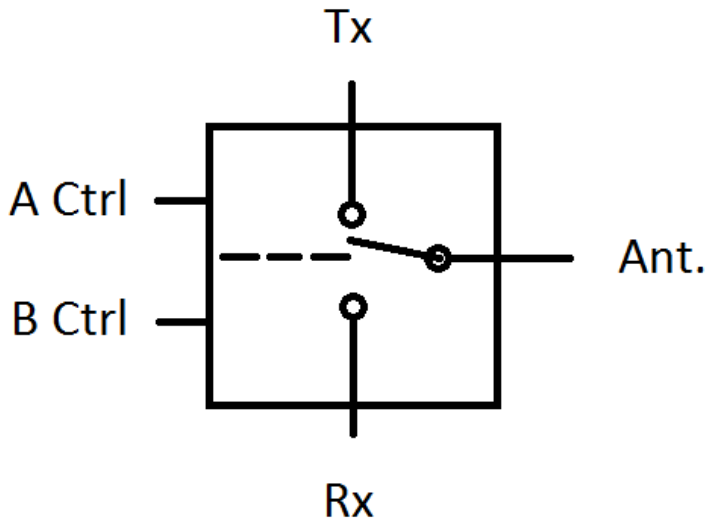

Figure 76 – Functional block diagram of the Monostatic board at the RF switch

Monostatic Adapter

The initial work for this project focused on developing a bistatic radar system. In this case, a horn was used for the transmitting antenna because of its high gain, broadband response, and small size. A Vivaldi antenna was used at the receiver because of its narrow vertical beamwidth (floor to ceiling) in addition to its broad bandwidth.

For better wall characterization, a simple monostatic modification, using the same module, was needed. Thus the transmitter and receiver would require operation using a single antenna. To protect sensitive receiver circuitry, the receiver input must be disconnected briefly from the antenna to allow transmission of the UWB pulse. Once the pulse is transmitted, the receiver would be re-connected and the transmitter disconnected. See Figure 76.

To review, Figure 77 shows a reprint of the transmitter block diagram. A clock signal from the system's digital control board is input at the transmitter's FPGA port. This clock generates a 10 MHz, 260 ps pulse that is modulated on a 3.125 GHz carrier. The resultant modulated products are amplified and then drive the transmitting antenna.

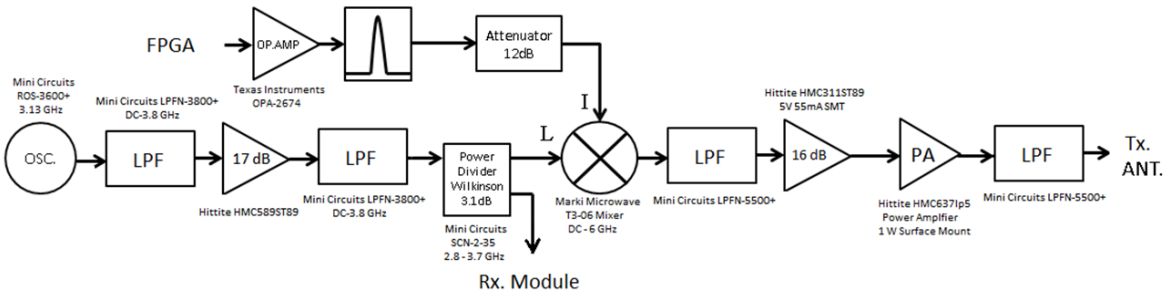

Figure 77 – Transmitter block diagram

Fig. 78 shows the clock signal (green) and the output of the transmitter (magenta). It can be seen that the radar pulse occurs at approximately 15 ns from the falling edge of the clock. Using the clock signal, an appropriately timed Transmit/Receive (T/R) switch could connect and disconnect the transmitter and receiver.

The Switch and Switch Control

To accomplish this, the board must precisely control a high speed, broadband microwave switch. During transmission of the UWB radar pulse, the switch must connect the transmitter to the antenna. Since the UWB pulse repeats every 100ns, a control pulse to the switch must be generated long enough, with the same repetition rate and timing, to gate the UWB pulse energy. Then the transmitter must be disconnected from the antenna to permit connection of the receiver.

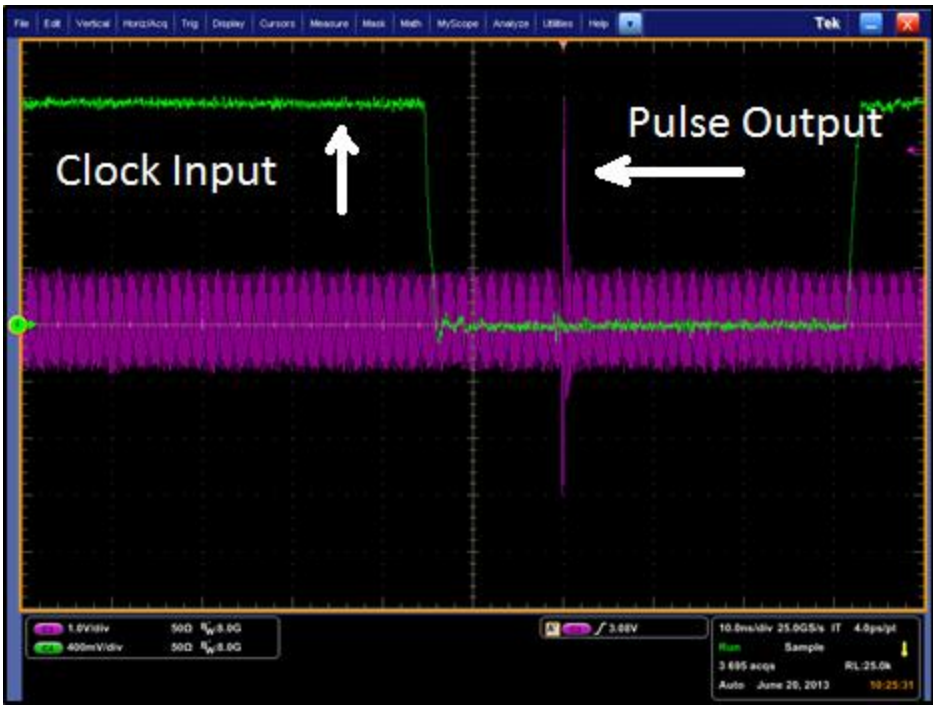

Figure 78 – Clock and transmitter signals

Crucial to this design is the switching time. Quick switch actuation will maximize the receiver connection time to the antenna, and therefore data acquisition time. However, a short interval for the transmitter connection implies a more difficult fast control pulse with a small duty cycle. Details to this discussion are in the next section.

RF Switch

For the RF switch, the Hittite HMC347lp3 and the MA/COM MASW-008322 were evaluated. Their evaluation boards, pictured in Figures 79 and 80, were ordered, received and tested.

Both switches offered good bandwidth, return loss and isolation, as Table 7 demonstrates. Switching speeds were reasonable at 6ns and 12ns respectively, quality times for a surface mount package. The MA/COM switch had significantly lower insertion loss, and its reflective topology was unimportant since the transmitter UWB pulse would not be present when the switch was open. Thus, Figure 86, page 2 of the schematic for the monostatic board, shows the MA/COM implementation.

The difficulty for this implementation arises chiefly due to the switch activation time. Since the MA/COM switch requires 12 ns to turn “on” and “off”, the receiver must be disconnected the first 12 ns, and therefore any pulse arriving during that time will be lost. This translates in free space to a travel distance of 3.6 meters in one direction, or for a reflected pulse, 1.8 meters. Thus, any wall characterization or object localization must be at least 1.8 meters distant from the transmitter.

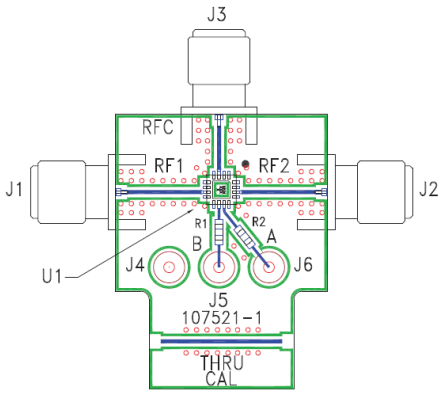

Figure 79 – Hittite HMC347 Evaluation Board

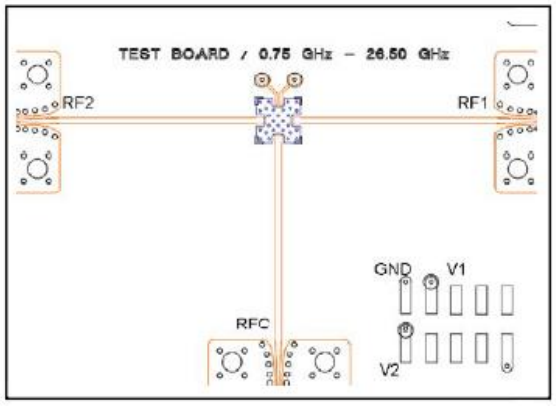

Figure 80 – MA/COM MASW-008322 Evaluation Board

Table 7 – Comparing Industry-leading RF Switches

	Hittite HMC347	MA/COM MASW-008322
Bandwidth	DC – 14 GHz	DC – 20 GHz
Non-Reflective	Yes	No
Return Loss (Typ.)	13 dB	20 dB
Insertion Loss at 6 GHz	1.6 dB	0.7 dB
Switching Speed	6 ns	12 ns
Isolation at 6 GHz	46 dB	44 dB

Control and Timing

The MA/COM switch required -5/0 V to turn on/off. The block diagram of Figure 81 displays the approach to generate this signal.

A simple chip made by Maxim Integrated, the DS1123, can provide a programmable delay of up to 128 ns in 0.5 ns steps. In addition, it can also be operated as a re-triggerable monostable multivibrator with pulse-width down to 5 ns. In either mode, programming can be simply hard-wired onto the printed circuit board. A small surface-mount chip, it operates at +3.3V, the same logic voltage as the clock generated by the FPGA. Its data sheet is shown in Fig. 82.

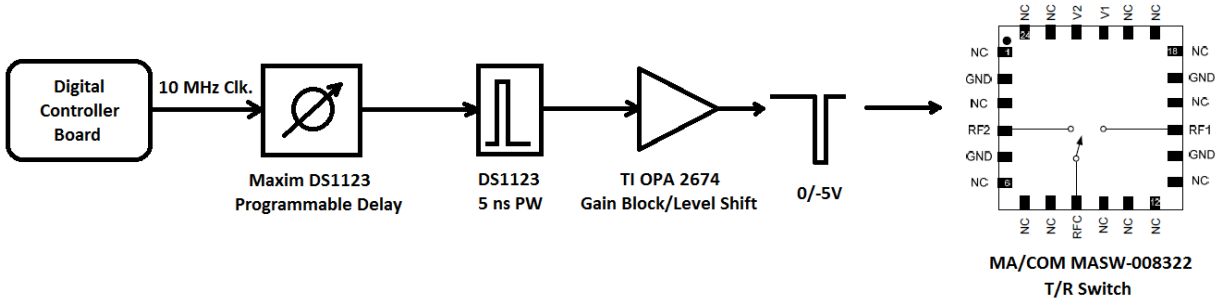

Figure 81 – Control voltage generation for the MA/COM RF switch

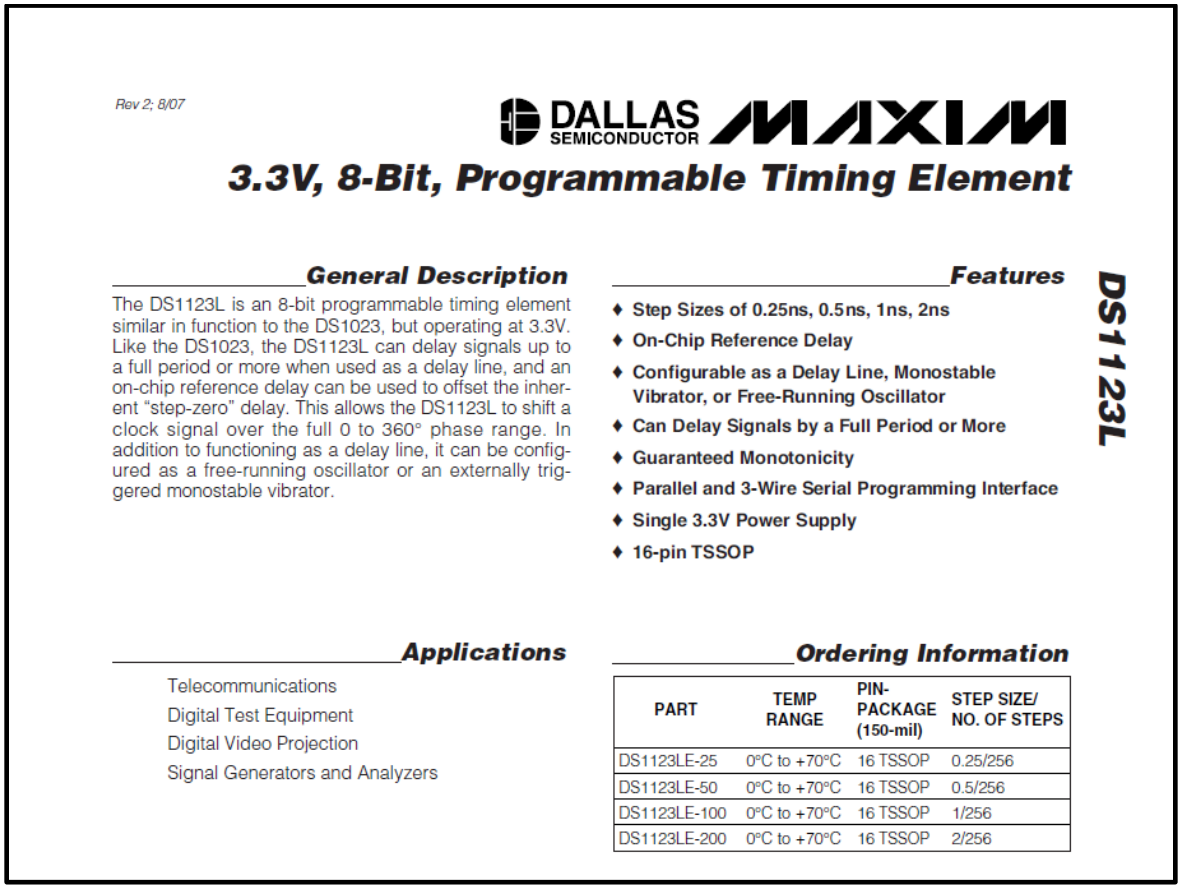

Rev 2; 8/07

DALLAS SEMICONDUCTOR MAXIM

3.3V, 8-Bit, Programmable Timing Element

DS1123L

General Description

The DS1123L is an 8-bit programmable timing element similar in function to the DS1023, but operating at 3.3V. Like the DS1023, the DS1123L can delay signals up to a full period or more when used as a delay line, and an on-chip reference delay can be used to offset the inherent "step-zero" delay. This allows the DS1123L to shift a clock signal over the full 0 to 360° phase range. In addition to functioning as a delay line, it can be configured as a free-running oscillator or an externally triggered monostable vibrator.

Features

- Step Sizes of 0.25ns, 0.5ns, 1ns, 2ns
- On-Chip Reference Delay
- Configurable as a Delay Line, Monostable Vibrator, or Free-Running Oscillator
- Can Delay Signals by a Full Period or More
- Guaranteed Monotonicity
- Parallel and 3-Wire Serial Programming Interface
- Single 3.3V Power Supply
- 16-pin TSSOP

Applications

Telecommunications
Digital Test Equipment
Digital Video Projection
Signal Generators and Analyzers

Ordering Information

PART	TEMP RANGE	PIN-PACKAGE (150-mil)	STEP SIZE/ NO. OF STEPS
DS1123LE-25	0°C to +70°C	16 TSSOP	0.25/256
DS1123LE-50	0°C to +70°C	16 TSSOP	0.5/256
DS1123LE-100	0°C to +70°C	16 TSSOP	1/256
DS1123LE-200	0°C to +70°C	16 TSSOP	2/256

Figure 82 – The Maxim DS1123L, a programmable timing chip and pulse generator

Once the 3.3V clock signal is sufficiently delayed and converted to a 12 ns pulse of correct polarity, it must be amplified and level shifted. To do this, the familiar and readily available TI OPA 2674 op amp was implemented. The amplifier features a 2 ns risetime and a 220 MHz bandwidth. Because of its current feedback design, gains from 1 to 8 V/V were possible without compromising its bandwidth. Finally, TI offers the op amp in the useful dual configuration with an SOIC-8 pin package. This results in a small form factor and ultimately smaller board fabrication, saving space and cost.

Figure 83 shows the LTSpice schematic for the op amp and Figure 84, simulation results. Logic gates A1 and A2 on the left side of the schematic more accurately simulated the input clock signal.

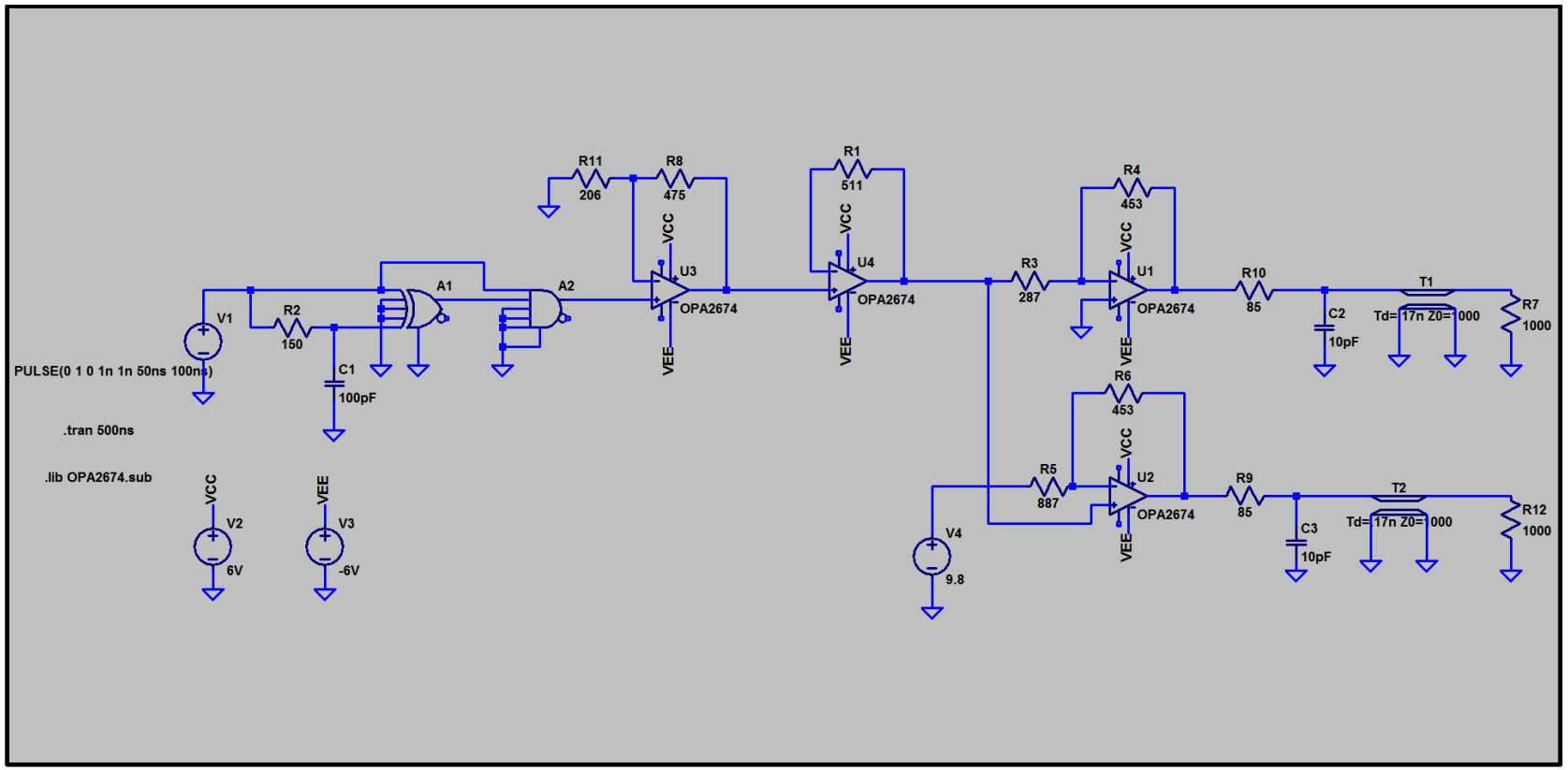

Figure 83 – LTSpice simulation of the op amp gain block

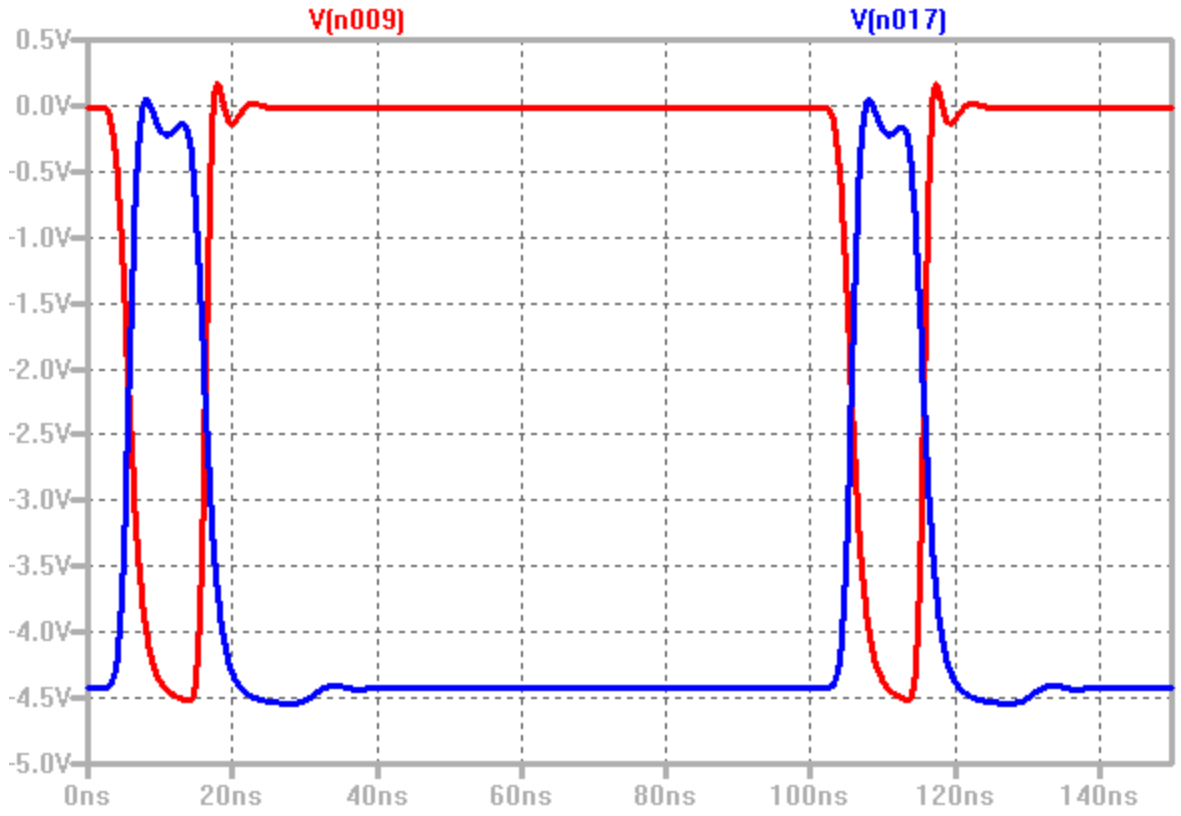

Figure 84 – Simulation results for the op amp gain block

Figure 84 shows the two complementary logic signals necessary to control the RF switch. The signal in red, labeled V(n009), drives the side of the MA/COM switch that gates the transmitter pulse. The blue signal, V(n017), opens the RF switch to make the antenna-to-receiver connection. The 4.5 V voltage swing of both signals approaches the maximum the op amp could generate with the ±6V supply. Tests of the MA/COM RF switch showed this swing would be adequate for full "on" and "off" control.

Printed circuit board schematics from Mentor Graphics PADS are pictured in Figure 85 and 86. The two DS1123L's are featured in Figure 85 with hard-wired delay control, and the TI op amps and RF Switch are shown in Figure 86. Several regulators were added to meet power supply requirements.

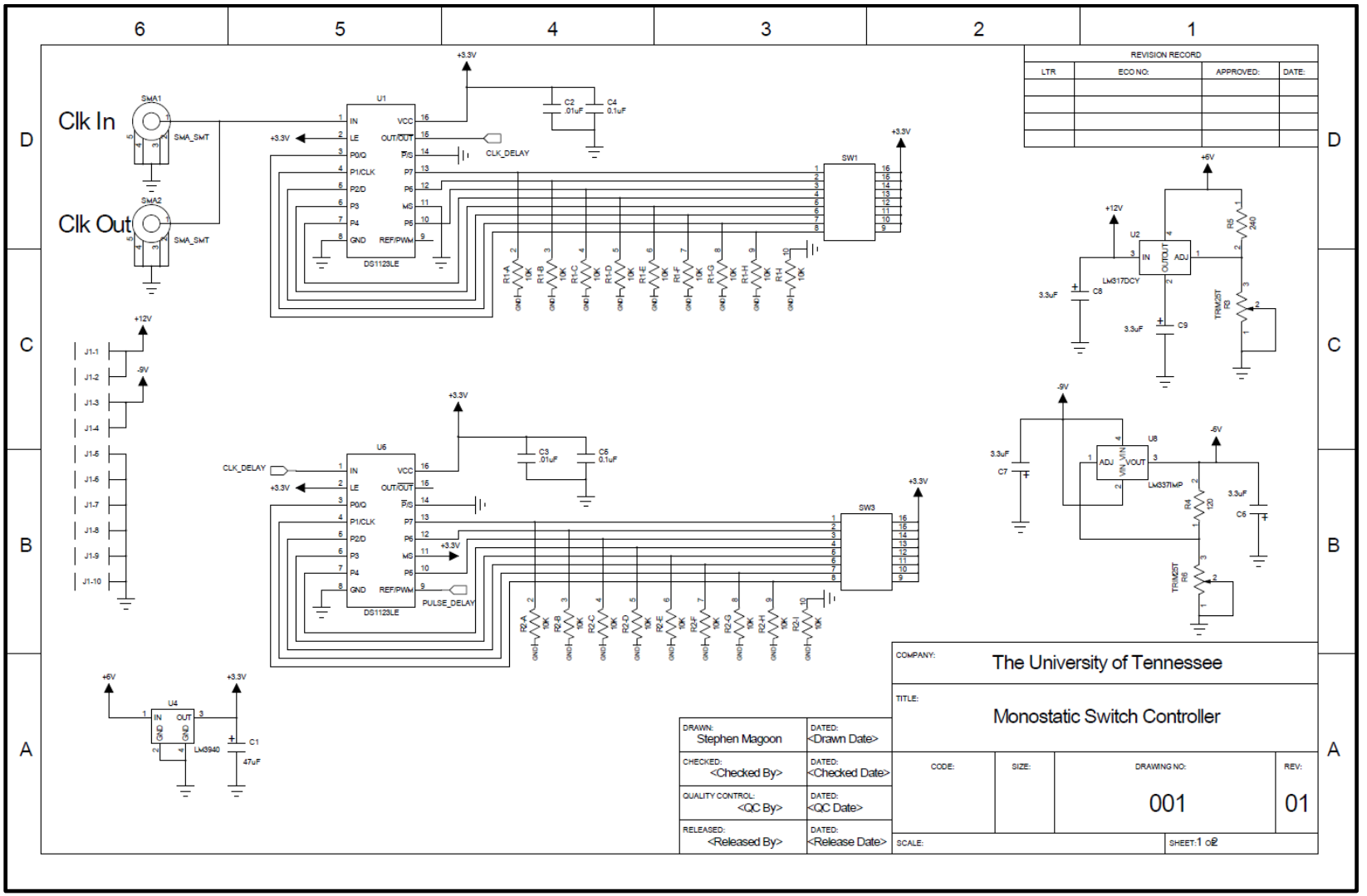

Figure 85 – Monostatic board schematic, page 1

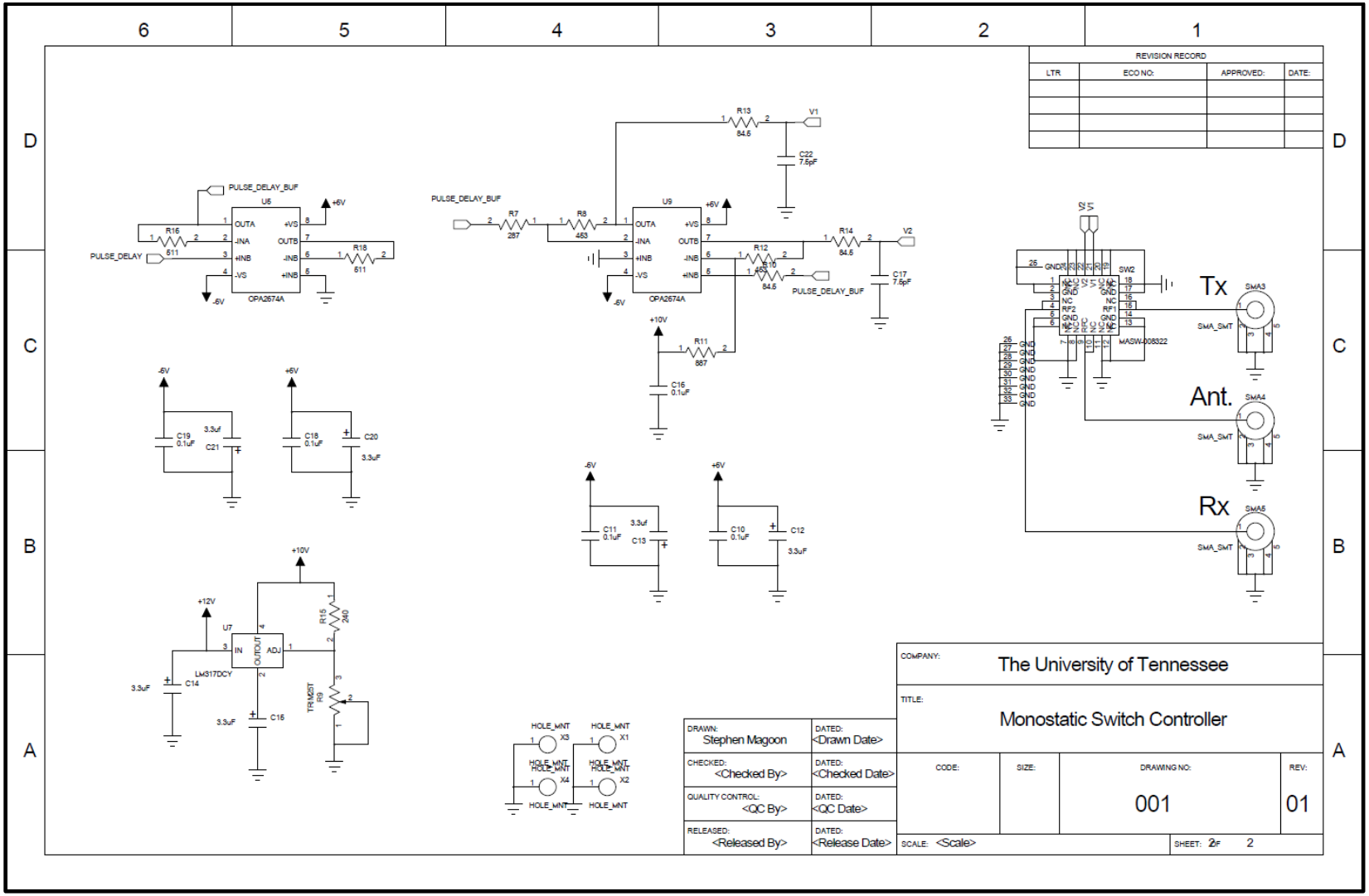

Figure 86 – Monostatic board schematic, page 2

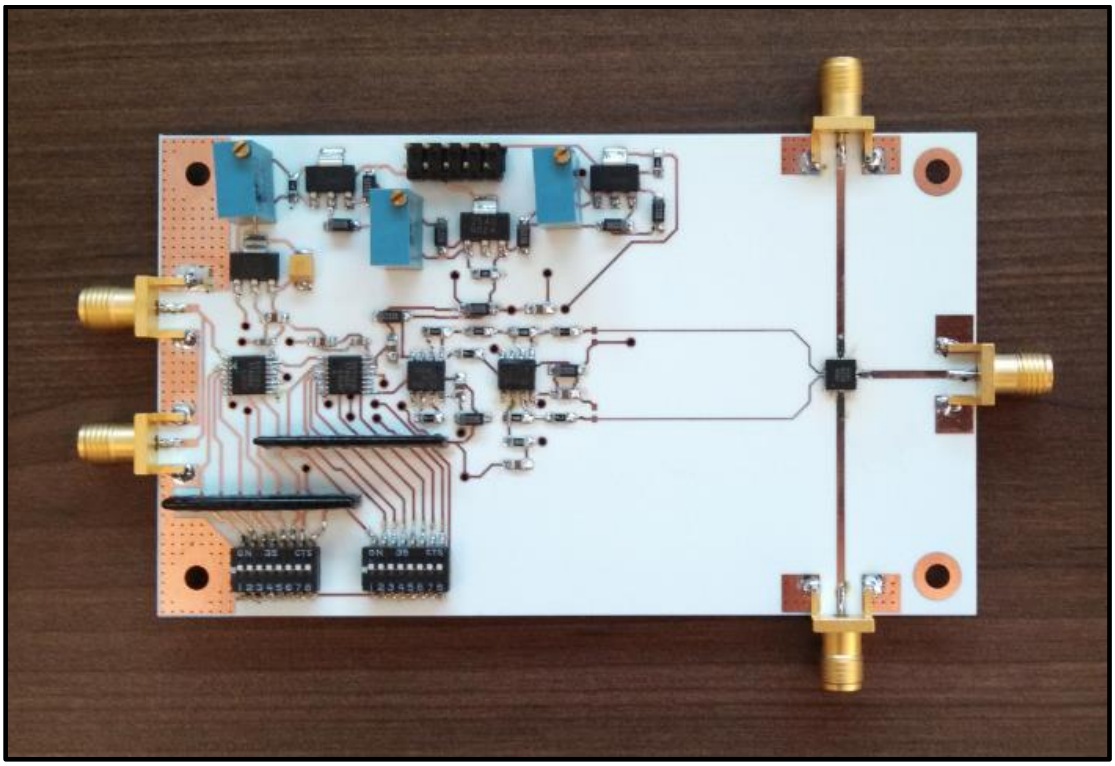

Figure 87 – The fabricated and assembled monostatic adapter board

For the monostatic board of Figure 87, the two SMA terminals on the left provide a continuity path for the clock signal from the Digital Control Board to the Through-Wall module's pulse driver network. The signal is simply picked off from this path and used to drive timer networks for the MA/COM switch. The three SMA terminals on the right provide connections to the transmitter, receiver, and the single antenna.

The MA/COM switch can be seen on the right, isolated from the rest of the control circuitry. Except for the area just below the op amps, the bottom side of the board is copper ground plane, providing noise cancellation and proper field properties for good microwave line impedance. The ground plane beneath the op amps was cleared to reduce stray capacitance for sensitive op amp circuitry.

Final layout design resulted in a circuit board only 2.5” x 4.25”. Rogers RT Duroid 4350 again was used for this board for its low loss at microwave frequencies.

Test Results

Figure 88 shows the complementary signals generated to control the MA/COM RF switch. The top signal in the figure runs at 10 MHz, mostly at 0 V, “Off”. The negative going, -5 V, 12 ns pulses, turn the switch on. Thus, the transmitter is connected to the antenna briefly. The lower signal (in blue) controls the receiver connection to the antenna. It can be seen to be mostly “On”, except for a 12 ns window to protect it from the generated transmitter energy.

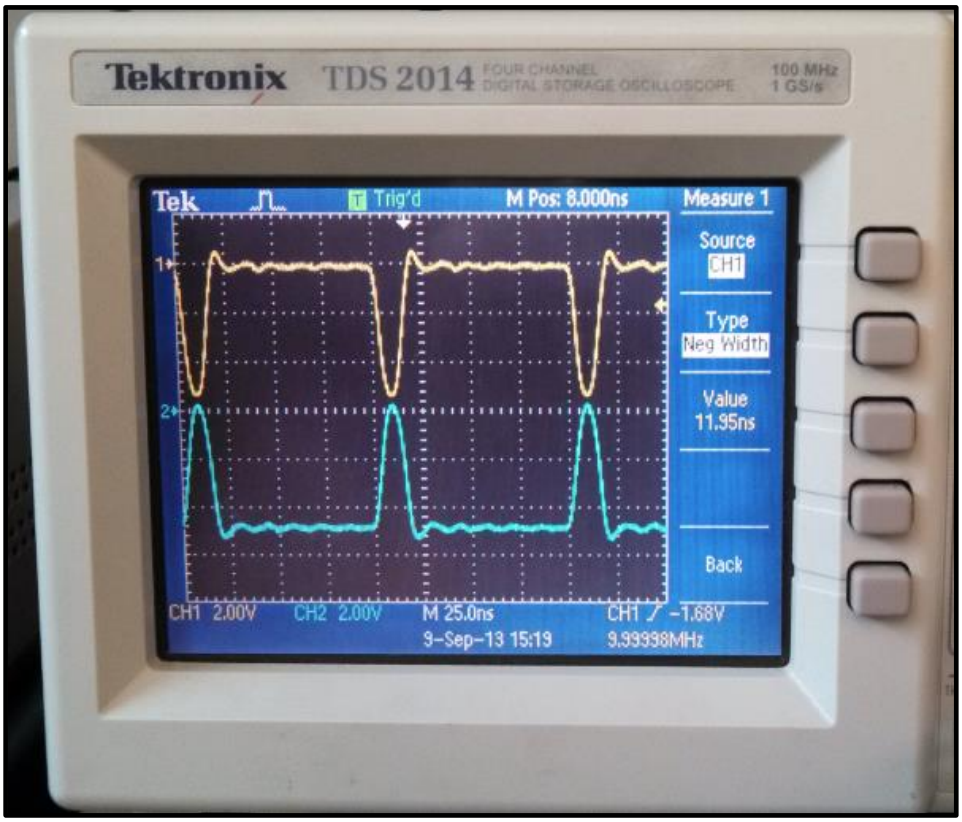

Figure 88 – Control signals generated by the monostatic board

Note in Figure 88 the essentially smooth pulse transitions. The pulses are clean and show little ringing. Kudos is due to the engineers at LT Spice for their simulation software and at Texas Instruments for their quality current feedback amplifier in the OPA 2674.

Figure 89 shows the output results of an 8ns test pulse (not the same as the UWB transmitted pulse) connected to the monostatic board RF1 input, with the timing of the monostatic board set to allow the pulse through. Figure 90 shows the result from timing the board to turn the pulse "Off". This "worst case" test clearly demonstrates the board's capabilities.

Next, Figures 91 and 92 show measured S11 and S21 for the monostatic board in the "On" position. Return loss and insertion loss show acceptable results to 5.5 GHz, the primary bandwidth of the STW system. Figure 93 and 94 show S11 and S21 in the "Off" position. Note that the board has an isolation of at least 30 dB to 10 GHz.

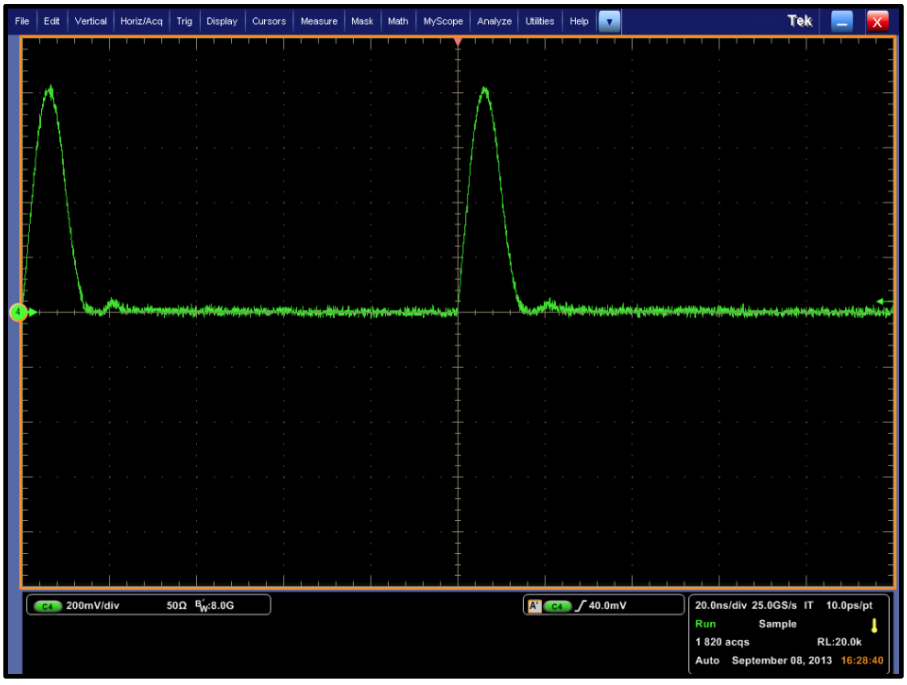

Figure 89 – Monostatic board output with timing set to allow a 10 MHz pulse through

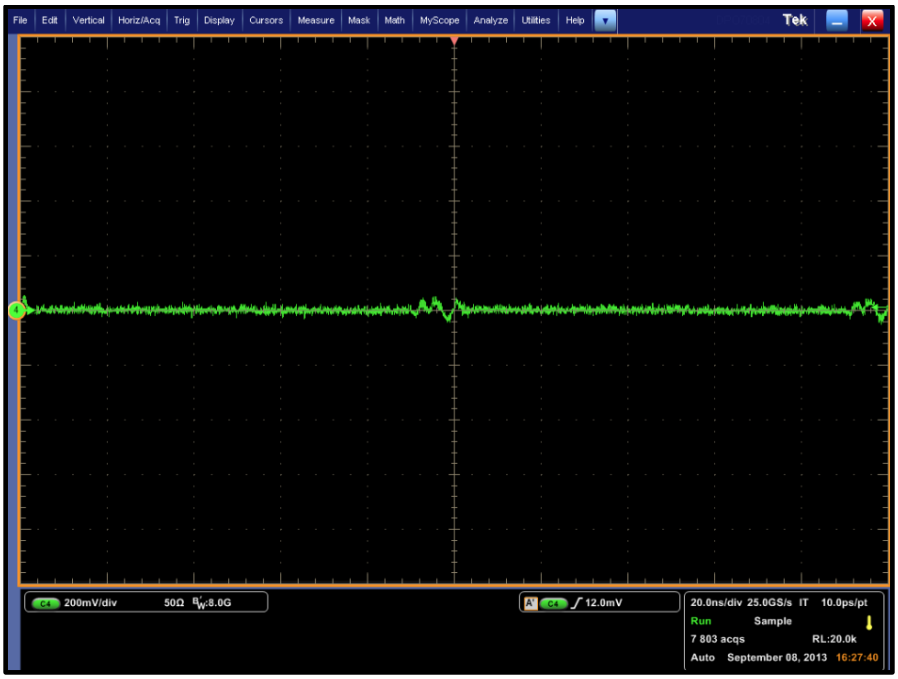

Figure 90 – Output results with an input pulse "shut-off" by the monostatic board

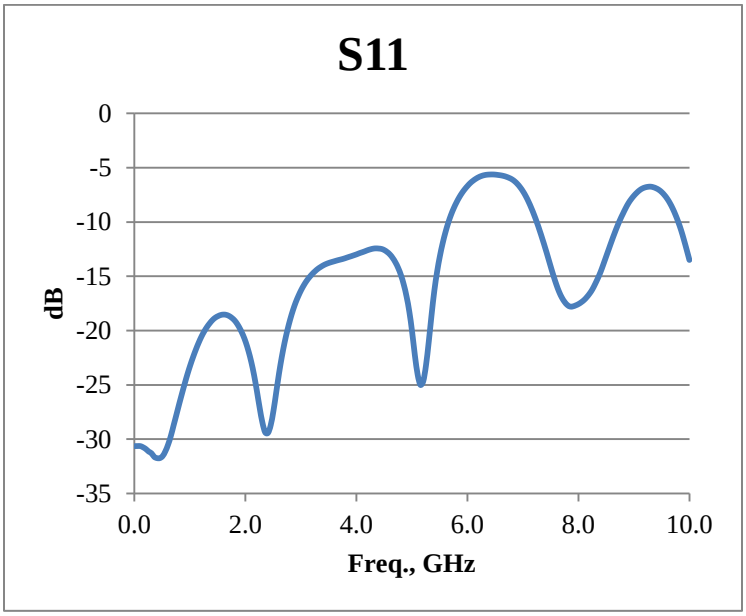

Figure 91 – Return loss for one input of the monostatic board

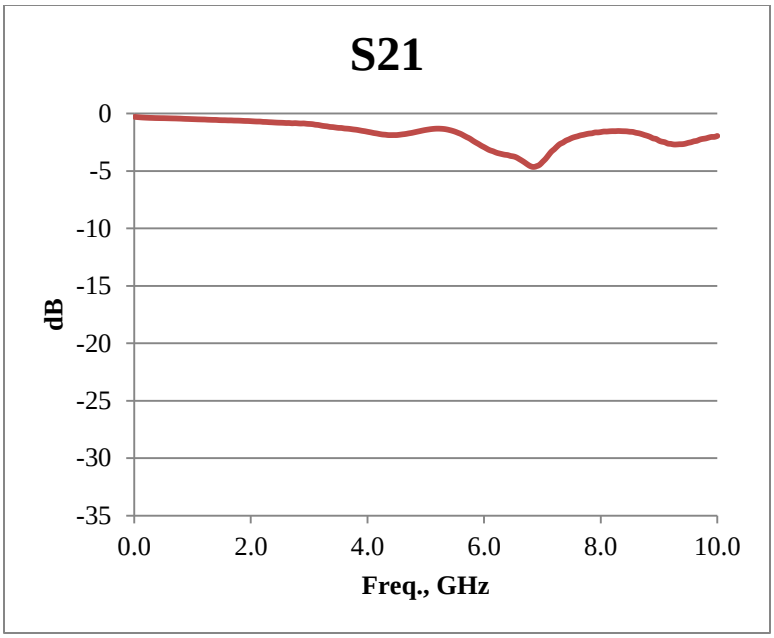

Figure 92 – Insertion loss in the "On" mode

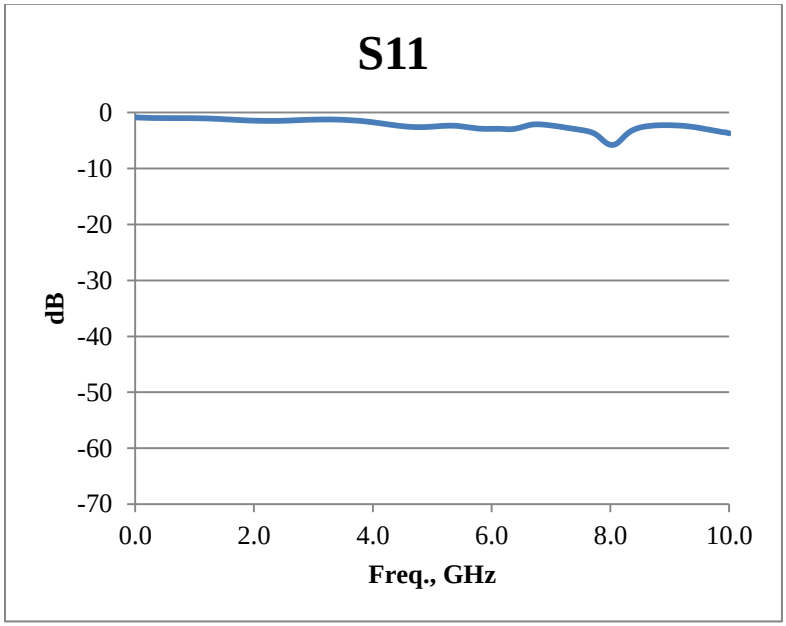

Figure 93 – Return loss in the "Off" position

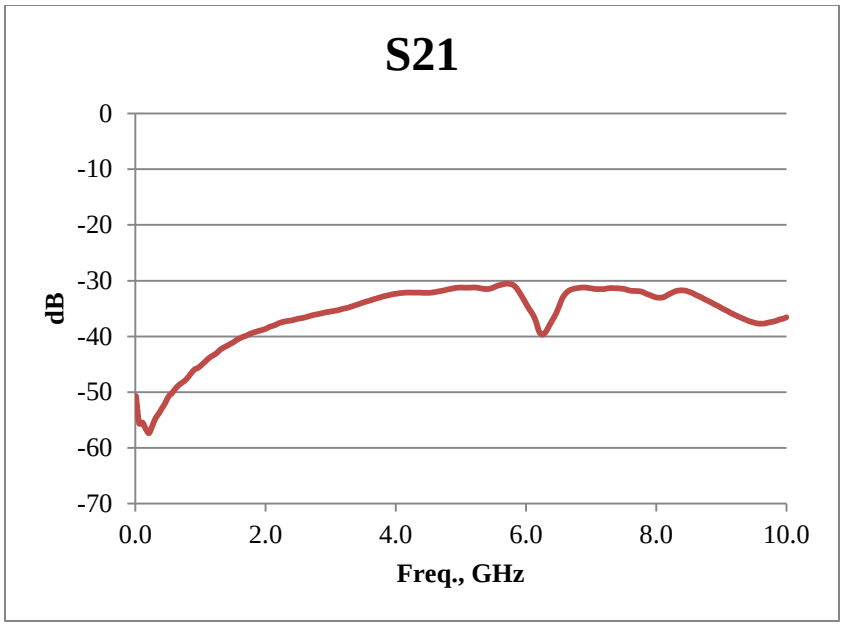

Figure 94 – Isolation in the "Off" mode

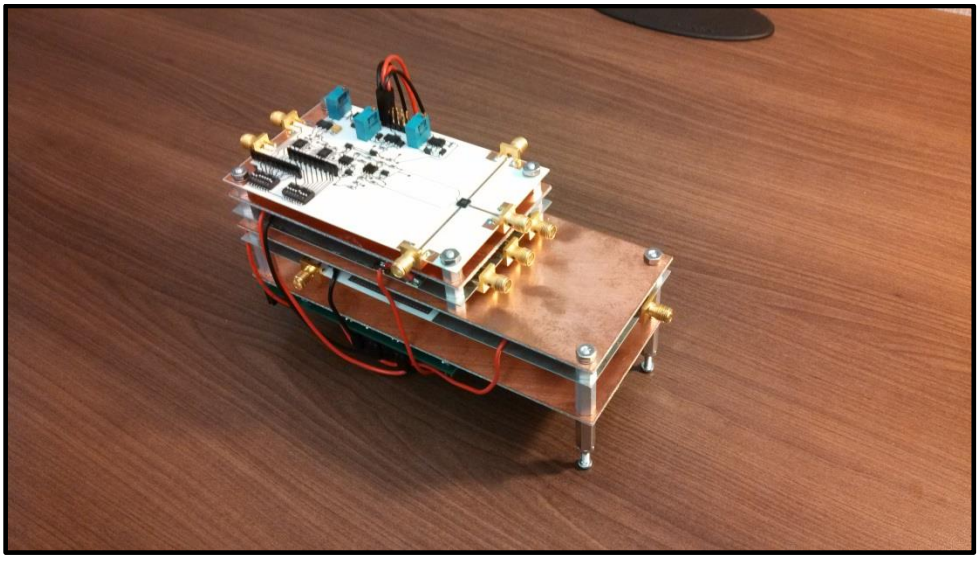

Figure 95 – Monostatic board mounted on STW module

For final confirmation of the design functionality, the board was mounted into the Through-Wall system as shown in Figure 95.

Figure 96 shows the monostatic output with the UWB transmitter pulse. Switch timing was correctly set to route the transmitter output power to the antenna. Figure 97 shows the receiver-side of the monostatic board while the transmitter was driving the antenna. The signal was strongly attenuated.

Though not shown in Figure 97, noise was detected at the receiver output during the period when the receiver was connected to the antenna. Switching noise and reflections from the transmitting antenna were amplified by the low noise, high gain and high dynamic range receiver. They will be addressed in a new board revision.

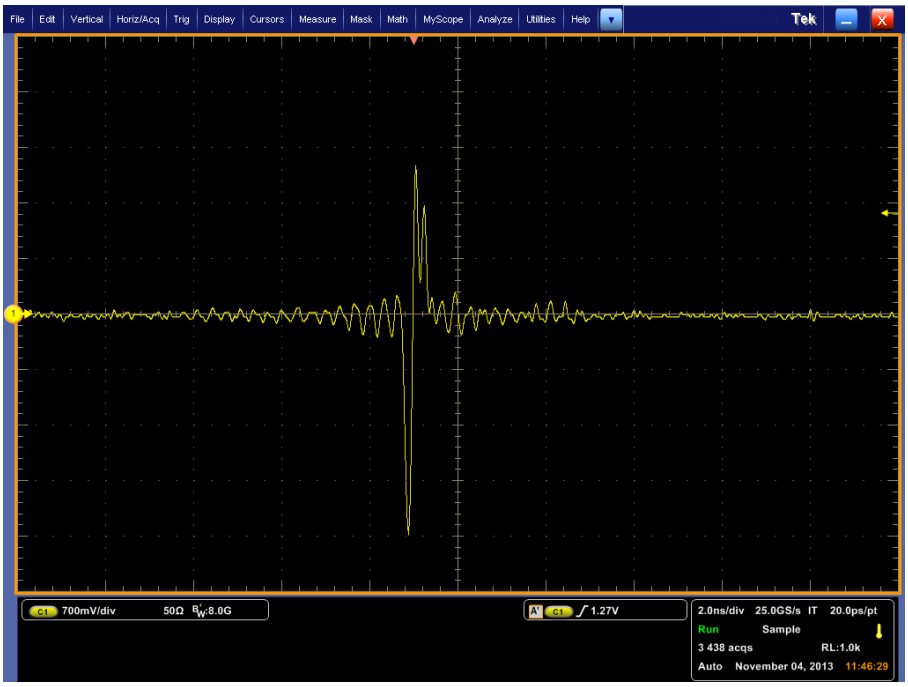

Figure 96 – Transmitter power to the antenna

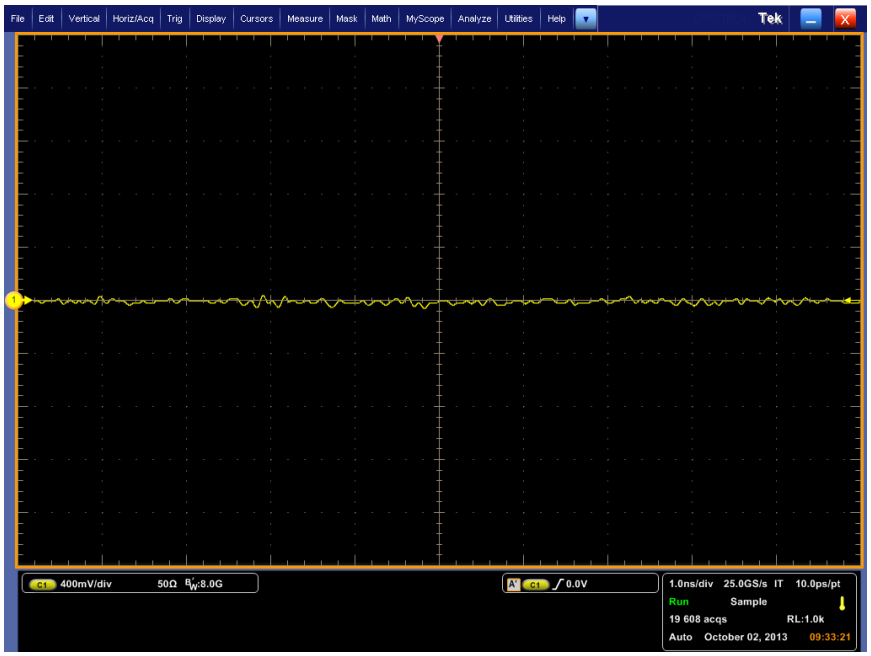

Figure 97 – Receiver output of the monostatic board with the transmitter power on

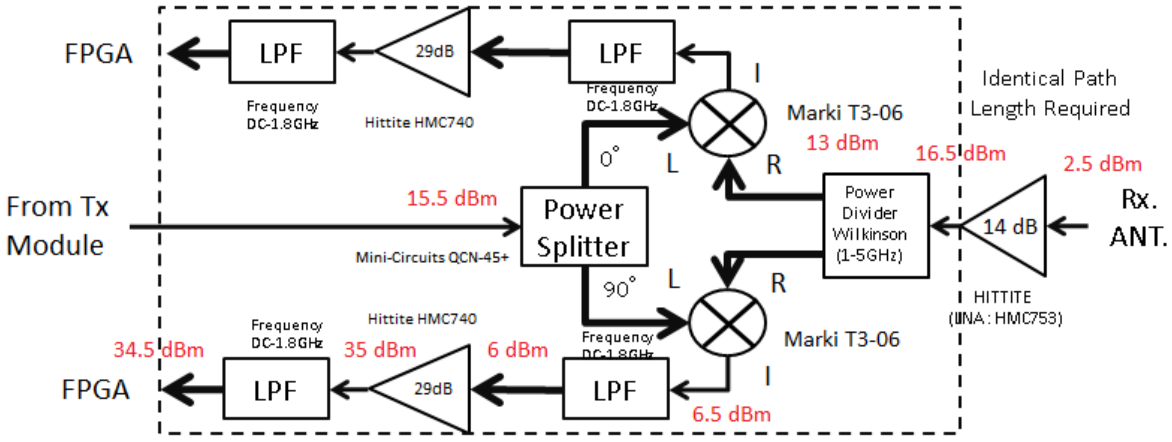

Figure 98 – Receiver block diagram with power levels

Wall Characterization

Noise in the monostatic board provided an opportunity to test the STW module in a "pseudo-monostatic" approach. Instead of one antenna, a bistatic arrangement, with the Horn and Vivaldi antennas close to one another, was set up. The close proximity reduced the travelling wave angle of incidence to approximately 90°.

A wall of solid concrete blocks was assembled in the anechoic chamber, as shown in Figure 99. Eighteen blocks with dimensions of 4"x8"x16" produced a 4'x4' structure. Two tests were performed, one with just the wall and one with a 3'x4' aluminum plate placed in front of the wall. The horn antenna was located 112" away from the wall, 22" above the floor, and 8" to the left of the first element of the Vivaldi array.

Figure 100 shows a composite plot of the wall reflection data overlaying the PEC reflection data. The wall reflection coefficient reduces the returned pulse, compared to the PEC plate. Referring again to equations (34) to (38), calculations by Dr. Chris Thajudeen produced the results shown in Table 8. In his report he notes, "The "actual" values are only included for the computation of % error and are based on the physical thickness of the material and the measured average relative permittivity determined by using a "through" estimation technique which utilized both sides of the wall and S11, S21, S12 data to estimate the parameters. For the "actual" relative permittivity in Table 8, the value was determined using the Agilent 85070 material analysis software over the range of 1GHz to 3 GHz." Another resource corroborates that value [13].

The results show good agreement between actual and estimated permittivity using the pseudo-monostatic approach.

Figure 99 – Testing for wall estimation

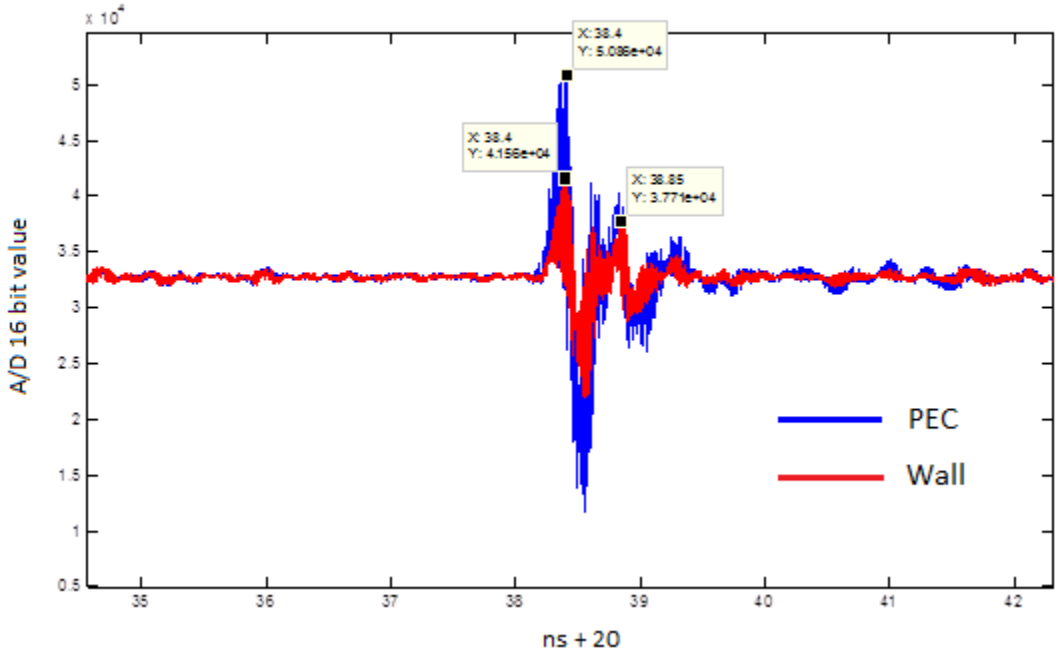

Figure 100 – Wall response overlaid on PEC response

Table 8 – Estimated values using pseudo-monostatic approach

Estimated values	"Actual" Values	Estimated Values	% Error
Relative Permittivity	7 - 8	8.32	8.6%

Chapter 5 – Future Work

Given that the UWB radar module is a mobile device intended for field operation, reliability, smaller size, lower power consumption and better performance would be beneficial. In addition, the following usability issues must be addressed.

The Monostatic board

As mentioned, noise on the monostatic board limited board performance. The electronics behind the design correctly control the RF switch, but isolation must be increased or the noise somehow circumvented. Hittite Microwave makes an absorptive switch, the HMC347LP3, as previously mentioned, which could remedy some of the switch transition discontinuities. Other solutions must be sought to eliminate any noise, reflected or otherwise, from entering the receiver.

FCC Compliance

The Federal Communications Commission has mandated maximum power levels for UWB transmission at -41 dBm from 3.1 to 10.6 GHz. The requirements become stricter below 3.1 GHz, dropping to -65 dBm for the GPS band in 1 to 1.6 GHz range. Reviewing, the output of the transmitter is shown in Figure 101. The carrier and pulse spectrum power outputs of 10 dBm and -28 dBm are acceptable for military applications where communications standards are not a concern. For domestic usage, a simple drop in the output gain of the transmitter board would satisfy the pulse power spectrum requirements. The carrier, however, requires additional work.

The primary cause for the carrier output power originated from mixer leakage on the transmitter board. The Marki mixer required +15 dBm of local oscillator power to drive its internal circuitry. Though it had good isolation of 33 dB from LO to RF output, the resultant leakage was amplified through the gain of the output amplifiers on the transmitter. Because a mixer is inherently a non-linear device, filters are generally applied at the output to reduce harmonics. In this case filters below 5.5 GHz would degrade performance of the STW module output and therefore could not be used.

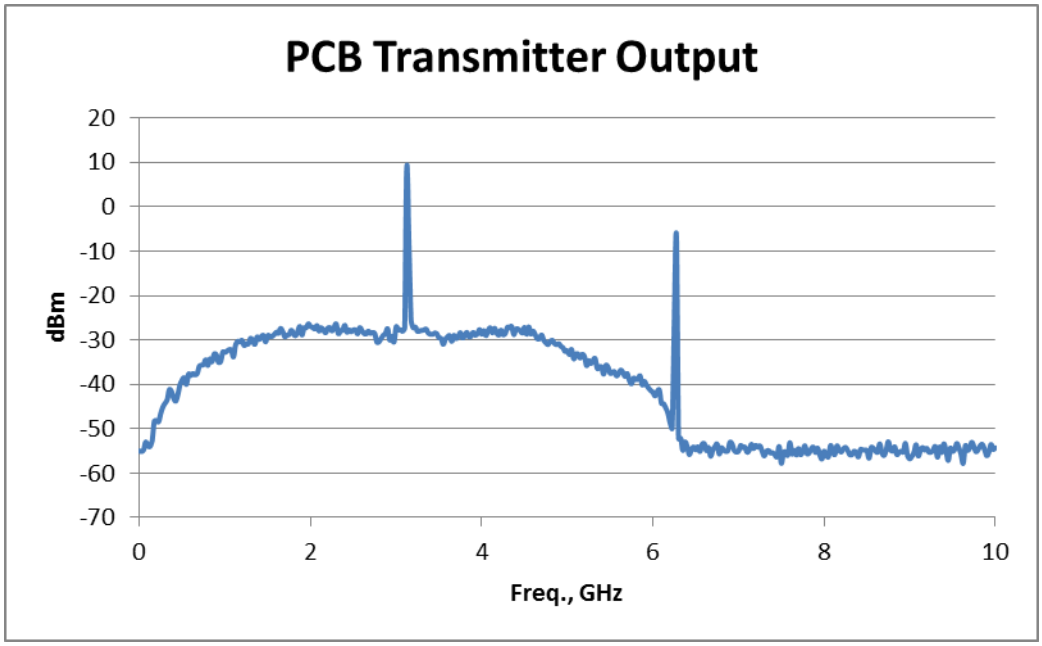

Figure 101 – Transmitter output

In the past several solutions to remove carrier leakage have been attempted, with limited results. A narrowband notch filter was investigated [13], but due to the nature of this filter, its non-linear pulse dispersion made it unacceptable. A defected ground structure was proposed [14], but its inherently narrowband approach also made it unacceptable.

Some progress was made by manipulating input power levels of the mixer, both at the Local Oscillator and IF inputs. By reducing the LO input and increasing the pulse power, a drop of 6.5 dBm was obtained, at the expense of pulse spectrum flatness, Figure 102.

Another potential solution would involve adding the original carrier to the output, 180° out of phase. This could be done with a programmable phase shifter and a Wilkinson power combiner. A proposed model for this technique can be found here [15]. Because of its passive design, it could provide a maximum carrier reduction of 15 dB.

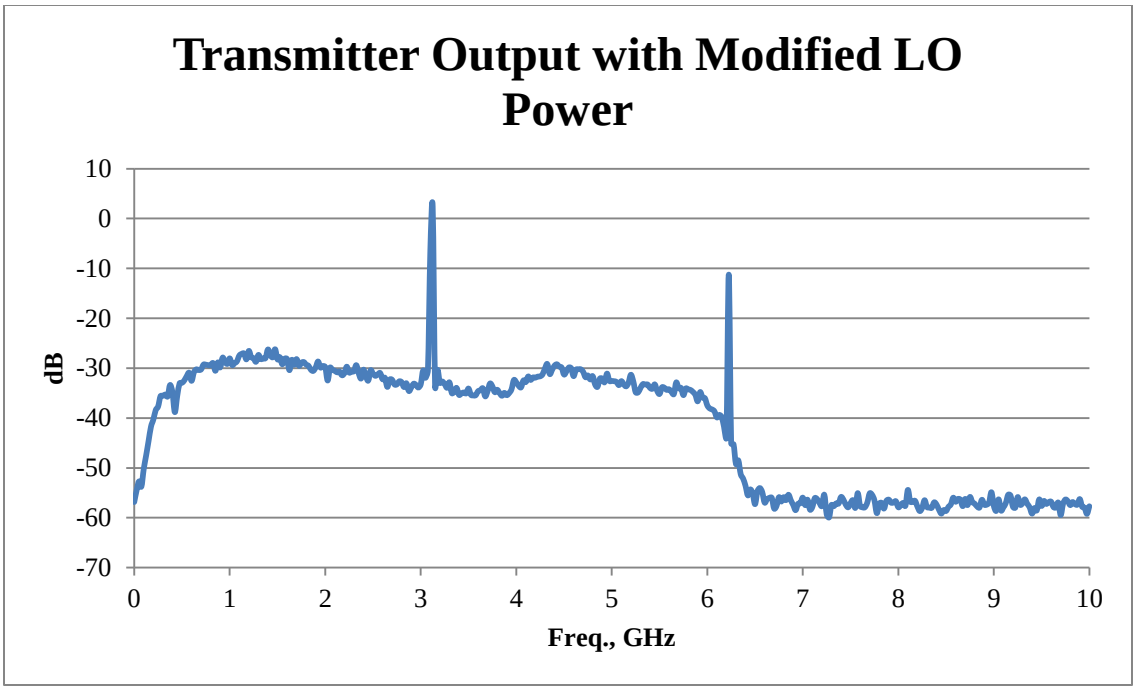

Figure 102 – Carrier suppression through input mixer power manipulation

Additional Issues

To make this module completely portable, several additional issues might also be addressed:

1. Add a battery pack to replace the power converters.
2. Incorporate the digital controller as part of the new module.
3. Adapt the imaging system to a portable display and combine it with the new module.
4. Add simple controls for greater versatility.
5. Develop a small antenna structure with high gain and directivity.
6. Design an attractive container.

Chapter 6 – Conclusion

A compact, mobile UWB radar module was designed. Many improvements were incorporated compared to the original prototype. The final assembly measured 2.5”Wx 6.25”Lx3.5”D, counting the additional monostatic board assembly. Power consumption was reduced to 7W. Costs for manufacturing this module were much lower compared to the cost of components with the prototype.

Co-planar waveguide was implemented. Its quasi-TEM structure provided a good, low loss path for broadband microwave energy. All new surface-mount components such as a VCO, gain-block amplifiers, Mini-Circuits low pass filters, and a new broadband mixer added quality to the design. The Hittite HMC637 Power Amplifier introduced a significant reduction in power usage and component size, while delivering equivalent power output and excellent frequency response. At the receiver, Marki mixers reduced the necessity of two separate receiver boards to one.

A new power supply was designed. Its final size was half the prototype’s, with fewer components and lower cost. Simple connectors were introduced to give it greater flexibility and allow for adaptations or revisions of other boards.

The pulse generator, a separate circuit in the original prototype, was successfully added to the transmitter board. It generated 1V peak, fast 260 ps pulses. Simulation of these pulses using Agilent ADS correlated well with final results. To drive the pulse generator, the original op amp circuit was included, but with improvements to output linearity and reliability.

A monostatic adapter was developed. Without changing controller coding, it generated precise clock delay and pulse shaping to drive a high-speed microwave switch. Pulse energy and a sensitive receiver were correctly gated to a broadband antenna. The microwave switch itself was capable of bandwidths to 20 GHz. Except for gain considerations of the receiver, the board performed flawlessly.

Significant potential exists for the further development of this device. With additions mentioned in Chapter 5, a module could be constructed that would have broad military and commercial usefulness. It could assist firefighters in the rescue of trapped people; it could improve the comfort of the elderly or those who are hospitalized. It could assist doctors in the diagnosis of disease. It could save lives.

Bibliography

1] R. J. Fontana, "Recent system applications of short-pulse ultra-wideband (UWB) technology," *IEEE Trans. Microwave Theory and Tech.*, vol. 52, no. 9, pp. 2087-2104, Sept. 2004.

2] A. E. Fathy, Y. Wang, Y. Koo, L. Ren and S. Magoon, "Using UWB Technology for See Through Wall Imaging, Sensitive Asset Tracking, and Suspicious Human Motion Analysis," in *International Microwave Symposium 2013*, Seattle, 2013.

3] Y. Yang, Development of a Real-time Ultra-wideband See Through Wall Imaging Radar System, Knoxville, TN, 2008.

4] C. A. Balanis, Advanced Engineering Electromagnetics, John Wiley & Sons, Inc., 2012.

5] F. T. Ulaby, E. Michielssen and U. Ravaioli, Fundamentals of Applied Electromagnetics, Pearson Education, Inc., 2010.

6] C. Thajudeen, A. Hoorfar and F. Ahmad, "Measured complex permittivity of walls with different hydration levels and the effect on power estimation of TWRI target returns," *Progress In Electromagnetics Research B*, vol. 30, pp. 177-199, 2011.

7] C. Thajudeen and A. Hoorfar, "Wall parameters estimation using a hybrid time-delay-only and reflected wave ration technique," in *IEEE International Symposium on Antennas and Propagation*, Orlando, FL, 2013.

8] Y. Wang, Q. Liu and A. Fathy, "CW and Pulse-Doppler Radar Processing Based on FPGA for Human Sensing Applications," *IEEE Transactions on Geoscience and Remote Sensing*, vol. 51, no. 5, part 2, May 2013.

9] Q. Liu, Y. Wang and A. Fathy, "Towards Low Cost, High Speed Data Sampling Module for Multifunctional Real-Time UWB Radar," *IEEE Transactions on Aerospace and Electronic Systems,* vol. 49, no. 2, April 2013.

10] C. P. Wen, "Coplanar Waveguide: A Surface Strip Transmission Line Suitable for Nonreciprocal Gyromagnetic Device Applications," *IEEE Transactions on Microwave Theory and Techniques, Vol MIT-17, No. 12,* pp. 1087-1090, December 1969.

11] J. S. Lee and C. Nguyen, "Uniplanar Picosecond Pulse Generator Using Step-Recovery Diode," *Electron Lett.*, vol. 37, no. 8, pp. 504-506, 2001.

12] E. W. Weisstein, "Fourier Transform - Gaussian," [Online]. Available: http://mathworld.wolfram.com/FourierTransformGaussian.html.

13] J. Davis and Y. Huang, "Determination of dielectric properties of insitu concrete at radar frequencies," in *Internation Symposium for Non-Destructive Testing in Civil Engineering 2003*, 2003.

14] C. Zhang, A. Elsherbini, A. Fathy and M. Mahfouz, "Investigation of Pulse Dispersion in a Carrier-Based UWB System with LO Leakage Cancellation," *International Journal of RF and Microwave Computer-Aided Engineering*, pp. 669-674, 2009.

15] J. Liu, W. Y. Yin and S. He, "A New Defected Ground Structure and its Application for Miniaturized Switchable Antenna," *Progress In Electromagnetics Research,* vol. 107, pp. 115-128, 2010.

16] Q. Zhang, Y. Yang, J. Wang and W. Wang, "A Carrier-Suppressed Balance BPSK Modulator for Impulse Radio Ultra-Wideband Transmitter," in *Wireless Communications Fifth International*

Conference on Networking and Mobile Computing, 2009.

17] R. Wilson and J. A. Crawford, "Propagation Losses Through Common Building Materials," Magis Networks, Inc., Los Angeles, 2002.

Vita

Stephen Magoon was born in California. His father, Gerald Magoon, was a successful businessman and politician. For 30 years he managed a women's clothing store, while also leading the city of Tulare as President of the Chamber of Commerce and Kiwanis. He received numerous community awards, including Man of the Year from the Chamber of Commerce. He ran for and was elected several times to the City School Board and the City Council. He was appointed county commissioner for one term by the governor of the state of California. His wife, Norma, was a homemaker and gifted artist. She won numerous awards for water color and photography, but especially as the best Mom from her sons Stephen and David.

Stephen received a Bachelor of Science degree in Electronic Engineering from California Polytechnic State University, San Luis Obispo, California. After working for two years as an engineer, he joined the Navigators, a collegiate Christian service. During this service he met his wife Colette, also staff with the Navigators, in Seattle. They married and moved to Idaho as part of their work with the Navigators, where they had two children, Jonathan and Stephanie.

Currently Stephen and Colette live in Knoxville Tennessee. Jonathan works for a technology company in Colorado as a computer programmer. Stephanie is working toward organic farming in, possibly, Tennessee.

Stephen graduated from the Electrical Engineering and Computer Science Department of the University of Tennessee, Knoxville, in December 2013.